LA-UR-20-26603
Approved for public release; distribution is unlimited.

Title: 2020 LANL Contributions to the BATS Test in WIPP

Author(s): Guiltinan, Eric Joseph; Boukhalfa, Hakim; Dangelmayr, Martin A.; Dozier, Brian Lee; Janicke, Michael Timothy; Livingston, Daniel Reece; Marina, Oana C.; Otto, Shawn; Rahn, Thomas A.; Ware, Stuart Douglas; Weaver, Douglas James; Stauffer, Philip H.; Kuhlman, Kristopher; Mills, Melissa; Jayne, Richard; Matteo, Ed; Herrick, Courtney; Nemer, Martin; Heath, Jason; Xiong, Yongliang; Choens, Charles; et al.

Intended for: Report

Issued: 2020-09-03 (rev.2)

2020 LANL Contributions to the BATS Test in WIPP

Spent Fuel and Waste Disposition

Prepared for
US Department of Energy
Spent Fuel and Waste Science and Technology
Milestone M3SF-20LA010303012

Los Alamos National Laboratory
Eric Guiltinan, Hakim Boukhalfa, Martin Dangelmayr, Brian Dozier, Michael Janicke, Daniel Livingston, Oana Marina, Shawn Otto, Thom Rahn, Doug Ware, Doug Weaver, Philip H. Stauffer

Sandia National Laboratories
Kristopher L. Kuhlman, Melissa Mills, Richard Jayne, Ed Matteo, Courtney Herrick, Martin Nemer, Jason Heath, Yongliang Xiong, Charles Choens

Lawrence Berkeley National Laboratory
Jonny Rutqvist, Yuxin Wu, Mengsu Hu

August 30, 2020
LA-UR-20-26603

DISCLAIMER

This information was prepared as an account of work sponsored by an agency of the U.S. Government. Neither the U.S. Government nor any agency thereof, nor any of their employees, makes any warranty, expressed or implied, or assumes any legal liability or responsibility for the accuracy, completeness, or usefulness, of any information, apparatus, product, or process disclosed, or represents that its use would not infringe privately owned rights. References herein to any specific commercial product, process, or service by trade name, trade mark, manufacturer, or otherwise, does not necessarily constitute or imply its endorsement, recommendation, or favoring by the U.S. Government or any agency thereof. The views and opinions of authors expressed herein do not necessarily state or reflect those of the U.S. Government or any agency thereof.

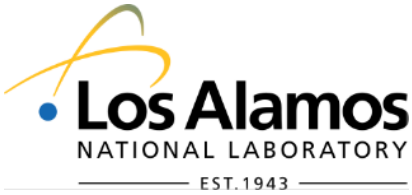

APPENDIX E

NFCSC DOCUMENT COVER SHEET [1]

Name/Title of Deliverable/Milestone/Revision No. 2020 LANL Contributions to the BATS Test in WIPP M3SF-20LA01030301

Work Package Title and Number Salt Disposal F&D - LANL SF -20LA01030301

Work Package WBS Number 1.08.01.03.03

Responsible Work Package Manager Philip Stauffer (Signature on file)
(Name/Signature)

Date Submitted 8/28/20

Quality Rigor Level for Deliverable/Milestone[2]	☐ QRL-1 ☐ Nuclear Data	☐ QRL-2	☑ QRL-3	☐ QRL 4 Lab QA Program[3]

This deliverable was prepared in accordance with Los Alamos National Laboratory (LANL)
(Participant/National Laboratory Name)

QA program which meets the requirements of
☑ DOE Order 414.1 ☐ NQA-1 ☐ Other

This Deliverable was subjected to:

☑ Technical Review ☐ Peer Review

Technical Review (TR)
Review Documentation Provided
☐ Signed TR Report or,
☐ Signed TR Concurrence Sheet or,
☑ Signature of TR Reviewer(s) below
Name and Signature of Reviewers
Artaches Migdissov: Section 2
(Signature on file)
Florie Caporuscio: Section 2
(Signature on file)

Peer Review (PR)
Review Documentation Provided
☐ Signed PR Report or,
☐ Signed PR Concurrence Sheet or,
☐ Signature of PR Reviewer(s) below
Name and Signature of Reviewers
Hari Viswanathan: All Sections
(Signature on file)

NOTE 1: *Appendix E should be filled out and submitted with each deliverable. Or, if the PICS: NE system permits, completely enter all applicable information in the PICS: NE Deliverable Form. The requirement is to ensure that all applicable information is entered either in the PICS: NE system or by using the NFCSC Document Cover Sheet.*

- *In some cases there may be a milestone where an item is being fabricated, maintenance is being performed on a facility, or a document is being issued through a formal document control process where it specifically calls out a formal review of the document. In these cases, documentation (e.g., inspection report, maintenance request, work planning package documentation or the documented review of the issued document through the document control process) of the completion of the activity, along with the Document Cover Sheet, is sufficient to demonstrate achieving the milestone.*

NOTE 2: *If QRL 1, 2, or 3 is not assigned, then the QRL 4 box must be checked, and the work is understood to beperformed using laboratory QA requirements. This includes any deliverable developed in conformance with the respective National Laboratory / Participant, DOE or NNSA-approved QA Program.*

NOTE 3: *If the lab has an NQA-1 program and the work to be conducted requires an NQA-1 program, then the QRL-1 box must be checked in the work Package and on the Appendix E cover sheet and the work must be performed in accordance with the Lab's NQA-1 program. The QRL-4 box should not be checked.*

ACKNOWLEDGEMENTS

The authors thank Dustin Crandall from National Energy Technology Laboratory (NETL) for providing preliminary imaging and characterization results from our salt cores. We also acknowledge the assistance and support of the WIPP underground facilities personnel, who make the implementation in the underground possible, and support of the DOE Office of Environmental Management (DOE-EM) Carlsbad Field Office (CBFO) chief scientist, George Basabilvaso. The authors acknowledge Artaches Migdissov, Florie Caporuscio, and Hari Viswanathan (LANL) for reviewing versions of this document.

CONTENTS

Contents iv
LIST OF FIGURES vi
LIST OF TABLES ix
Acronyms x

1. Introduction 1
   1.1 Test Overview 1
   1.2 Document Preview 6

2. Chemistry of the brines from the Brine availability test in salt at WIPP (BATS) experiment: Effect of temperature and brine migration on brine composition 7
   2.1 Summary of progress in understanding the chemistry brine at WIPP 7
   2.2 Timetable of the BATS experiment: history of brine sampling 9
   2.3 Chemistry of WIPP brines 10
      2.3.1 Overview of chemistry of WIPP brines from historical data 10
      2.3.2 Chemistry of brine samples from the East and West arrays of the BATS experiment 13
      2.3.3 Geochemical modeling of brine chemistry 19
   2.4 Characterization of brine migration under temperature gradients using low field NMR 27
      2.4.1 Experimental Methods 27
      2.4.2 Results Low field NM examination of water distribution in salt: characterization before and after heating. 30
   2.5 Conclusions and Future work 33

3. Isotopic Analysis 36
   3.1 Water Isotopic Composition 36
      3.1.1 Water Isotopic Composition Time Series: Phase 1 37
      3.1.2 Water Isotopic Composition Time Series: Permeability Tests 42
      3.1.3 Water Isotopic Composition of Fluid Inclusions 46

4. FEHM Code Development during FY20 48
   4.1 Humidity and salt related boundary conditions: new keywords, updated existing keywords 48
   4.2 Examples of boun models 50
   4.3 Simulation examples using boun models 53
   4.4 Tabular Air Equation of State for all temperatures 55
   4.5 Other AWH and Salt activities 56
      4.5.1 Computation algorithm for fixed gridblock relative humidity and flowing relative humidity 56

5. Modeling 58

5.1 Model Development 58
5.2 Initial Results of 3D Model 61
5.3 2D Radial Model 63
5.4 Isotopic Simulations 65
5.5 Vadose Zone Journal Publication 68

6. Permeability Measurements 69
6.1 Borehole Pressure Decay Experiments 69
6.2 U D Borehole Threshold Pressure Testing 71

7. BATS Lessons Learned 74

8. SFWD Website 79
8.1 Website Sections 79
8.1.1 Journals page 79
8.1.2 DOE Reports page 79
8.1.3 WIPP Experiments page 79
8.1.4 People page 80
8.2 Additional Comments 80
8.3 Screenshots of the Website 80

9. Summary 85

10. References 86

11. Appendix 1 89

LIST OF FIGURES

Figure 1-1. WIPP underground map. BATS location indicated with red circle. Shakedown test location indicated with blue star. Drift widths not to same scale as repository layout. 2

Figure 1-2. Borehole layout plan for each BATS test array (heated and unheated)..... 3

Figure 1-3. Conceptual wiring and plumbing diagram for the heated HP borehole 4

Figure 1-4. Water concentration measured by LI-COR gas analyzer. 4

Figure 1-5. Temperature response in the heated array boreholes during Phase 1a. 5

Figure 2-1. History of brine sampling for the BATS experiment 10

Figure 2-2. Plot of major elements ratios representing various fluid inclusions and commonly sampled brine from WIPP related studies. 12

Figure 2-3. Plot of major elements ratios representing East and West array boreholes from the BATS along with various fluid inclusions and commonly sampled brine from WIPP related studies. The BATS samples were obtained on 4-24-2019 immediately after completion of the boreholes (green circles). 15

Figure 2-4. Plot of major elements ratios representing various fluid inclusions and commonly sampled brine from WIPP related studies. The plot includes historical data (squares) and brines from the BATS experiments samples at different times before heating over 9 moths (green and blue circles). 17

Figure 2-5. Plot of major elements ratios representing various fluid inclusions and commonly sampled brine from WIPP related studies. The plot includes the sample from the shakedown test (orange circle). 19

Figure 2-6. Graphical representation of the saturation indices of the different minerals relevant to GWB brine. The chemical formula of the different minerals are as follows: Polyhalite $K_2Ca_2Mg(SO_4)_4 \cdot 2H_2O$, Magnesite $MgCO_3$, Anhydrite $CaSO_4$, Gypsum $CaSO_4 \cdot 2H_2O$, Halite NaCl, Brucite $Mg(OH)_2$, Goergeyite $K_2Ca_5(SO_4) \cdot 6H_2O$, Huntite $CaMg_3(CO_3)_4$, Dolomite $CaMg(CO_3)_2$ 21

Figure 2-7. Graphical representation of the saturation indices of the different minerals relevant to BATS brines. The chemical formula of the different minerals are as follows: Polyhalite $K_2Ca_2Mg(SO_4)_4 \cdot 2H_2O$, Magnesite $MgCO_3$, Anhydrite $CaSO_4$, Gypsum $CaSO_4 \cdot 2H_2O$, Halite NaCl, Brucite Mg(OH)2, Huntite $CaMg_3(CO_3)_4$, Dolomite $CaMg(CO_3)_2$. 26

Figure 2-8. Experimental setup showing the heating unit, temperature controller, scale, and core together with the data logger. 28

Figure 2-9. Salt core with connected thermocouples and temperature readings on 8/6/20. 29

Figure 2-10. Magritek NMR Mouse pictured with KEA spectrometer. 30

Figure 2-11. T_2 measurements and Laplace Inverse Transform results. Raw data acquired from the Magritek NMR Mouse for the measurements of the salt core. The left panel shows the full set of 400 echoes acquired using the CPMG experimental parameter set with the middle image reporting just the echo intensity and the right panel showing the Laplace Inverse Transform results of the signal showing the different water populations (different peaks and their relative abundances “amplitude of the peak”). Hot side refers to the side of the core that was in direct contact with the hot plate and the cold side refers to the top of the core. 31

Figure 2-12. Bar graph showing a summary of the relaxation times T_2 and T_2 of the free water (associated to minerals or in tight pores) and water in inclusions. The data represent the top and bottom of the salt core before and after heating. 32

Figure 2-13. Bar graph showing a summary of intensity of the signals attributed to the bound and free water. The data represent to top and bottom of the salt core before and after heating. 33

Figure 3-1. Stable water isotope data from WIPP site characterization studies (from Lappin, 1988)..... 36

Figure 3-2. Time series of borehole temperatures (left) and diameter (right)..... 37

Figure 3-3. H_2O vapor concentration as well as $\delta^{18}O$ and $\delta^{2}H$ in the heated (left) and unheated (right) boreholes as a function of time. Color changes indicate heater on and off as well as changes in gas flow to optimize analytical performance..... 39

Figure 3-4. Carbon dioxide in continuous flow sample stream of the heated borehole. Unheated borehole CO_2 (not shown) was constant at ~2 ppm. 40

Figure 3-5. Trace gas analyses normalized to N_2. Top: Complete period of heating. Bottom: Detailed observations at time of heater turn-off..... 41

Figure 3-6. Temperature time series during permeability testing in spring/summer of 2020. Top panel shows entire time series while bottom panel shows detail of heating periods of late April through May. 43

Figure 3-7. H_2O vapor concentration as well as $\delta^{18}O$ and $\delta^{2}H$ in the heated (orange) and unheated (blue) boreholes as a function of time..... 44

Figure 3-8. $\delta^{2}H$ relative to $\delta^{18}O$ for the heated (left) and unheated (right) boreholes during the permeability testing period April to August 2020..... 45

Figure 3-9. $\delta^{2}H$ relative to $\delta^{18}O$ for the outlying data highlighted in Figure 3-8. 45

Figure 3-10. Crusher with inlet and injection port on the left. Picarro CRDS on the right..... 46

Figure 3-11. Correlation of measured reference material vs known values, O isotopes on left, H isotopes on right..... 47

Figure 4-1. 1D domain used for example simulations with boun macro keywords and tabular air EOS verification. 53

Figure 4-2. Pressures (2a), temperatures (2b), and relative humidity (2c), for model 3 applied for the Left BC and model 7 applied for the Right BC..... 55

Figure 4-3. Comparison of table and previous existing properties in FEHM 56

Figure 5-1. As-built locations and orientations of the boreholes in the heated array. From Kuhlman et. al, 2020..... 58

Figure 5-2. Borehole locations at the drift face in the three dimensional Phase 1 model domain 59

Figure 5-3. Three dimensional representation of the model..... 59

Figure 5-4. The initial pressure distribution development for the Phase 1a model. The model is initialized with a formation pressure of 12 MPa and an atmospheric pressure and zero saturation boundary condition representing the drift face. The model is ran for 7 years to develop the initial pressure and saturation condition for the model. On the right, a

slice through the center of the model showing the pressure around the boreholes after 5 days. 60
Figure 5-5. 750W Infrared heater, borehole closure gage, and thermocouples. From Kuhlman et al, 2020 61
Figure 5-6. Temperature at thermocouple control near heater compared to nearby thermocouple. 62
Figure 5-7. Saturation, permeability, and temperature in the parallel to the drift face in the plane of the heater 62
Figure 5-8. Phase 1 3D simulation results. Left, the temperature response in borehole T1. Right, temperature response in Borehole T2. TC8 is in the plane of the heater and thus the warmest thermocouple. TC-10 and TC-6 are deeper and shallower than TC-8, respectively. 63
Figure 5-9. Permeability in 2D radial model of the Phase 1 experiment. 64
Figure 5-10. Temperature result at HT2-8 using $\lambda IS, 300 = 5.15$ for intact salt and step heating schedule shown in Table 5.2. 65
Figure 5-11. Permeability distribution of 2D radial isotope simulation with borehole (red), packer (dark blue), and intact salt (light blue) 66
Figure 5-12. Initial Isotope Experiment. A borehole with no isotopic $^{18}0$ is flooded with $^{18}0$ from nearby salt formation. 67
Figure 5-13. Vadose Zone Journal cover. 68
Figure 6-1. Permeability testing data compared to FEHM simulations of the heated borehole in the Phase 1 borehole configuration. The data is approximately matched with a permeability of 2e-17 m^2. 70
Figure 6-2. Leaky packer detected during permeability experiments. 71
Figure 6-3. U-D nitrogen breakthrough pressure experiment 72
Figure 6-4. Permeability and threshold pressure in the salado formation. From Davies (1997) 72
Figure 6-4. Phase 1 U-D permeability simulation. 73
Figure 8-1. Homepage of the https://sfwd.lanl.gov website. 80
Figure 8-2. Journals webpage. 81
Figure 8-3. DOE Reports webpage. 82
Figure 8-4. WIPP Experiments webpage. 83
Figure 8-5. The BATS subsection of the WIPP Experiments webpage 83
Figure 8-6. The BATS subsection of the WIPP Experiments webpage, with some content sections expanded. 84
Figure 8-7. The BATS Phase 1 photo gallery within the WIPP Experiments webpage. 85

LIST OF TABLES

Table 2-1 Timetable showing the time of BATS boreholes and related dates of brine samples collection. 9

Table 2-2 Summary of selected brine inclusions analyses obtained from WIPP at the repository level. Inclusions composition is expressed in g/L. All data were taken from Stein and Krumhansl, (1986). 11

Table 2-3 Summary of brine samples collected from the BATS experiment heated and unheated arrays before heating 14

Table 2-4 Summary of brine analyses performed on the first samples obtained from the East and west array boreholes sampled on 4-18-2019. All concentrations are in g/L. 14

Table 2-5 Summary of brine samples collected from the BATS experiment heated and unheated arrays before heating. 16

Table 2-6. Analyses of brines from BATS collected from different boreholes before heating. 16

Table 2-7. Summary of brine samples collected from the BATS experiment heated and unheated arrays before heating. 18

Table 2-8. Analyses of brines from BATS collected from different boreholes before heating. 18

Table 2-9. PHREEQC calculation of mineral saturation of the main minerals susceptible to undergo significant precipitation/dissolution for GWB brines under variable temperatures. 21

Table 2-10. Thermodynamic equilibrium calculations by PHREEQC the main minerals susceptible to undergo significant precipitation/dissolution for brines sampled from the bats experiment U-D-4-18-19 and the shakedown. 22

Table 3-1. Timing of various changes in flow rate and borehole heating which correspond with highlighted changes in Figure 3-3. 38

Table 3-2. Sequencing of gas flow rate and hating during the permeability testing period of April to August 2020 42

Table 3-3. Measured and corrected values for H and O isotopes of 500 mg crushed BATS salt samples. 47

Table 4-1 List of boun keywords indicating related keywords and input macros. FEHM input macros in bold; boun keywords in plain text. 49

Table 5-1 Key initial parameters used for Phase 1a borehole simulations 60

Table 5-2 Heating schedule during the 2D radial Phase simulation 64

Table 5-3 Diffusion and Henry's law parameters for isotope modeling 66

Table 6-1 A summary of the permeability tests conducted on the Phase 1 borehole configurations 69

ACRONYMS

AMU	Atomoic Mass Units
BATS	Brine Availability Test in Salt
BSEP	Brine Sampling and Evaluation Program
CBFO	Carlsbad field office (DOE-EM WIPP office)
CRDS	Cavity Ring-Down Spectrometer
DOE	Department of Energy
DOE-NE	DOE Office of Nuclear Energy
DRZ	disturbed rock zone
ERDA	Energy Research and Development Administration
ERT	electrical resistivity tomography
GWB	Generic Weep Brine
LANL	Los Alamos National Laboratory
LBNL	Lawrence Berkeley National Laboratory
LVDT	linear variable differential transformer
QMS	Quadrupole Mass Spectrometer
RH	relative humidity
SFWD	Spent Fuel & Waste Disposition Campaign
SNL	Sandia National Laboratories
US	United States
WIPP	Waste Isolation Pilot Plant (DOE-EM site)

This page is intentionally left blank.

2020 LANL CONTRIBUTIONS TO THE BATS TEST IN WIPP

1. Introduction

The DOE Office of Nuclear Energy (DOE-NE) repository research and development program seeks to provide a sound technical basis for multiple viable disposal options, increase confidence in the robustness of generic disposal concepts, and develop science and engineering tools needed to support disposal concept implementation. Sandia, Los Alamos, and Lawrence Berkeley National labs are conducting research into salt, which includes the Brine Availability Test in Salt (BATS) field test at the Waste Isolation Pilot Plant (WIPP), a DOE Office of Environmental Management facility. BATS is leveraging the existing infrastructure associated with the WIPP to advance science informing generic disposal concepts.

BATS is an ongoing heated borehole experiment being conducted in the WIPP underground. The goal of this experiment is to reduce the uncertainty associated with spent nuclear fuel disposition in geologic salt formations. The BATS experiments is designed to accomplish this by increasing our understanding of brine migration in salt, assessing damaged zones from mining and drilling, simulating a post-closure environment, confirming salt properties, and providing data for model validation. Phased testing for generic salt repository R&D was proposed in 2015 (Stauffer et al., 2015). Subsequently, borehole thermal testing was developed as a first step in this process (Johnson et al., 2017, Kuhlman et al., 2017). This document summarizes the work conducted on the BATS experiment during fiscal year 2020 with an emphasis on the contributions by Los Alamos National Lab.

1.1 Test Overview

The first phase of the BATS experiments was conducted as a "shakedown" test and is known as Phase 1s (Boukhalfa et al., 2018; Mills et al., 2019). This test was conducted in boreholes drilled in 2012 in the E-140 drift (Figure 1). The experiment was performed from June 2018 through April 2019 with a journal article summarizing the results and modeling published this fiscal year (Guiltinan et al., 2020). Lessons learned from the Phase 1s were used in the construction and implementation of the full Phase 1 experiment. In particularly it was discovered that the initial stainless steel block heater did not put enough energy into the system to achieve our target temperature of 120° C and instead a 750W infrared heater was selected. Additionally, several other designs changes were made and best practices around operating underground at WIPP were put in place.

The Phase 1 experimental plan is presented in SNL (2020) and includes experiments conducted on two borehole arrays located in the N-940 drift (Figure 1). An as-built description of the Phase 1 experiment and detailed description of all data acquired to date is discussed Kuhlman et al., (2020). The drilling of the arrays was completed in April 2019 and instrumentation continued into fiscal year 2020. Each array includes a central borehole (HP) with a heater (for the heated

array only) and a packer as well as dry N_2 gas circulation to remove brine (Figure 2). Surrounding the central borehole are boreholes for temperature sensors only (T), acoustic emissions (AE), a cement seal (SL), D_20 isotopic tracer injection (D), electrical resistivity (E), fiber optic (F), isotopic sampling (SM). The western array is heated while the eastern array serves as an unheated control. Phase 1a, an initial test on the new arrays was conducted from January to March 2020 before the power was shut off at WIPP for planned electrical upgrades in March. Following the planned electrical outage uncertainty surrounding covid-19 prevented the restart of the heater. Phase 1b and 1c, which will include liquid and gas tracers are planned to be carried out later in 2020.

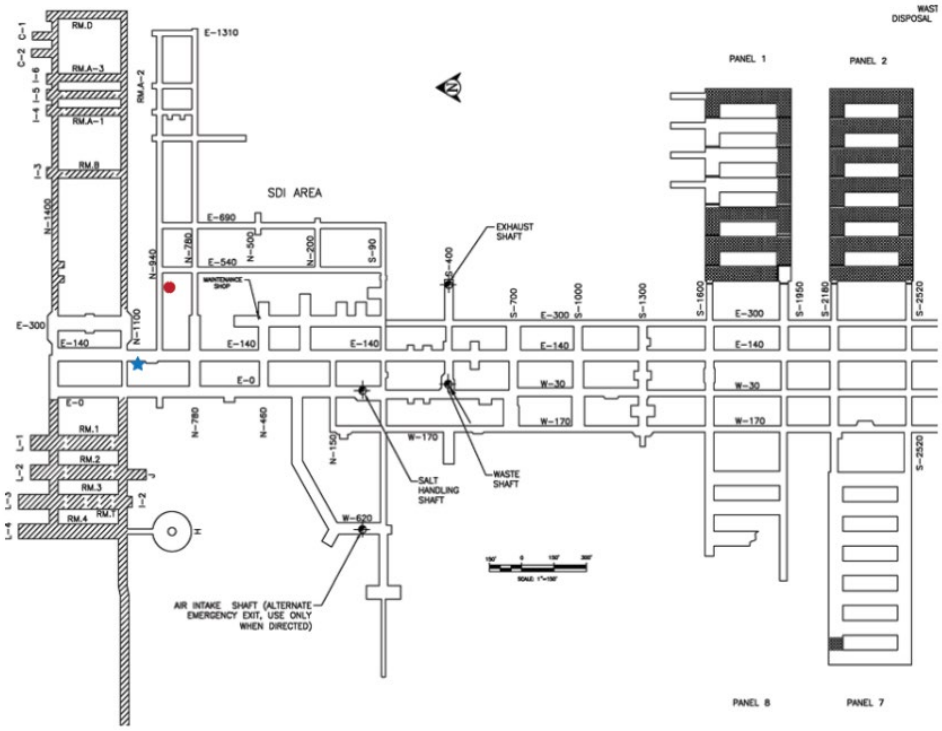

Figure 1-1. WIPP underground map. BATS location indicated with red circle. Shakedown test location indicated with blue star. Drift widths not to same scale as repository layout.

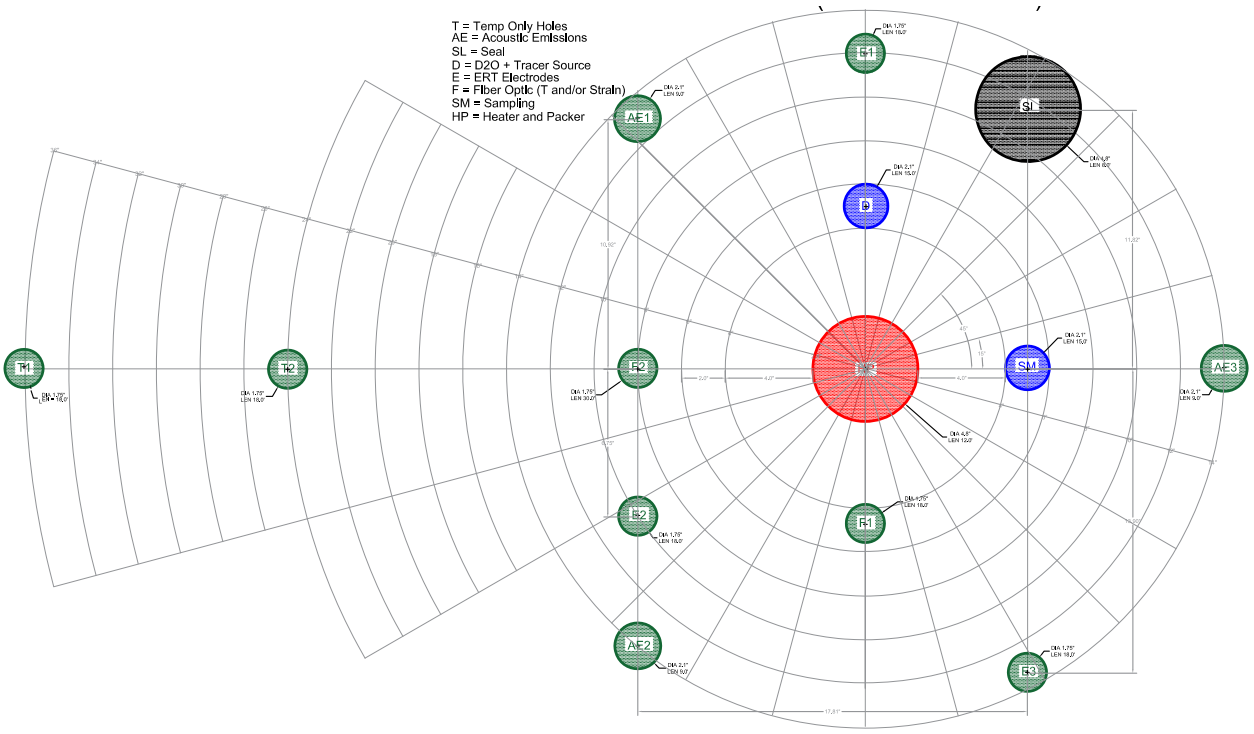

Figure 1-2. Borehole layout plan for each BATS test array (heated and unheated).

Heating for Phase 1A was provided by a 750 W infrared heater isolated behind an inflatable packer along with a borehole closure gage (Figure 1-3). Dry Nitrogen gas was circulated behind the packer and through a gas analyzers befored passing through two dessicant traps. By weighing the dessicant traps the amount of water removed from the borehole can be measured and compared to that calculated from the gas analyzers. The concentration of water in the outflow during Phase 1a is showing in Figure 1-4.

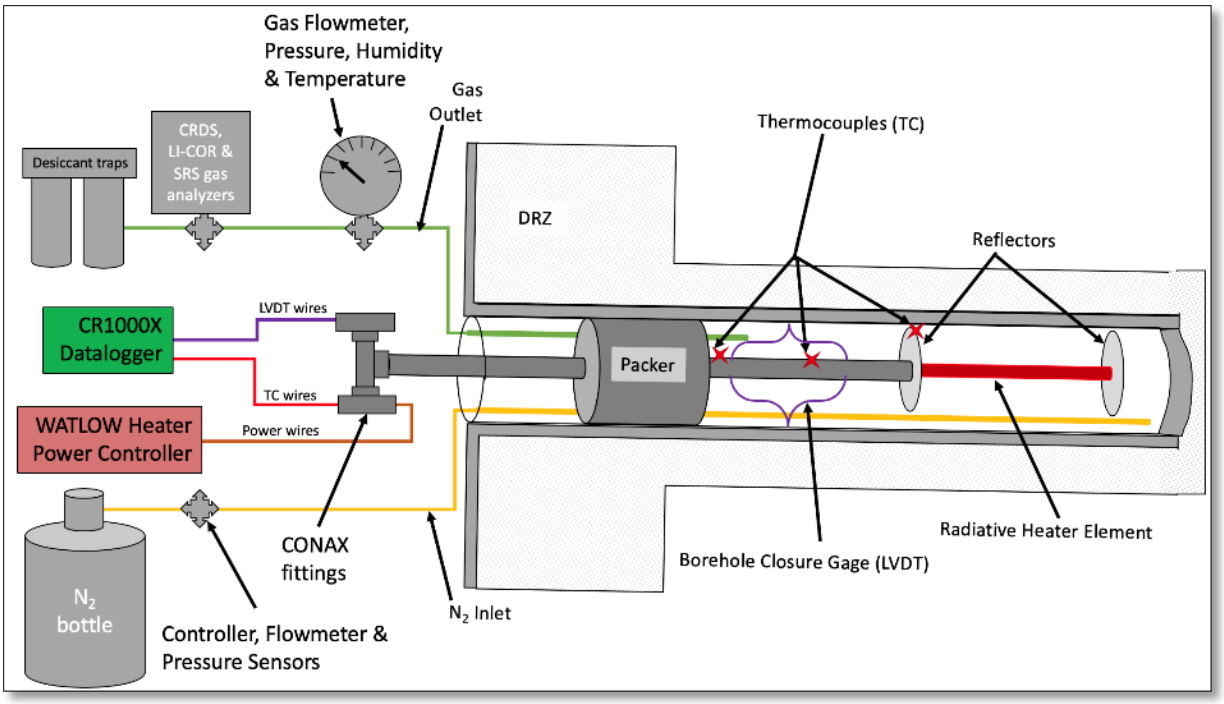

Figure 1-3. Conceptual wiring and plumbing diagram for the heated HP borehole

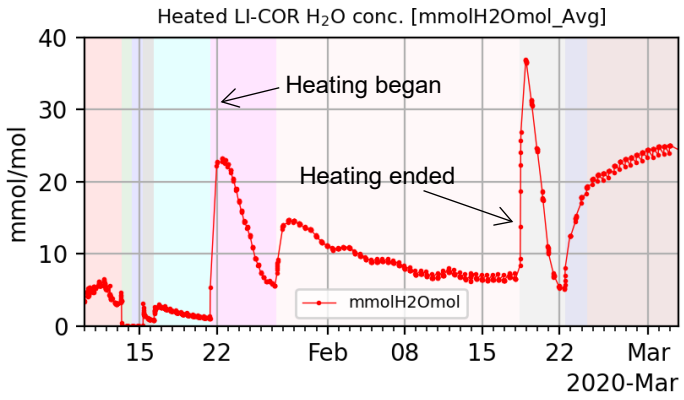

Figure 1-4. Water concentration measured by LI-COR gas analyzer.

Temperature sensors were located in most of the boreholes including 16 thermocouples in each of the temperature boreholes (T1 and T2, Figure 1-5). The lower right panel shows the temperature at the thermocouple which is used to control the heater (red) and the power of the heater (green). While the heater is rated to 750 W it only puts out enough power to achieve the target temperature and the controlling thermocouple. For a complete review of all the data collected during BATS Phase 1a please see Kuhlman et al., (2020).

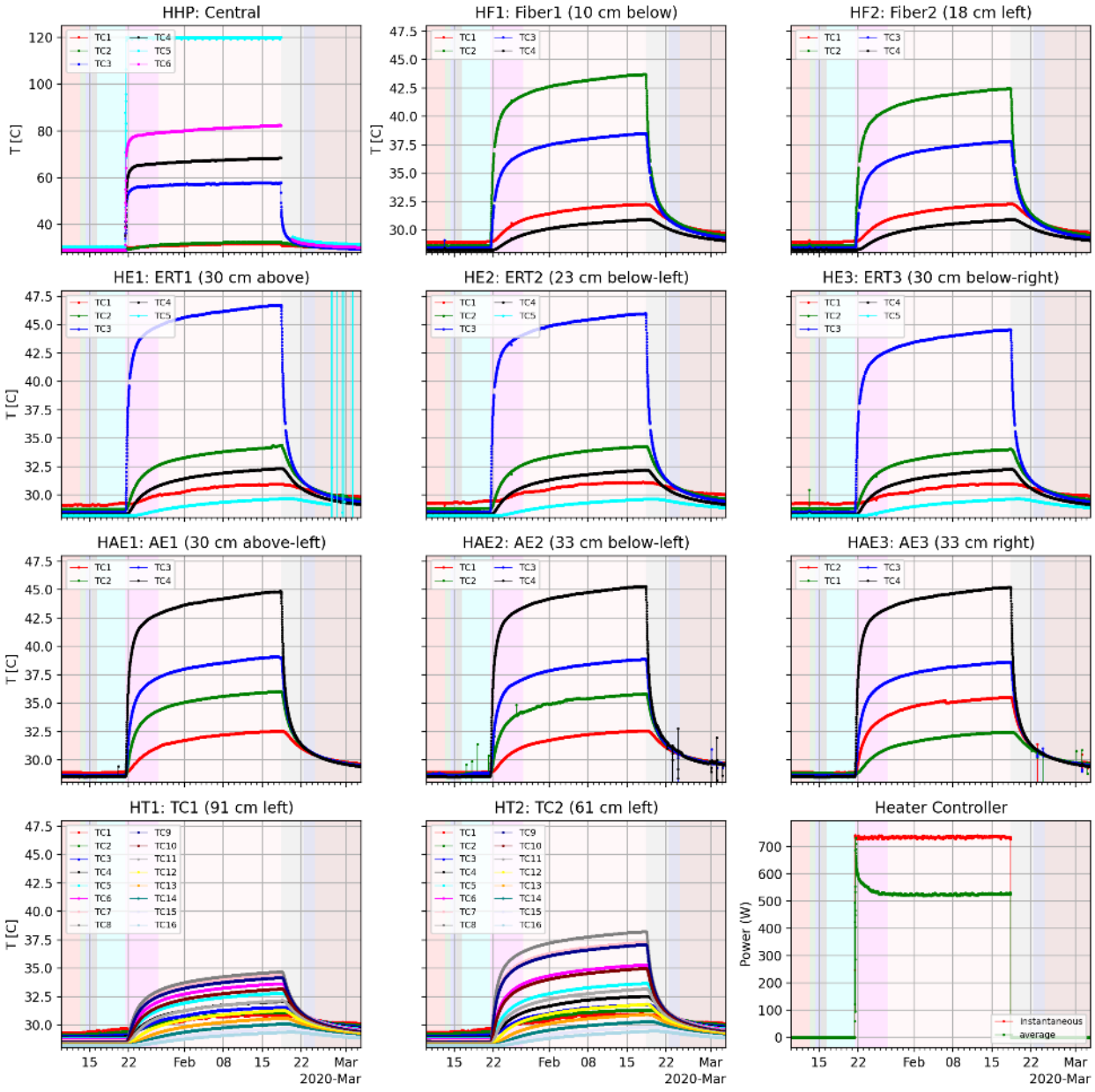

Figure 1-5. Temperature response in the heated array boreholes during Phase 1a.

1.2 Document Preview

This document describes the LANL contributions to the BATS experiments performed during fiscal year 2020. We present (Chapter 2) chemical analysis of WIPP brines, (Chapter 3) ongoing experiments to characterize the isotopic signature of different brine sources, (Chapter 4) upgrades to the FEHM code to add new functionalities to support the BATS experiments https://fehm.lanl.gov, (Chapter 5) modeling of the thermal and isotopic response during Phase 1a (Chapter 6) permeability testing of the BATS Phase 1 boreholes, (Chapter 7) lessons learned by the LANL Carlsbad office in the implementation of these experiments and (Chapter 8) the presentation of the our new website highlighting LANL's contributions to the SFWD campaign.

2. Chemistry of the brines from the Brine availability test in salt at WIPP (BATS) experiment: Effect of temperature and brine migration on brine composition

2.1 Summary of progress in understanding the chemistry brine at WIPP

This chapter describes current progress made in both geochemical modeling and R&D efforts focused on understanding the mechanisms of brine migration, brine availability, and the chemistry of brines sampled from the BATS experiment. The structure of this chapter comprises three sections. The first section presents an overview of the historical data reported in the literature detailing the chemistry of brines sampled in the WIPP underground, synthetic brines used in studies related to WIPP, and analyses of brines collected from several boreholes from both the East (unheated) and West arrays of the BATS experiment. The second section of this chapter will present initial geochemical modeling setup in PHREEQC to simulate the chemistry of brines from the widely used synthetic brines including GWB, ERDA-6 and others. The geochemical model is used to simulate the re-equilibration in the WIPP environment of the initial set of brines collected from the BATS experiment. The third section presents the details of a heating experiment setup with a small salt core collected from the BATS experiment. The section presents results that show the versatility of low field NMR and the ability of the technique to map the distribution of brines in a salt, and the mapping of brine migration in a temperature gradient. Brine distribution data in a salt core before and post heating are presented.

The Permian salts beds horizon at the WIPP facility are mostly dry. However, boreholes drilled in the salt rock accumulate brines very quickly and there are visible wet spots in the underground from water seeping in from the salt walls. The amount of brine in salt depends on the salt formation and can vary significantly but remains largely < 5 wt. % and there is usually more brine in the clay rich layers (Caporuscio et al., 2014) The chemistry of the brine associated with salt has been extensively evaluated in by the Brine Sampling and Evaluation Program (BSEP) established at WIPP in the 1980's and by more recent studies (Bein et al., 1991; Deal et al., 1991; Garcia-Veigas et al., 1992; Stein and Krumhansl, 1986). Several studies have also evaluated the brine mineral relation in reaction to brine composition (Braitsch, 2012; Hardie, 1968, 1982). The detailed report on the variation of the chemistry of fluid inclusion brines by Stein and Krumhansl (Hardie, 1968) is very comprehensive and represents that as elemental ratios that permits a visual representation of the variability of the fluid inclusions chemistry. A comprehensive evaluation of the brine chemistry in salt formations describing both historical studies and modeling is also available (Colon et al., 2012). The plot of the Na/Cl ratio as a function of K/Mg ratio is a good illustration of the variability of the chemical composition of the chemistry of the brine inclusions (Figure 2-2). The K/Mg ratio in the fluid inclusions varies from 0.15 to 0.85 and the Na/Cl ratio varies between 0.15 and 0.55. The weeps or brine sampled from wet places, which re-equilibrated within the WIPP environment in contact with the accessory mineral present in salt show less variably and are mostly centered at K/Mg of 0.8 and a Na/Cl ratio of 0.45 (Stein and Krumhansl, 1986). The brines are not always charge balanced and the analyses often show significant discrepancies between the sum of positive and negative charges. This is often due to analytical difficulties and the need to dilute samples up to a million times for

the analyses. The different samples collected from the BATS experiment before heating over nine months of sampling are all grouped above all historical data at a K/Mg of 0.35 and a Na/Cl ratio of 0.65. The brine analyses performed also show some significant charge imbalance. It is not clear why the chemical composition of the brines collected from the BATS experiment show significant deviation from the weeps and brines sampled historically from boreholes drilled in the WIPP facility horizon.

Preliminary geochemical modeling efforts to test trends in re-equilibration processes in the presence of different minerals associated with WIPP salt are ongoing. These efforts will help gain an understanding of the evolution of the chemistry of brines and identify the important mineral phases that affect brine composition. PHREEQC was used to model saturation indices of minerals for the salt inclusions and various brines. The purpose of the modeling exercises was to investigate the re-equilibration of the inclusions brines as they migrate under thermal gradient. Precipitation of minerals causes shifts of ionic ratios of the brines as they are transport through the salt crystals. Specifically, the formation of mineral hydrates such as Gypsum ($CaSO_4$ $2H_2O$), Carnallite ($KMgCl_3 6H_2O$) , Bischofite ($MgCl_2 6H_2O$) and Polyhalite ($K_2MgCa_2(SO_4)4_2H_2O$) can impact the solution chemistry of brines through the concentration of the brine by removal of water from the brine. We report progress on the simulation of brine chemistries of synthetic brines widely used in WIPP related studies such as Brine A, G-Seep, GWB, ERDA. We also report simulations of fluid inclusion brines reported in archived Sandia National Laboratory reports by Stein and Krumhansel (1986). Average values for the ionic constituents found in their report were used to represent a fluid inclusion chemistry and brine weep chemistry. We also report simulations of the 13 new brines from the BATS experiment analyzed in this report.

We tested the ability of low NMR to measure brine distribution in salt. A Magritek NMR Mouse instrument was used to measure the distribution of relaxation times T_2 of water isolated in a salt core from the BATS experiment before and after heating. The data show the presence of two populations of water in the salt core. The first population of water with a shorter relaxation time (ca. 1 to 5 msec) represents the tightly bound water or water within small pores while the second population of water with a larger relaxation signal (45 to 54 msec) represents the free water isolated in inclusions. The water distribution inhomogeneous and there is significantly more free water than tightly bound water in the salt core. Characterization of the hot and cold sides of the salt core before heating shows that the side of the core that would be heated started with relatively more brine inclusions (longer T_2) than the side that remained colder (Figure 2-12). After heating, the relative amount of brine inclusions (longer T_2) on the heated side decreased (drop in signal intensity). We also observed a shortening of the T_2 possibly indicative of a tightening of the pore structure or partial dehydration of the minerals. The NMR data show a consistency of the relaxation times before and after heating, which might indicate very little changes in brine chemistry because of heating. However, significant changes in the relative intensities of the different population of water were observed following heating. We recorded a significant reduction of the amount of free water relative to bound water. The conclusion from these studies indicate that heating preferentially drives the loss of water inclusions and this could be measured using the NMR mouse and T_2 experiments.

2.2 Timetable of the BATS experiment: history of brine sampling

Details of the BATS experiment are reported in the FY-20 Sandia report (Kuhlman et al., 2020). Here we provide a short description of the BATS test site development and history of brine collection to support the brine chemistry detailed in this report. The timetable of the BATS experiment is summarized in Table 2-1.

Table 2-1 Timetable showing the time of BATS boreholes and related dates of brine samples collection.

Date	Action	Filter
2/7/2019	borehole drilling started	drilling
4/19/2019	borehole drilling completed	drilling
4/24/2019	Initial brine samples collection brine	brine collection
5/6/2019	brine volume measurements	brine volume
5/22/2019	brine volume measurements	brine volume
6/24/2019	brine volume measurements	brine volume
7/1/2019	brine sample collected from unheated array D borehole	brine collection
7/1/2019	brine sample collected from unheated array F2 borehole fiber optic wires	brine sample
7/23/2019	brine volume measurements	brine sample
9/4/2019	brine volume measurements	brine volume
9/11/2019	brine volume measurements	brine volume
12/17/2019	brine volume measurements	brine volume
1/21/2020	start heating heated HP borehole	heating
1/30/2020	brine volume measurements	brine volume
1/30/2020	brine sample collected from heated and unheated SM boreholes	brine sample
2/6/2020	brine sample and brine precipitate collected from heated array borehole F2 wires	brine sample
2/12/2020	brine volume measurements	brine volume
2/12/2020	brine sample collected from heated array SM borehole	brine sample
2/18/2020	end heating heated HP borehole	heating
2/24/2020	brine sample and brine precipitate collected from heated array borehole F2 wires	brine sample
4/23/2020	brine sample collected from heated array D borehole	brine sample

Brine volume measurement did not always yield brine samples. Figure 2-1 shows a plot of the different sampling events and the amount of brine collected for brine analyses.

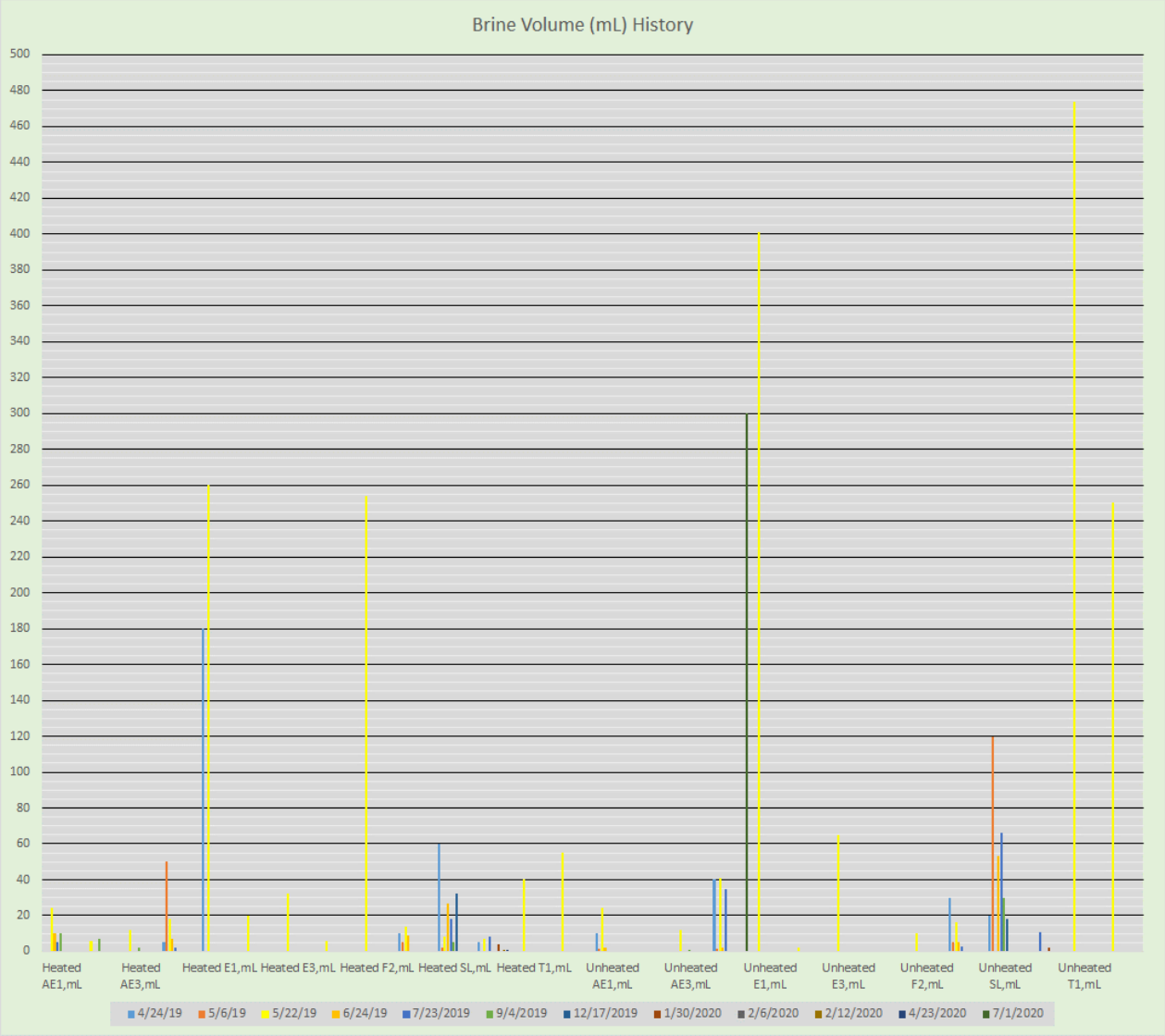

Figure 2-1. History of brine sampling for the BATS experiment

The plot shows that the amount of brine accumulated in the boreholes varied significantly between boreholes. Brine samples were collected using a vacuum pump system described in details in the BATS experimental setup (Kuhlman et al., 2020). The samples were sealed immediately after sampling to minimize evaporation

2.3 Chemistry of WIPP brines

2.3.1 Overview of chemistry of WIPP brines from historical data

The interest in brines composition in the context of nuclear waste repositories stems from the need to predict the potential reactions of brine components with emplaced transuranic waste

(Hansen and Leigh, 2011). Brine chemistry defines the solubility of actinides and potential formation of colloidal species and has a strong impact on the performance assessment of the repository. It is therefore important to characterize the chemistry of the brines and develop an understanding of their evolution in the geochemical environment of the repository. There are three different populations of brines associated with bedded salt at WIPP. The first population of brines is isolated in the salt crystals in the form of millimeter-sized inclusions. These brine inclusions are in equilibrium with the NaCl salt matrix and have no apparent interaction with the accessory minerals present in salt in today's environment. Their chemical composition is defined by the chemistry of the brines that existed at the time of their formation and diagenetic processes and recrystallizations that might have occurred over time (Bein et al., 1991; Braitsch, 2012; Colon et al., 2012; Deal et al., 1991; Garcia-Veigas et al., 1992; Hardie, 1968, 1982; Stein and Krumhansl, 1986). Their chemical composition varies significantly (Table 2-2). A representation of the data from Table 2-2 as metal ratios of the most prevalent elements is presented in Figure 2. The graphical representation of the fluid inclusions in Figure 2 illustrates the brine inclusions compositional variability. The brine inclusions data can be grouped into two groups. The first group is characterized by a low Na/Cl at ~ 0.15 and low K/Mg at ~0.2 and the second group is characterized by a Na/Cl and K/Mg at ~0.4. Inclusions in the first group separate from the second group by their high magnesium content and low sodium content relative to the second group. By comparison the Na/Cl and K/Mg ratios in sea water are 0.55 and 0.3 respectively. This is indicative of significant recrystallizations of the brines after their isolation within the inclusions in group I. The brines are significantly enriched in Mg and depleted in Na relative of the average sea water composition. This might also indicate rapid crystallization of the salt and isolation of brines that were initially far from a chemical equilibrium. Some diagenesis might have also affected the inclusions chemistry especially in the salt layers rich in clays and other minerals. The inclusions in group II have Na/Cl ratio close to the average seen in sea water, which could indicate that these inclusions have been formed under normal seawater saturation conditions and might have not experienced recrystallization as in group I inclusions.

Table 2-2 Summary of selected brine inclusions analyses obtained from WIPP at the repository level. Inclusions composition is expressed in g/L. All data were taken from Stein and Krumhansl, (1986).

Fluid Inclusions	Ca^{2+}	Mg^{2+}	K^{+}	Na^{+}	Cl^{-}	Br^{-}	SO_4^{2-}	- charge	+ charge	difference
1	2.5	31.5	12.3	91.3	191	1.5	23	5.88	7.00	1.12
2	0.54	54.1	8.5	32.1	196	5.3	22.4	6.05	6.09	0.04
3	0.17	40.4	6.7	31.3	161	2	17.8	4.93	4.87	-0.07
4	0.23	22.7	8.7	61.8	163	1.3	21.4	5.05	4.79	-0.26
5	0.18	15.6	11.5	81.3	161	0.9	24.5	5.06	5.12	0.06
6	0.21	21.4	8.1	66	163	1.8	26	5.16	4.85	-0.31
7	0.35	23.3	10.9	66.9	161	1.4	21	4.99	5.12	0.13
8a	0.14	40.9	7	31.7	153	2.2	17	4.69	4.93	0.24
8b	0.15	37.9	6.6	33.7	153	2.2	17	4.69	4.76	0.07
8c	0.15	40.8	7	32.6	162	2.3	18	4.97	4.96	-0.01
9	0.22	25	8.8	56.6	165	1.3	22	5.12	4.75	-0.37

10	0.18	22	9.3	66.2	161	1.2	22	5.01	4.94	-0.07
11	0.19	29.1	9.2	59	192	1.6	25.2	5.95	5.21	-0.75
12	0.29	15.2	13.1	92.3	177	0	23.2	5.47	5.61	0.14
13	0.28	29.1	10.5	56.2	159	1.6	19	4.89	5.12	0.23
14	0.23	28.1	9.2	52.4	168	1.5	18.5	5.14	4.84	-0.30
15	0.22	26.3	9.7	60.7	184	1.4	18.7	5.59	5.06	-0.53
16	0.27	24.2	9.7	63.8	171	1.9	26	5.38	5.03	-0.36
17	0.26	24.2	9.7	63.8	172	1.4	19.5	5.27	5.03	-0.24
18	0.31	15.7	6.4	78.5	167	0	17.4	5.07	4.88	-0.18

The second population of brines from the WIPP facility horizon exists in the form weeps and accumulates in boreholes and as visible puddled water. The chemical composition of these brines has less variability compared to fluid inclusions (Figure 2-2).

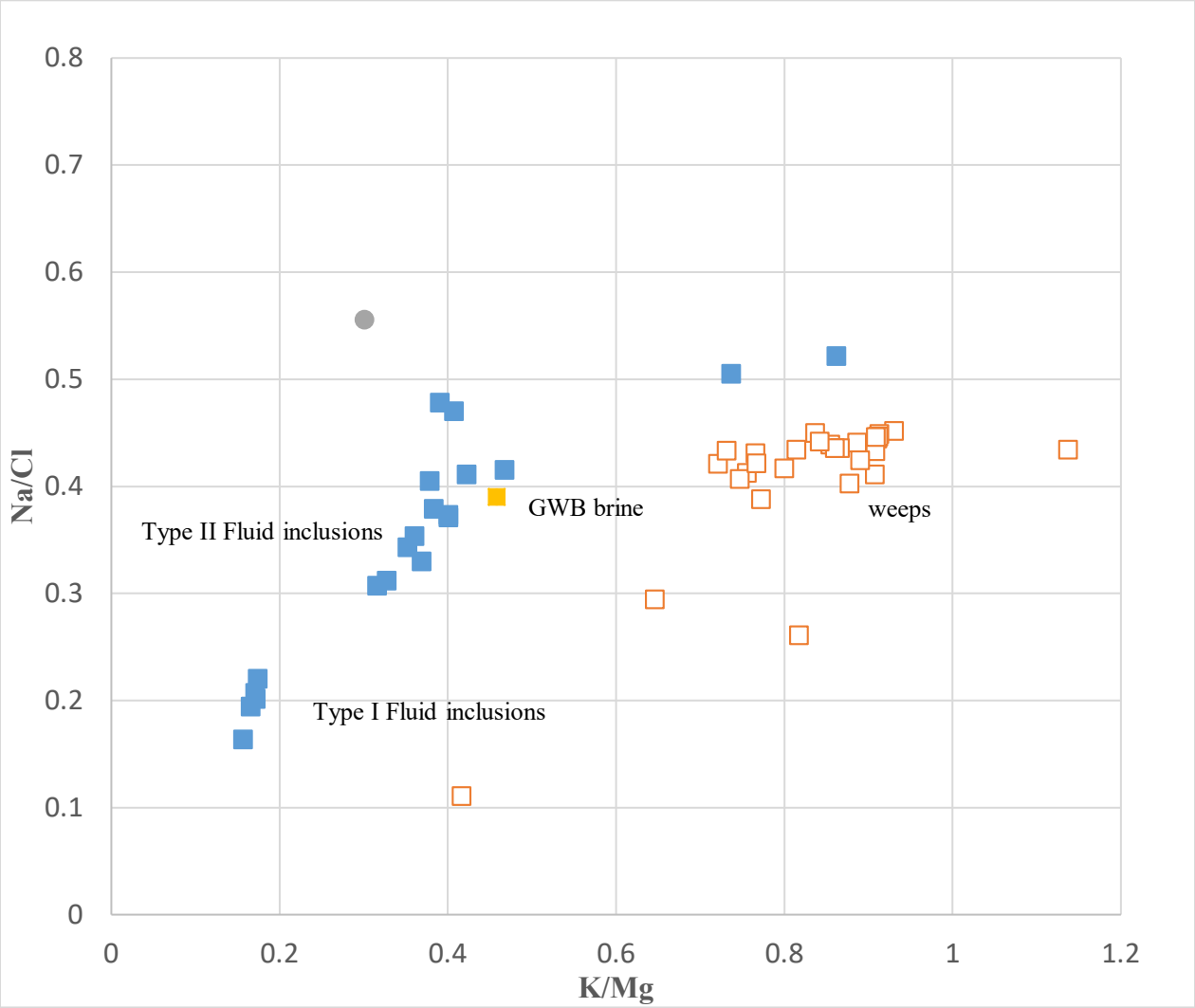

Figure 2-2. Plot of major elements ratios representing various fluid inclusions and commonly sampled brine from WIPP related studies.

The representation of the weep brines chemistry data as metal ratios shows that weep brines are slightly depleted in magnesium and slightly enriched in potassium relative to brine inclusions. This is an indication of the re-equilibration of the brines with observed repository minerals such as halite, anhydrite, magnesite, polyhalite representing close to 10% of the of the salt in the WIPP horizon brine that has been equilibrated with.

The plot in Figure 2-2 also shows the representation of the GWB brine which is the most widely used brine in transuranic studies related to WIPP. The GWB brine groups with the inclusions type II. The charge balance from the historical data shows some charge imbalance which is indicative of analytical uncertainties originating from the large dilutions needed to perform the analyses on the anion chromatography.

The third population of brines is tightly associated with the accessory minerals present in salt. There are no data that directly characterized these brines. They are tightly associated with hydrated minerals and might not directly migrate to excavations in salt. However, there are some indications from our recent NMR studies that water associated with salt minerals exchanges quite rapidly with the free and mobile water in salt. Therefore, the water associated with hydrated minerals might also indirectly be available for migration through exchange processes.

2.3.2 Chemistry of brine samples from the East and West arrays of the BATS experiment

Brine samples were collected from both the East (unheated) and west (heated) arrays of the BATS experiment when available. Boreholes were isolated by packer systems to minimize evaporation and the influence of ambient tunnel air. Sampling was performed by pumping the brines through tygon tubing connected to the back of the boreholes (Kuhlman et al., 2020). The brines were filtered, acidified, and diluted one million times to prepare samples for cation and anion analyses.

The volume of brine produced by different boreholes and sampling date are presented in Figure 2-1 and Table 2-1. Sampling was performed periodically over the initial stage of the experiment. The first set of samples were collected immediately after the completion of the drilling (Table 1-1). The sampling locations sample names and dates are summarized in Table 2-3. The brine chemistry data of the major elements are summarized in Table 2-4.

Table 2-3 Summary of brine samples collected from the BATS experiment heated and unheated arrays before heating

Sampling location	Sampling date	Sample name
UE1 (E. Array)	Aril 24, 2019	U-E1-4-18-19
UD (E. Array)	Aril 24, 2019	U-D-4-18-19
USL (E. Array)	Aril 24, 2019	U-SL-4-18-19
HE2 (W. Array)	Aril 24, 2019	H-E2-4-18-19
UHP (E. Array)	Aril 24, 2019	U-HP-4-18-19
HHP (W. Array)	Aril 24, 2019	H-HP-4-18-19
HAE2 (W. Array)	Aril 24, 2019	H-AE2-4-18-19
UT2 (W. Array)	Aril 24, 2019	U-T2-4-18-19
UES (E. Array)	Aril 24, 2019	U-ES-4-18-19
HT1 (W. Array)	Aril 18, 2019	H-T1-4-18-19

Table 2-4 Summary of brine analyses performed on the first samples obtained from the East and west array boreholes sampled on 4-18-2019. All concentrations are in g/L.

Sample	Ca^{2+}	Mg^{2+}	K^{+}	Na^{+}	Cl^{-}	Br^{-}	SO_4^{2-}	-charge	+ charge	difference
U-E1-4-18-19	0.28	23.88	15.17	70.80	138	0.76	11.8	3.91	5.45	1.53
U-D-4-18-19	0.25	19.24	12.30	53.29	143	0.80	12.4	4.06	4.23	0.17
U-SL-4-18-19	0.26	21.59	13.51	61.17	199.	1.13	17.0	5.64	4.79	-0.84
H-E2-4-18-19	0.23	19.59	12.18	50.93	157.	0.92	13.7	4.44	4.15	-0.29
U-HP-4-18-19	0.41	24.72	15.37	64.73	184.	1.12	16.2	5.21	5.26	0.05
H-HP-4-18-19	0.26	22.77	14.34	62.22	193.	1.11	16.6	5.48	4.96	-0.52
H-AE2-4-18-19	0.12	7.99	5.28	23.75	73	0.36	6.31	2.07	1.83	-0.24
U-T2-4-18-19	0.23	19.48	12.61	58.11	172	0.99	14.9	4.87	4.46	-0.41
U-ES-4-18-19	0.23	19.66	12.46	56.44	178	1.03	15.5	5.05	4.40	-0.65
H-T1-4-18-19	0.25	19.99	12.80	58.81	182	1.03	15.6	5.16	4.54	-0.62

A plot of the data along with the historical WIPP brine data is shown in Figure 2-3.

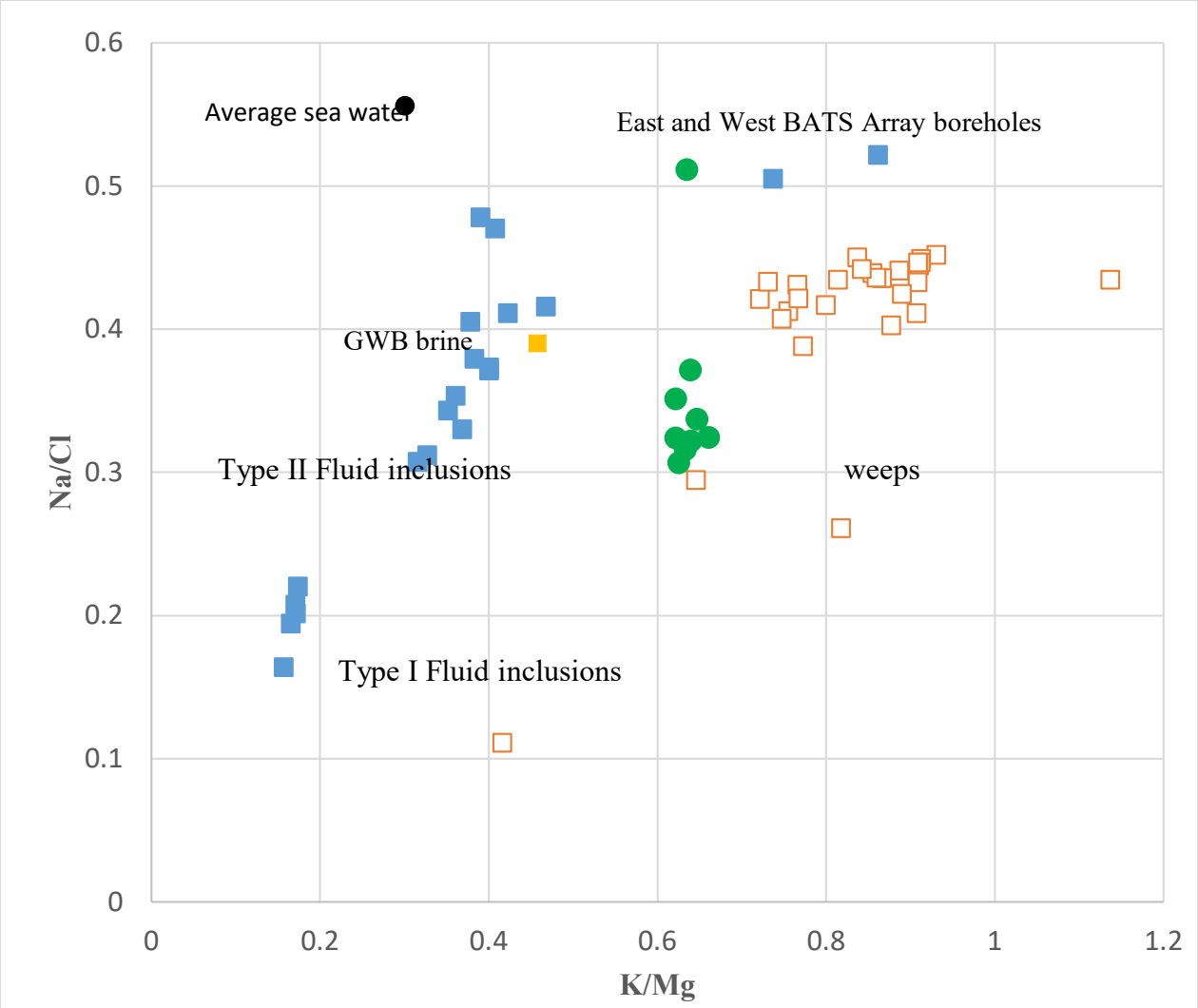

Figure 2-3. Plot of major elements ratios representing East and West array boreholes from the BATS along with various fluid inclusions and commonly sampled brine from WIPP related studies. The BATS samples were obtained on 4-24-2019 immediately after completion of the boreholes (green circles).

The brine samples from the BATS boreholes are grouped together at ~ 0.65 K/Mg and 0.35 Na/Cl. One sample has a very high Na/Cl ratio that plots outside of the group. It is unusual to have strong deviations in brine compositions from samples collected from the same location at the same sampling time. This deviation might be due to analytical errors. The Na/Cl ratio is consistent with a composition similar to type II brine inclusion. However, the K/Mg ratio is higher that the ratio observed for type II inclusion. This trend is consistent with the re-equilibration of the brines observed in other boreholes and weeps analyzed in past studies (Figure 2.2). The shift in K/Mg ratio is mainly driven by a slight increase in potassium content.

The second set of brine samples was collected from various borehole from the heated and unheated arrays of the bats experiment at various times from May to December (Table 2-5). All

the samples were collected before the start of the heating experiment. The chemical composition of the brines is summarized in Table 2-6 and plotted in Figure 2-4 along with the historical data and the earlier brine data collected in April.

Table 2-5 Summary of brine samples collected from the BATS experiment heated and unheated arrays before heating.

Sampling location	Sampling date	Sample name
AE3 heated array	September 2019	H-AE3-9-19
AE1 heated array	September 2019	H-AE1-9-19
E3 unheated array	September 2019	U-E3-9-19
AE2 Heated array	September 2019	H-AE2-9-19c
Seal test borehole heated array	September 2019	H-Seal test brines
Seal test borehole unheated array	September 2019	U-Seal test hole
AE2 Heated array	September 2019	H-AE2-9-19c
SL heated array	December 17 2019	H-SL-12-19
SL unheated	December 17 2019	U-SL-12-19

Table 2-6. Analyses of brines from BATS collected from different boreholes before heating.

Sample	Ca^{2+}	Mg^{2+}	K^{+}	Na^{+}	Cl^{-}	Br^{-}	SO_4^{2-}	- charge	+ charge	difference
H-AE3-9-19	0.29	23.7	15.0	70.2	262	1.64	26.5	7.97	5.41	2.55
H-AE1-9-19	0.28	23.1	14.7	71.3	325	2.08	30.4	9.81	5.40	4.42
U-E3-9-19	0.41	17.7	12.7	79.2	196	1.28	20.8	5.98	5.25	0.74
H-AE2-9-19c	0.33	17.7	12.1	70.6	195	1.27	18.2	5.89	4.86	1.04
H-Seal test brines	0.24	20.3	12.6	61.8	263	1.90	24.7	7.97	4.70	3.27
U-Seal test hole	0.26	24.0	14.6	69.4	189	1.82	17.9	5.73	5.38	0.35
H-SL-12-19	0.29	20.9	12.6	68.6	183	1.17	10.0	5.40	5.04	-0.36
U-SL-12-19	0.24	20.9	12.1	64.1	178	1.14	10.1	5.26	4.83	-0.43

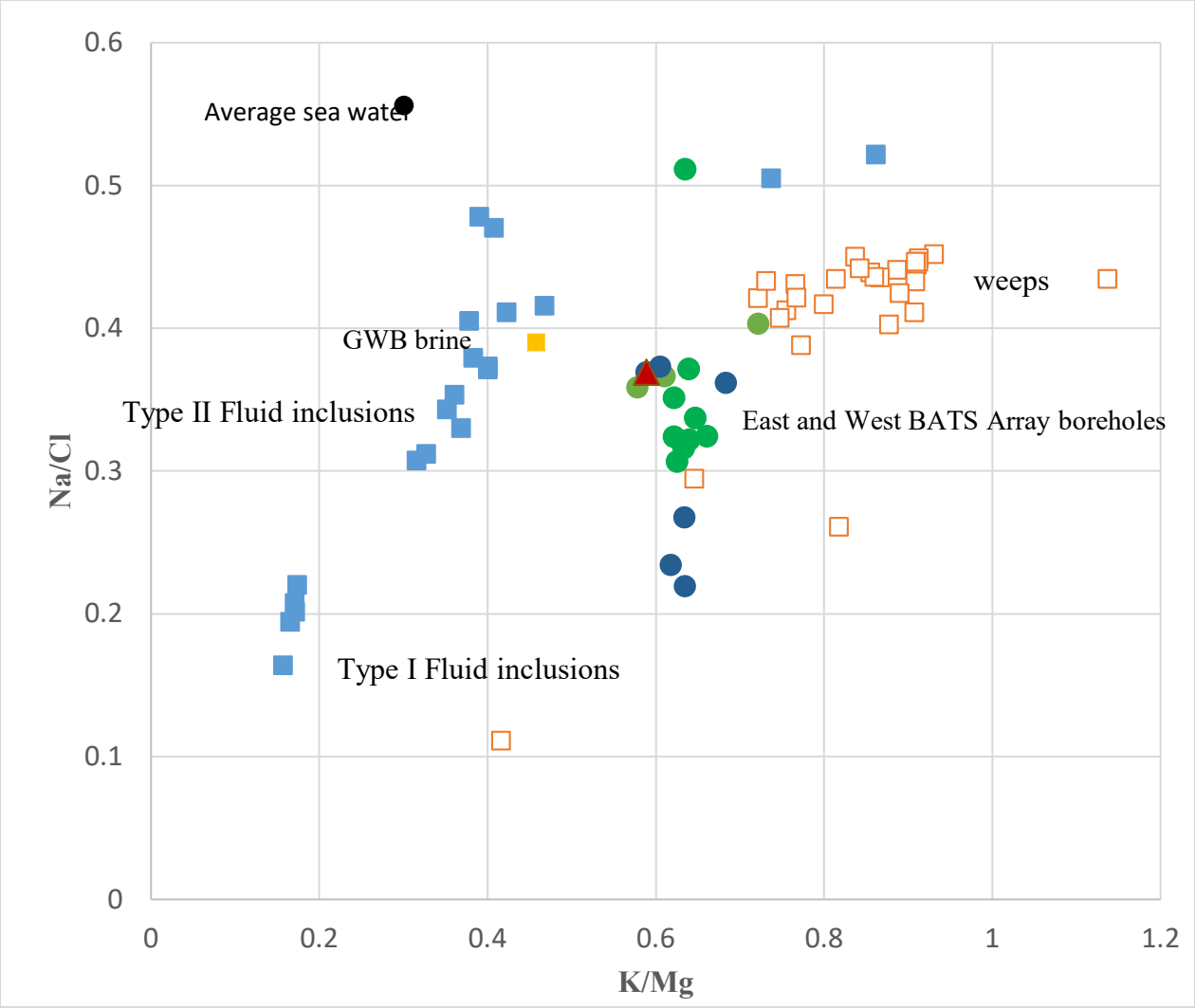

Figure 2-4. Plot of major elements ratios representing various fluid inclusions and commonly sampled brine from WIPP related studies. The plot includes historical data (squares) and brines from the BATS experiments samples at different times before heating over 9 moths (green and blue circles).

The brine data from the September and December sampling have a consistent K/Mg ratio of ~ 0.65 and similar to the early samples. However, the Na/Cl ratio varies significantly. This variability can be due to the re-equilibration of the brines in contact with the salt rock but can also be due to analytical uncertainties in the Na analyses. The large variability observed in the data might also be related to analytical errors and a careful re-evaluation of the analytical results might be beneficial. Although we have presented the data in this update, we are planning to rerun all the brine samples reported here to check for analytical accuracy. The re-analysis will insure these shifts are not from analytical uncertainties related to the large Na concentrations in the samples.

We analyzed a single sample from borehole D in April 2020 after the completion of the first heating experiment. The brine chemistry from borehole D is presented in Table 2-6 and is shown in Figure 2-4 as a red triangle. The sample does not show any significant variation from the samples collected immediately after the completion of the drilling.

Two additional brine samples collected from unheated array in July 2020 along with brines seeping from thermocouple wires grouted in cement in the F2 boreholes were also analyzed. The brine chemistry data are presented in Table 2-8. The data in Table 2-8 also contain the analysis of a brine sample collected from borehole HP from the shakedown test, which was heated for an extended time during the shakedown test. The summary of the samples collection date and location is summarized in Table 2-7.

Table 2-7. Summary of brine samples collected from the BATS experiment heated and unheated arrays before heating.

Sampling location	Sampling date	Sample name
D heated array	April 4, 2020	H-D-4-23-20
D unheated array	July 9, 2020	U-D-7-9-20
F2 unheated array	July 9, 2020	U-F2-7-9-20
HP-shakedown heated borehole	July 9, 2020	HP-shakedown-7-9-20
F2 FO wires	February 24, 2020	H-F2 FO wires-2-24-20
F2 FO wires	February 6, 2020	H-F2 FO wires-2-6-20

Table 2-8. Analyses of brines from BATS collected from different boreholes before heating.

Sample	Ca^{2+}	Mg^{2+}	K^{+}	Na^{+}	Cl^{-}	Br^{-}	SO_4^{2-}	- charge	+ charge	difference
H-D-4-23-20	0.35	20.1	11.8	68.9	186	1.07	11.3	5.52	4.98	-0.53
U-D-7-9-20	0.34	23.6	15.4	1.21	232	1.63	22.6	7.03	6.01	1.02
U-F2-7-9-20	0.02	0.00	26.7	118.	215	0.86	59.0	7.31	5.85	1.46
HP-shakedown	0.26	37.3	22.3	61.2	245	2.57	38.4	7.74	6.32	1.42
H-F2 FO wires-2-24-20	6.43	1.06	13.5	96.5	202	0.81	1.21	5.74	4.95	-0.79
H-F2 FO wires-2-6-20	4.84	0.00	5.7	23.8	48	0.29	1.74	1.40	1.42	0.02

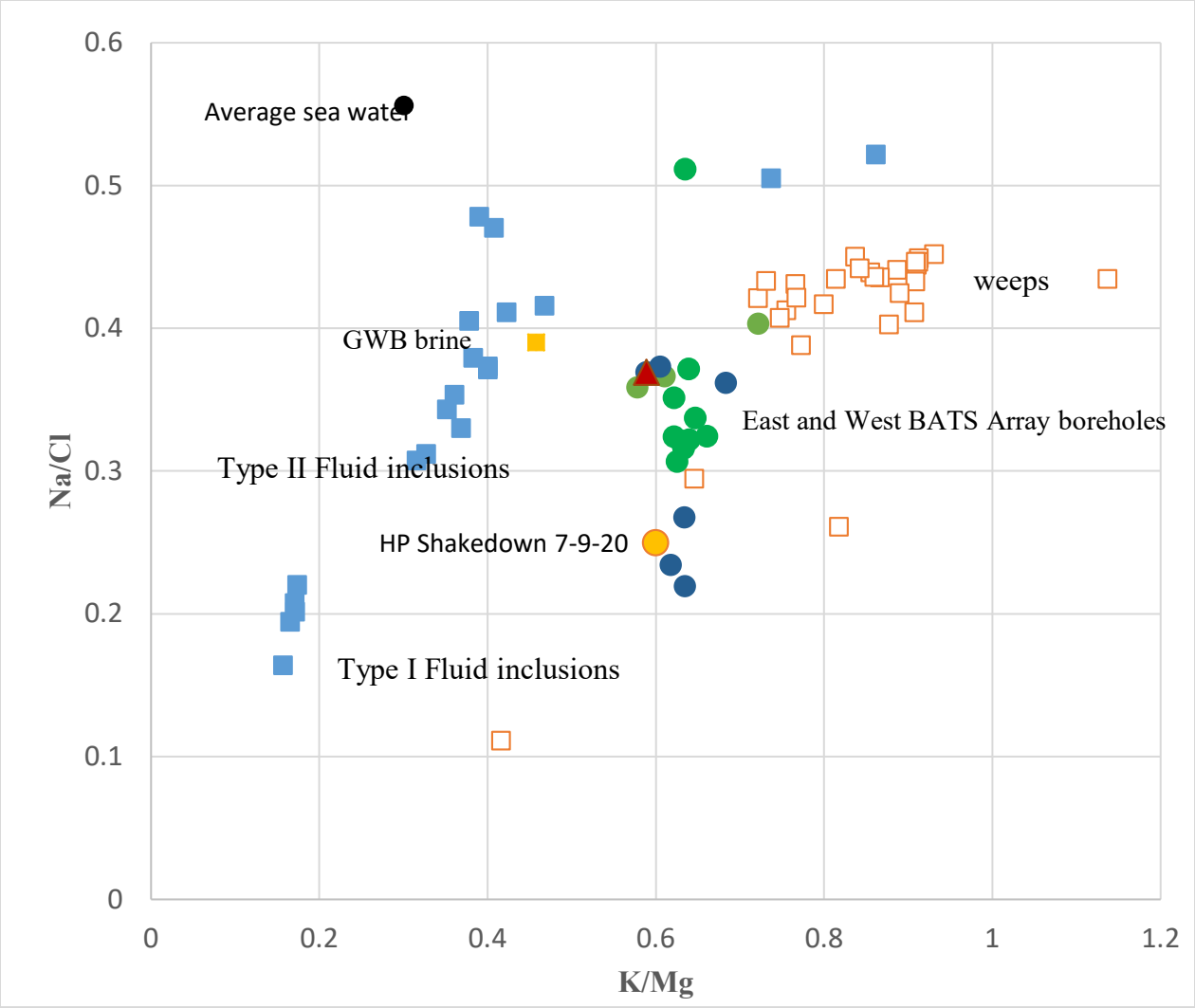

Figure 2-5. Plot of major elements ratios representing various fluid inclusions and commonly sampled brine from WIPP related studies. The plot includes the sample from the shakedown test (orange circle).

The brine sample from the shakedown test has a K/Mg consistent with all the data obtained from the BATS experiment. However, the Na/Cl ratio is shifted towards lower values due to a high Cl^- values.

2.3.3 Geochemical modeling of brine chemistry

PHREEQC was used to calculate thermodynamic equilibrium saturation indices of minerals relevant to the WIPP brines. We first setup the model using synthetic brines such as GWB, ERDA and other brines used extensively in WIPP related studies. We performed calculation for the bines inclusions and brine weeps reported in historical reports from Sandia National Laboratory (Lucchini et al., 2013; Stein and Krumhansl, 1986), and for the brines

sampled from the BATS experiment. The purpose of the modeling exercises was to investigate the precipitation of minerals and examine the shift of ionic ratios of brines as they are transported through the salt as under the influence of mechanical or thermal disturbances. Brine volumes reduction through evaporation or the formation of mineral hydrates (such as Gypsum or Goergyte), which can impact the solution chemistry have not been implemented in calculations. In addition, gas bubbles, which are ubiquitous in the fluid inclusion, are assumed to remain constant even though increases in temperature would lead to degassing of aqueous CO_2 which in turn would affect pH and mineral solubilities.

For the initial calculations presented in this report we used the Pitzer database (Appelo, 2015; Appelo et al., 2014), which we believe is the most consistent database for geochemical calculations at high ionic strength and allows calculations of temperature effects. The default PHREEQC database uses the Debye-Hückel equation to calculate molar activities, which only remains accurate for ionic strengths of <0.1. In addition, the solution density was adjusted to 1.21 kg/m^3 as described in (Lucchini et al., 2013). The water chemistry was allowed to equilibrate with a bubble of air (78% N_2, 20% O_2, 0.04% CO_2) composing roughly 20 % of the volume at temperature 25 °C with a pressure of 1 atmosphere. Large charge imbalances (+/- 1 mol) were also found in several samples, which PHREEQC was allowed to balance by adjusting Cl^- concentrations in the initial solution composition. Most of the brine samples did not have values for pH and alkalinity, and as a consequence values of pH of 6.5 and HCO_3^{1-} concentration of 701 mg/l were used instead. We used synthetic brines (Brine A, G-Seep, GWB, ERDA) used in WIPP studies to setup the PHREEQC thermodynamic calculations of the properties for the concentrated brines at variable temperature ranging from 5 °C to 85 °C. We calculated saturation indices for Polyhalite, Magnesite, Anhydrite, Gypsum, Halite, Brucite, Huntite, and Dolomite in order to provide an understanding of the evolution of the brines as a function of temperature. Saturation indexes for all possible mineral species were computed for a temperature range of 5° C to 85 °C.

We present the thermodynamic equilibrium calculations of the different brines focusing the saturation indices of the different mineral species in equilibrium with brines. At this stage of our model development we did not perform any checks on completion of the database as this relates to specific mineral species that are relevant WIPP brines. We are currently checking the database for completion and self-consistency and reviewing the literature to compile data on several sulfate and hydroxysulfate mineral phases that are relevant to WIPP brines. After completion of the data collection we will perform validation calculations for single and binary mineral phases with data from the literature to check for consistency. The result of the calculations for GWB is summarized in Table 2-9 and Figure 2-6. The thermodynamic calculations for the ERDA, Brine A, G-seep, were also performed are reported in Appendix 1, along with the chemical composition of the synthetic brines used as input parameters for the thermodynamic calculations. Negative values indicate dissolution and positive values indicate precipitation

Table 2-9. PHREEQC calculation of mineral saturation of the main minerals susceptible to undergo significant precipitation/dissolution for GWB brines under variable temperatures.

GWB Temp	Polyhalite	Magnesite	Anhydrite	Goergeyite	Gypsum	Halite	Brucite	Huntite	Dolomite
5	-0.12	2.32	-0.04	6.77	0.26	0.08	-4.20	5.61	3.40
15	-0.22	2.36	0.04	5.73	0.21	0.07	-3.67	6.35	3.68
25	-0.40	2.37	0.10	4.81	0.15	0.06	-3.20	7.01	3.90
40	-0.82	2.35	0.17	3.60	0.05	0.02	-2.61	7.87	4.11
55	-1.38	2.29	0.22	2.56	-0.06	-0.02	-2.12	8.64	4.22
70	-2.07	2.20	0.25	1.68	-0.17	-0.05	-1.73	9.33	4.24
85	-2.86	2.07	0.26	0.91	-0.29	-0.09	-1.42	9.97	4.18

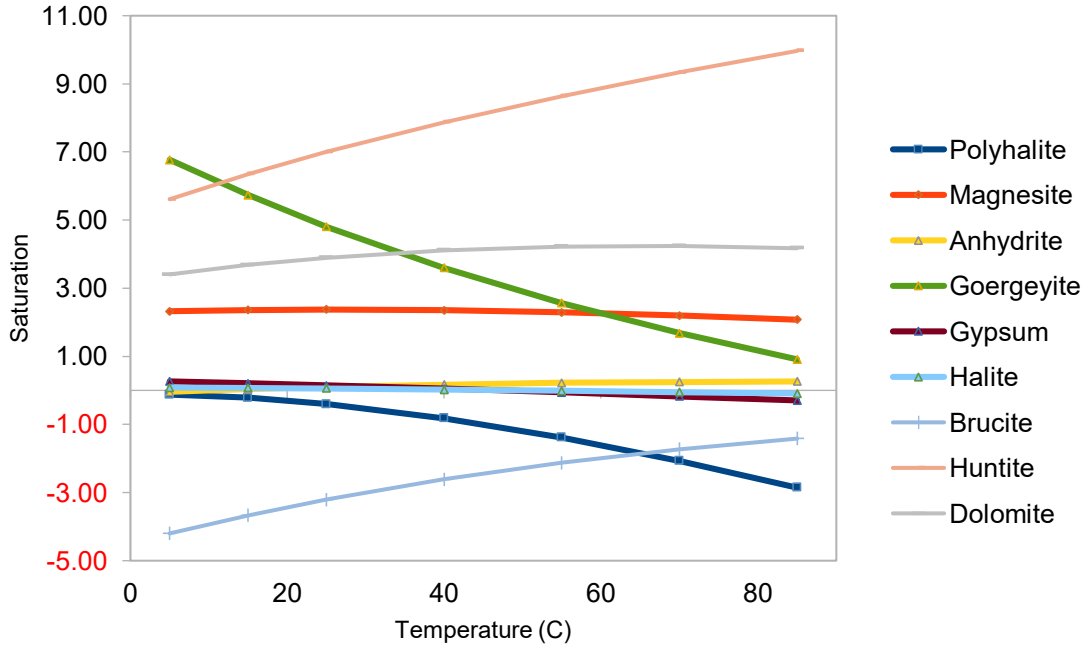

Figure 2-6. Graphical representation of the saturation indices of the different minerals relevant to GWB brine. The chemical formula of the different minerals are as follows: Polyhalite $K_2Ca_2Mg(SO_4)_4 \cdot 2H_2O$, Magnesite $MgCO_3$, Anhydrite $CaSO_4$, Gypsum $CaSO_4 \cdot 2H_2O$, Halite NaCl, Brucite $Mg(OH)_2$, Goergeyite $K_2Ca_5(SO_4) \cdot 6H_2O$, Huntite $CaMg_3(CO_3)_4$, Dolomite $CaMg(CO_3)_2$.

Our calculations show that the GWB brine is unsaturated in Polyhalite ($K_2Ca_2Mg(SO_4)_4 \cdot 2H_2O$) and that the unsaturation increases with temperature. GWB brine is also unsaturated in Brucite $Mg(OH)_2$, but the unsaturation decreases with temperature because of the pH increase due to CO_2 degassing retrograde solubility of Brucite. GWB brine is found to be oversaturated in a number of other minerals such as Dolomite $CaMg(CO_3)_2$, Huntite $CaMg_3(CO_3)_4$, and Magnesite $MgCO_3$. The oversaturation in these minerals is not significantly reduced with temperature and as a consequence of this disequilibrium precipitation of these mineral may occur as the brine equilibrates. The consequences of the re-equilibration reactions will determine the concentrations

of Ca, Mg, and K that define the brines. These re-equilibration reactions are pH and alkalinity dependent highlighting the importance of accurate measurement of these parameters for brines.

We also performed thermodynamic equilibrium calculations for all the brine samples obtained from the BATS experiment. An example of the calculated saturation indices obtained for the U-D-4-18-19 sample obtained from borehole D of the east array as well as the calculations for the sample collected from the HD borehole of the shakedown test are presented in Table 2-10. The thermodynamic calculations for the all the BATS related samples are presented in Appendix 1.

Table 2-10. Thermodynamic equilibrium calculations by PHREEQC the main minerals susceptible to undergo significant precipitation/dissolution for brines sampled from the bats experiment U-D-4-18-19 and the shakedown.

U-D-4-18-19									
Temp	Polyhalite	Magnesite	Anhydrite	Goergeyite	Gypsum	Halite	Brucite	Huntite	Dolomite
5	-3.43	1.56	-1.05	1.33	-0.59	-0.69	-5.01	2.52	1.84
15	-3.41	1.65	-0.94	0.47	-0.61	-0.69	-4.42	3.46	2.21
25	-3.48	1.71	-0.84	-0.27	-0.64	-0.70	-3.90	4.29	2.51
40	-3.71	1.75	-0.71	-1.19	-0.68	-0.72	-3.23	5.39	2.84
55	-4.08	1.74	-0.60	-1.91	-0.73	-0.75	-2.67	6.38	3.06
70	-4.56	1.70	-0.51	-2.47	-0.79	-0.77	-2.20	7.26	3.17
85	-5.15	1.62	-0.43	-2.92	-0.86	-0.79	-1.82	8.07	3.19

HP Shakedown									
Temp	Polyhalite	Magnesite	Anhydrite	Goergeyite	Gypsum	Halite	Brucite	Huntite	Dolomite
5	1.52	2.50	0.10	8.05	0.35	0.18	-3.68	5.65	3.09
15	1.28	2.50	0.13	6.76	0.25	0.16	-3.17	6.24	3.29
25	0.96	2.49	0.14	5.59	0.14	0.13	-2.73	6.77	3.44
40	0.34	2.43	0.15	4.03	-0.01	0.08	-2.16	7.50	3.57
55	-0.42	2.34	0.14	2.66	-0.18	0.04	-1.71	8.13	3.61
70	-1.30	2.20	0.11	1.45	-0.35	-0.01	-1.35	8.63	3.52
85	-2.27	1.99	0.06	0.36	-0.53	-0.06	-1.08	8.90	3.27

The saturation indices for the BATS related brine samples is presented in Figure 2-7.

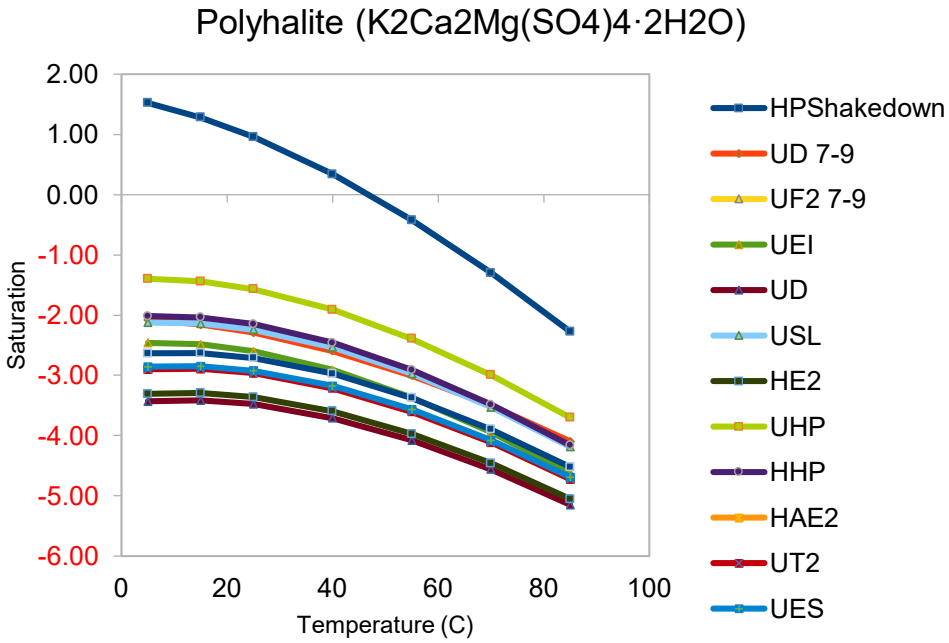
Polyhalite (K2Ca2Mg(SO4)4·2H2O)
2.00
1.00
0.00
-1.00
-2.00
-3.00
-4.00
-5.00
-6.00
Saturation
0
20
40
60
80
100
Temperature (C)
HPShakedown
UD 7-9
UF2 7-9
UEI
UD
USL
HE2
UHP
HHP
HAE2
UT2
UES

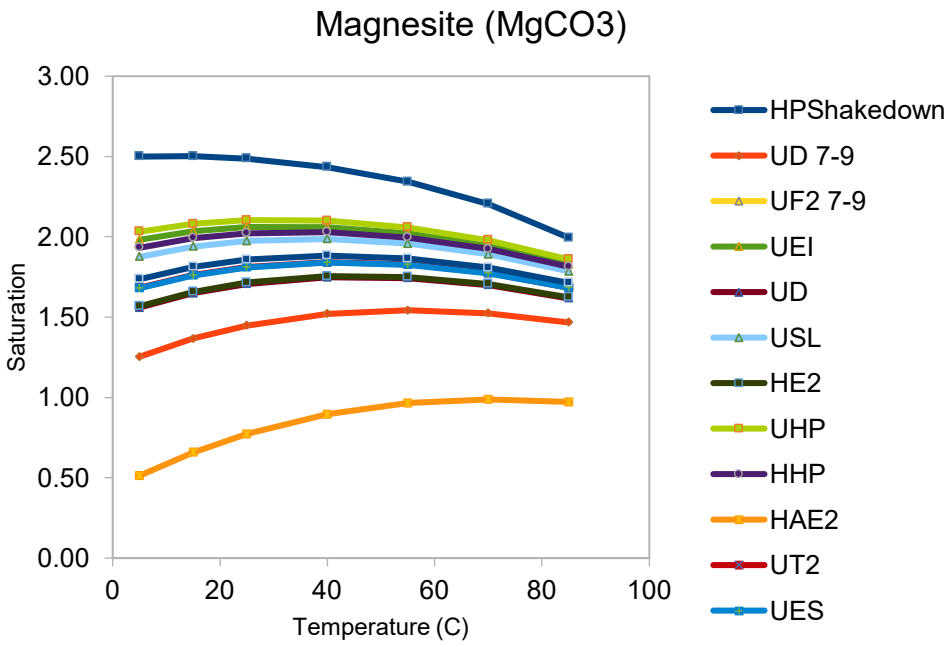
Magnesite (MgCO3)
3.00
2.50
2.00
1.50
1.00
0.50
0.00
Saturation
0
20
40
60
80
100
Temperature (C)
HPShakedown
UD 7-9
UF2 7-9
UEI
UD
USL
HE2
UHP
HHP
HAE2
UT2
UES

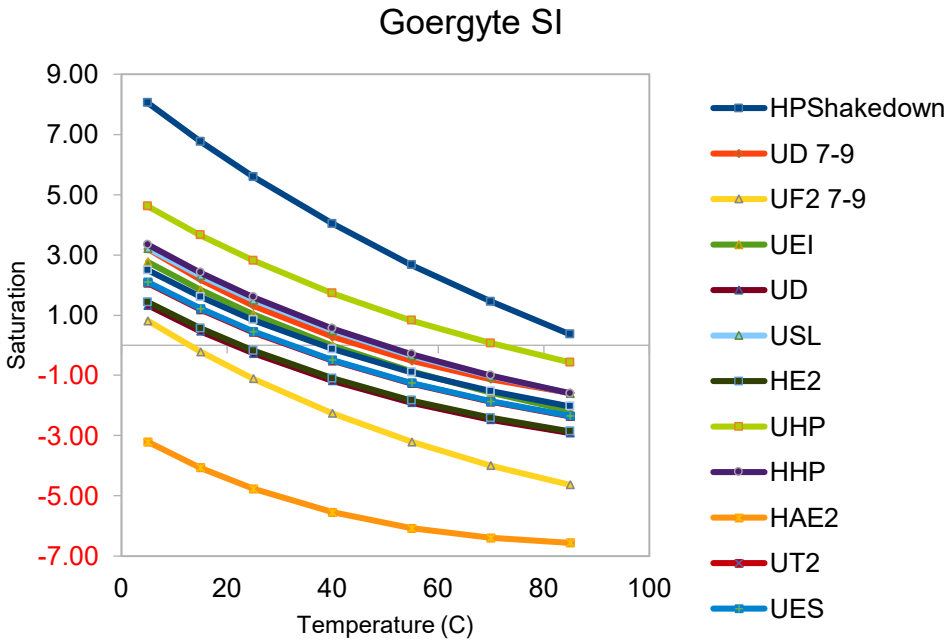
Goergyte SI
9.00
7.00
5.00
3.00
1.00
-1.00
-3.00
-5.00
-7.00
Saturation
0
20
40
60
80
100
Temperature (C)
HPShakedown
UD 7-9
UF2 7-9
UEI
UD
USL
HE2
UHP
HHP
HAE2
UT2
UES

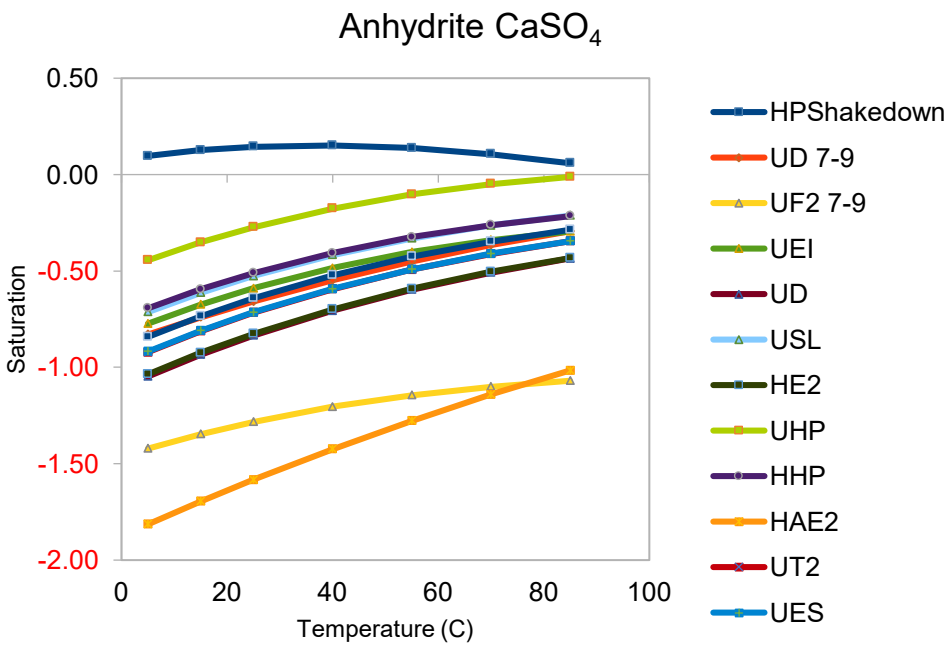
Anhydrite CaSO4
0.50
0.00
-0.50
-1.00
-1.50
-2.00
Saturation
0
20
40
60
80
100
Temperature (C)
HPShakedown
UD 7-9
UF2 7-9
UEI
UD
USL
HE2
UHP
HHP
HAE2
UT2
UES

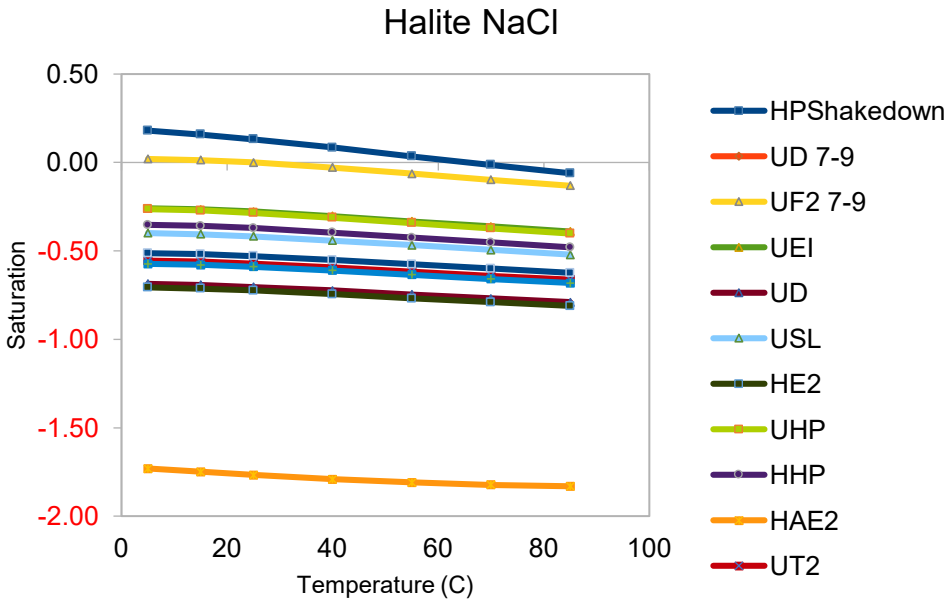
Halite NaCl
0.50
0.00
-0.50
-1.00
-1.50
-2.00
Saturation
0
20
40
60
80
100
Temperature (C)
HPShakedown
UD 7-9
UF2 7-9
UEI
UD
USL
HE2
UHP
HHP
HAE2
UT2

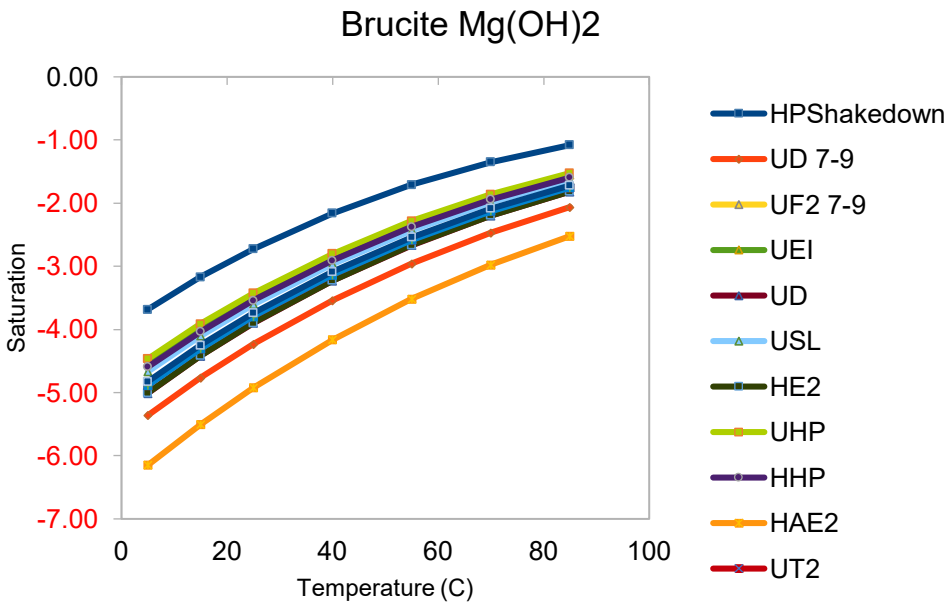
Brucite Mg(OH)2
0.00
-1.00
-2.00
-3.00
-4.00
-5.00
-6.00
-7.00
Saturation
0
20
40
60
80
100
Temperature (C)
HPShakedown
UD 7-9
UF2 7-9
UEI
UD
USL
HE2
UHP
HHP
HAE2
UT2

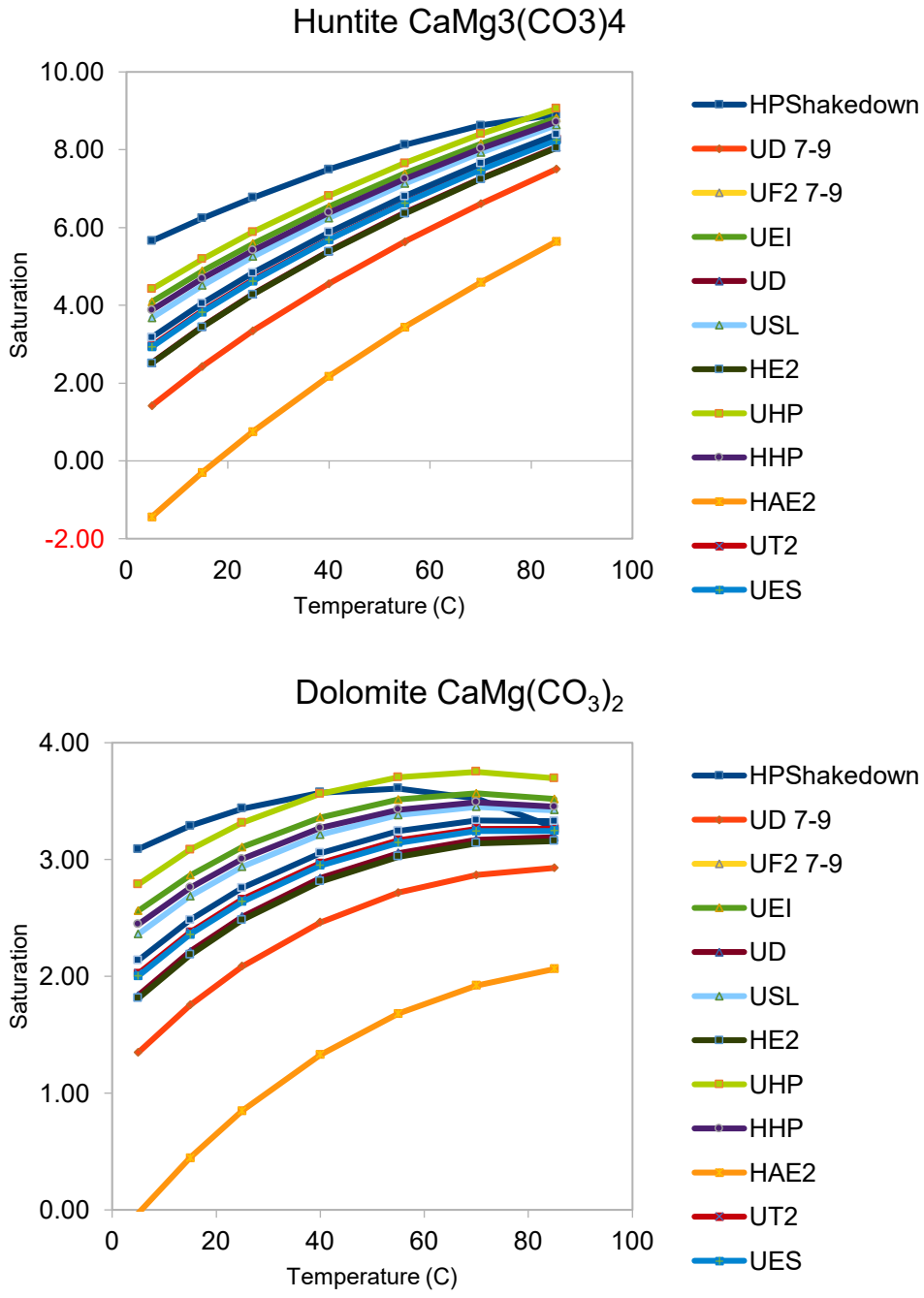

Figure 2-7. Graphical representation of the saturation indices of the different minerals relevant to BATS brines. The chemical formula of the different minerals are as follows: Polyhalite $K_2Ca_2Mg(SO_4)_4 \cdot 2H_2O$, Magnesite $MgCO_3$, Anhydrite $CaSO_4$, Gypsum $CaSO_4 \cdot 2H_2O$, Halite NaCl, Brucite Mg(OH)2, Huntite $CaMg_3(CO_3)_4$, Dolomite $CaMg(CO_3)_2$.

Our calculations show that all BATS brine samples are unsaturated in Polyhalite, Anhydrite and Brucite. They show oversaturation in Magnesite, Huntite, and dolomite. The thermodynamic calculation show very little evolution of the trends of the calcium, magnesium, and sulfate concentrations with temperature. It is not evident from these calculation which mineral phases will ultimately control the brine chemistry. However, it is noteworthy that three carbonate mineral phases (Dolomite, Magnesite, and Huntite) are oversaturated in almost all the brines and that in two of these minerals (Dolomite and Huntite) saturation increases with temperature. Carbonate precipitation leads to a decrease in pH which could potentially impact the brine chemistry, especially if the precipitates become inaccessible to re-equilibration as the inclusions move through the formation. All the brines from the BATS experiment contained precipitated mineral phases. We are in the process of analyzing the mineral composition of the precipitated minerals to help guide the discussion and thermodynamic calculations.

2.4 Characterization of brine migration under temperature gradients using low field NMR

Measuring and mapping the distribution of brine components in salt formations and how they migrate under the influence of thermal and mechanical disturbances is challenging. The complexity arises from the low salt porosity, variable permeability, heterogeneity of the salt layers, as well as varying fluid inclusions composition. Magnetic resonance methods have emerged as a key tool for evaluating petroleum reservoirs by well logging organizations such as Schlumberger (Garcia-Veigas et al., 1992), which use the technique to quantify the petrophysical parameters, and fluid properties at significant depths. Measurement of the nuclear magnetic resonance (NMR) signal relaxation rates (T_1 and T_2) are used to classify fluid compositions in complex formations such as kerogen, bitumen, light/heavy oils, gases and brine. In this context T_1 refers to the rate at which the detectable polarization returns to alignment with the applied magnetic field, and T_2 is the relaxation that causes polarization to decay but it can be reversed with simple echo experiments that are well known in NMR experiments (Song and Kausik, 2019). The measurement of the relaxation time T2 is particularly interesting for salt materials. The T_2 relaxation measurements can be used to quantify spin-spin relaxation and determine relative amounts of occluded, trapped, and bound water. T_2 values are inversely correlated to the viscosity and molecular motion. Short T_2 values are indicative of tightly bound water such as water associated to hydrated minerals and water associated to crystalline structures and long T_2 values are found in liquids phases or free water. Measurement of T2 values in salt specimens can reveal the relative degree of mineral hydration relative to free/bulk water.

In this report we report the characterization of water distribution in short salt core from the BATS experiment (Figure 2-8) prior to heating and following heating for 4 weeks under a temperature gradient. Details of the heating experiment and experimental setup are described in section 2.4.1 and the NMR results of the pre and post heating are described in section 2.4.2.

2.4.1 Experimental Methods

A salt core from the BATS experiment was collected during the drilling operation (Table 1-1) and sealed immediately after coring to preserve its water content (see Kuhlman et al., 2020 for

coring details and preservation) was placed on an aluminum surface in contact with a hot plate. A picture of the experimental setup is shown in Figure 8. The aluminum surface was kept at a constant temperature of 70° C by coupling the power supply of the hot plate to a temperature controller. A thermocouple connected to the aluminum surface provided a feed back to the temperature controller (J-Kchem Scientific) to maintain a constant temperature of the heating surface. The temperature of the hot surface was maintained at the assigned temperature to within ± 1 °C. The entire setup (heating unit, controller, and salt core) was placed on a balance to record the loss of mass in real time. The weight loss resulting from brine migration was recorded every 30 seconds by a computer connected to the balance. Prior to the start of the experiment, the round side of the salt core was covered with an epoxy resin to minimize moisture uptake from the atmosphere during the heating and cooling processes. The “bottom of the core” was filed down to provide a flat surface to increase contact and coupling with the aluminum plate. Six thermocouples (Omega, K Type) were placed alongside the length of the core at 1-2 cm intervals from the bottom to the top of the salt core to measure the temperature of the salt core. The thermocouples were connected to a data logger (Graphtech, midilogger GL220) which recorded the surface temperature of the salt core every 30 seconds. Figure 9 shows the thermocouples along the side of the core, together with temperature values obtained established when the temperatures stabilized.

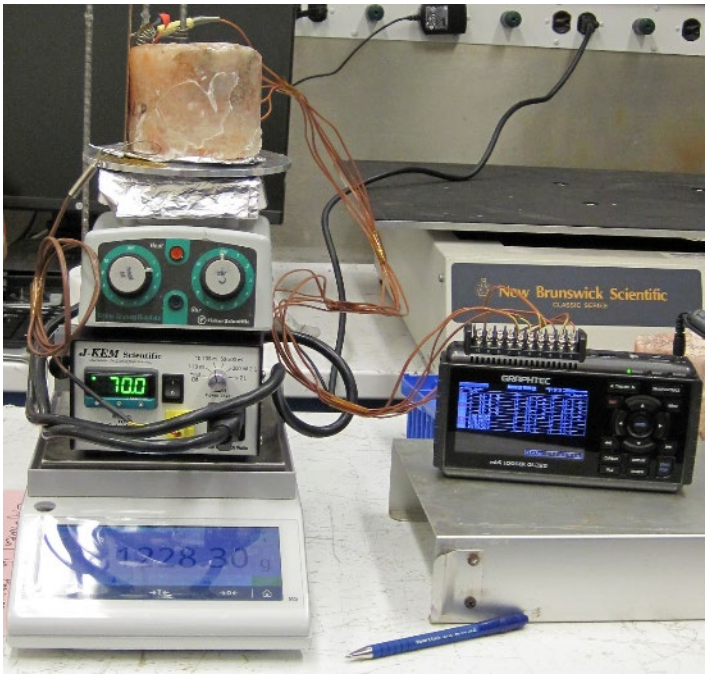

Figure 2-8. Experimental setup showing the heating unit, temperature controller, scale, and core together with the data logger.

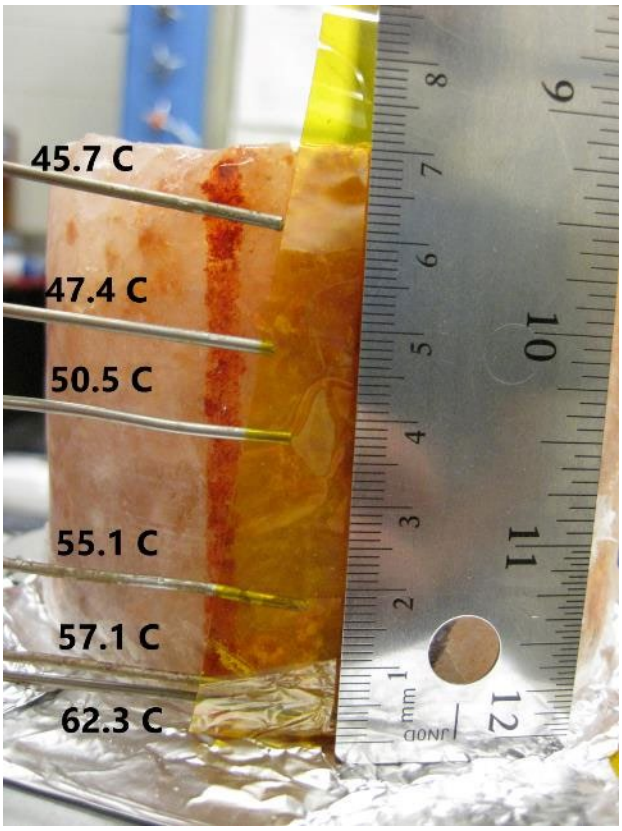

Figure 2-9. Salt core with connected thermocouples and temperature readings on 8/6/20.

The temperatures along the salt core stabilized within hours. The temperature of the hot plate was set at 70 °C and the temperature at the surface of the salt stabilized at 62.3 °C. The immediate drop of temperature is consistent with the results obtained by our team and others and is due to the low coupling between the heating surface and salt. This issues was also observed in field testing during the shakedown test and was remediated by switching to infrared heaters. The experiment was run from 07-7-2020 to 08-6-2020. The initial salt core weight was recorded at 1196 g prior to the heating experiment. At the completion of the experiment the mass was 1187 g. This represents the loss of 9 g of water or 0.7 wt. /%.

The Magritek NMR Mouse instrument was used to measure the relaxation time T_2 of free WIPP brine, water inclusions isolated in single halite crystals, and salt aggregates from ROM salt rich in accessory minerals. These samples were selected as they represent brine population present within salt with varying degrees of occluded water. The measurements were used to optimize the detection scheme for the salt core and characterize the relaxation times of the different brines. The Magritek NMR Mouse instrument shown in Figure 10 is a single-sided NMR designed for rapid relaxation measurements of materials with an added stage for profiling through samples. The B_1 magnetic field was measured to be 13.41 MHz and the $\pi/2$ pulse length was 6 μs at -7 dB power attenuation. For the CPMG experiment to measure the T_2^{eff}, 400 echoes with a 200 μs echo time were acquired. The data set is the accumulation of 20000 acquisitions with a T_1 delay of 800 ms (greater than $5*T_1$).

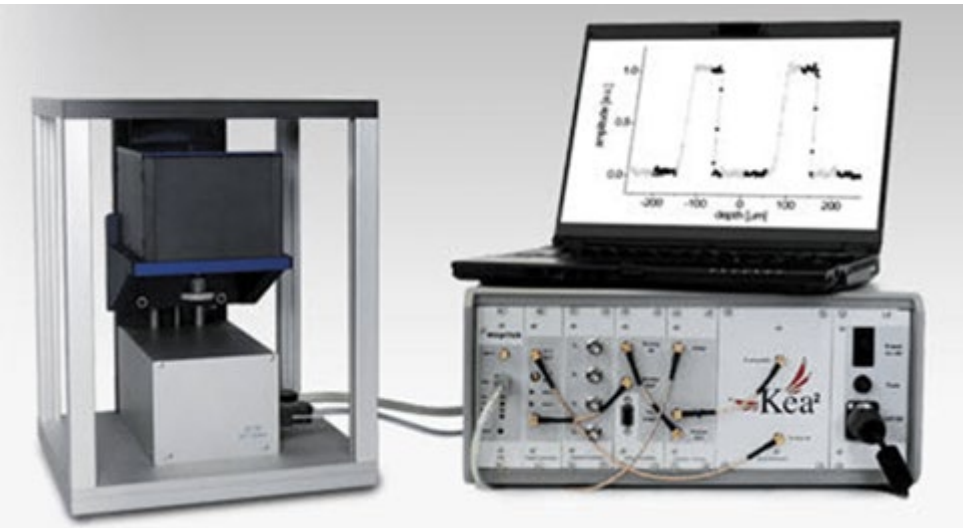

Figure 2-10. Magritek NMR Mouse pictured with KEA spectrometer.

2.4.2 Results Low field NM examination of water distribution in salt: characterization before and after heating.

The raw data acquired from the Magritek NMR Mouse for the measurements of the salt core taken on the cold and hot sides of the material before and after it was heated are shown in Figure 11. The left most image is the full set of 400 echoes acquired using the CPMG experimental parameter set with the middle image reporting just the echo intensity. From the exponential decay of the echo heights, the T_2^{eff} can be determined by fitting the data to a single or multiple exponential decay. T_2^{eff} refers to the fact that there is an additional component of the T_2 relaxation caused by field inhomogeneity that cannot be excluded from the technique. The T_2^{eff} that is calculated is the sum of the T_2 and the field inhomogeneities. The left data is the Laplace Inverse transform of the middle results giving a model independent summary of the number of relaxation modes as well as a distribution from the width of each peak.

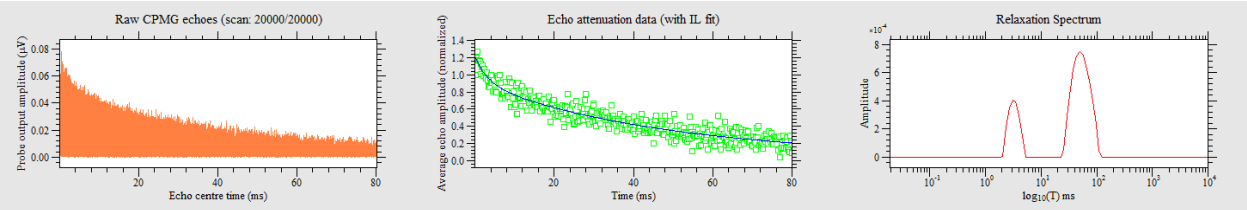

Cold Side – before heating

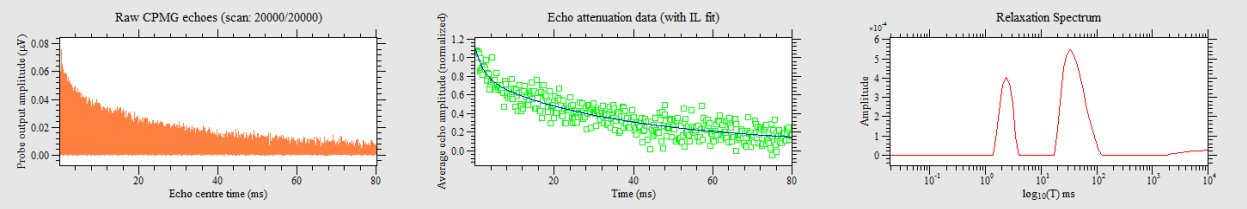

Cold Side – after heating

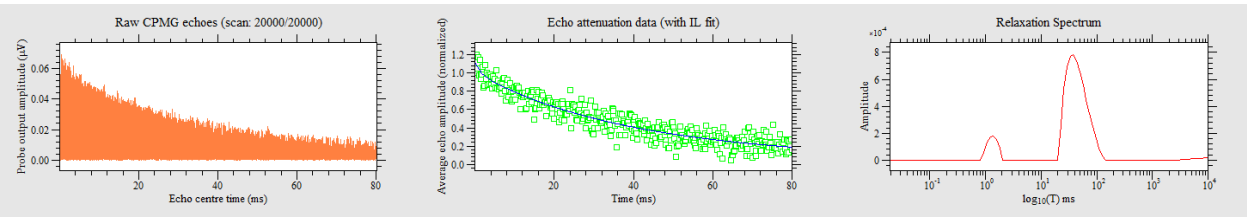

Hot Side – before heating

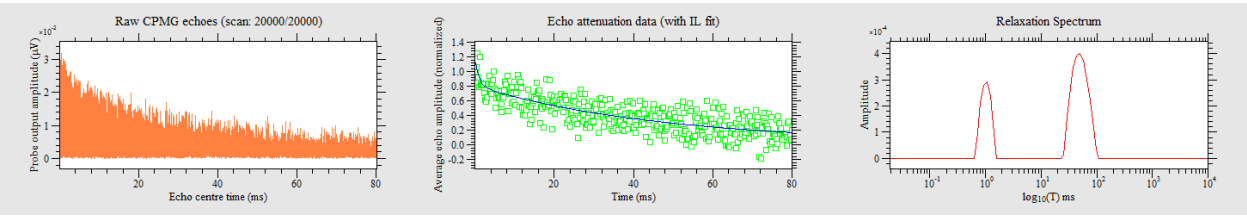

Hot Side – after heating

Figure 2-11. T_2 measurements and Laplace Inverse Transform results. Raw data acquired from the Magritek NMR Mouse for the measurements of the salt core. The left panel shows the full set of 400 echoes acquired using the CPMG experimental parameter set with the middle image reporting just the echo intensity and the right panel showing the Laplace Inverse Transform results of the signal showing the different water populations (different peaks and their relative abundances "amplitude of the peak"). Hot side refers to the side of the core that was in direct contact with the hot plate and the cold side refers to the top of the core.

The Laplace Inverse Transform results show that the salt core has two different water phases. The peak with the shorter relaxation time represents the tightly bound water or water in small pores (ca. 1 to 5 msec) and the peak with the larger relaxation signal (45 to 54 msec) representing the occluded brine inclusions. We also note that the relative ratio of the two peaks in the top part of the salt core is different from the ratio of peaks at the bottom. This is indicative heterogeneous water distribution in the salt core. Characterization of the hot and cold sides of the salt core before heating shows that the side of the core that would be heated started with relatively more brine inclusions (longer T2) than the side that remained colder. After heating the relative amount of brine inclusions (longer T2) on the heated side decreased (drop in signal intensity) as will be shown in the calculations to follow. We also see that the bound water had a shortening of the T_2 possibly indicative of a tightening of the pore structure to smaller dimensions or partial dehydration of the minerals.

After the NMR investigations had been completed for each material the echo data was analyzed and fit to a bi-exponential decay. To quantitatively determine the T_2^{eff}, the CPMG echo data (middle plot, green) was fit to a decaying exponential equation with two terms based on the results from the Inverse Laplace results. The form of the equation is

$$y = y_0 + A_1 e^{-x/t_1} + A_2 e^{-x/t_2}$$

with t_1 and t_2 as the T_2^{eff} for the bound and free water phases and A_1 and A_2 are the amplitude of the signal. The fitting routine was a bit unstable due to the low signal-to-noise but difficulties would be avoided by reducing the degrees of freedom. The results from the Laplace Inverse transform assisted in putting bounds on t_1 and t_2 in the fitting routine and y_o was also fixed at 0. As mentioned previously, the results for A_1 and A_2 will show the relative amounts of both phases. The values presented here are arbitrary units; however, they have not been normalized so the reported numbers are semi-quantitative between measurements and sampling regions.

Shown in Figures 2-12 and 2-13 are bar graphs summarizing the results from fitting the echo data to the bi-exponential function. Error bars are included showing +/- one standard deviation from the fits. The T_2 relaxation parameters show little significant difference from the hot and cold sides, before and after heating. It can be concluded that the dimensionality and chemistry of the droplets and pore space have not changed with heating. This hypothesis will be studied with more extensive future measurements.

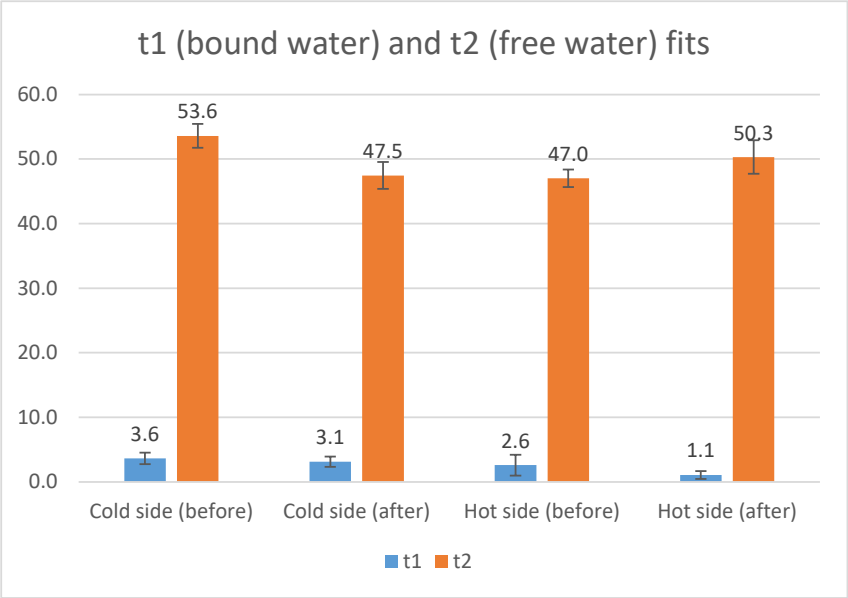

Figure 2-12. Bar graph showing a summary of the relaxation times T_2 and T_2 of the free water (associated to minerals or in tight pores) and water in inclusions. The data represent the top and bottom of the salt core before and after heating.

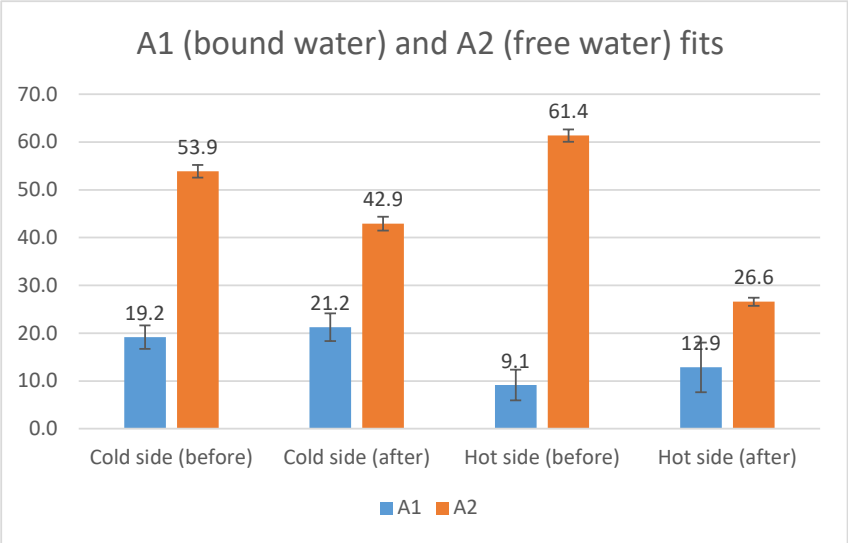

Figure 2-13. Bar graph showing a summary of intensity of the signals attributed to the bound and free water. The data represent to top and bottom of the salt core before and after heating.

The changes in A_1 and A_2 are more telling of differences before and after heating. Plotted in the bar graphs are the $A_{1,2}$ values representing the relative amounts of bound (A_1, blue) and free water (A_2, orange). Again error bars are included showing +/- one standard deviation from the fitting routine. The cold side was very similar between before and after heating, perhaps a small reduction in the free water (A_2) indicative of some water transport towards the heated zone. The hot side showed very different behavior as expected. There is a clear reduction in the amount of free water occlusions, reducing from 61 to 27. In effect and the conclusion from these studies, the heated side showed the loss of water inclusions and this could be measured using the NMR mouse and T_2 experiments.

A calibration of the signal amplitude with exactly weighed water content is needed to normalize the signals recorded. The data reported here remains qualitative but shows great promises and clearly indicates that under the temperature gradient established in our experiment brine migration from water inclusions and free water occluded in salt represents the major component of the water that is mobilized during the heating experiment.

2.5 Conclusions and Future work

BATS brines were found to have consistent K/Mg ratios while showing a relatively large variation in Na/Cl ratios. The data are consistent with brines analyses performed on WIPP brines. However, there appears to be some inconsistencies in the analytical data. Some samples have quite large charge imbalances and inconsistent sodium concentrations. This is likely due to analytical errors from the dilutions of concentrated brines and instrument calibration. Careful re-

evaluation of the samples is needed to gain confidence in the data and support the conclusion derived from our analyses. We are planning to perform a re-run of the archived samples from BATS and use calibration standards to check the validity of the analytical method. In addition, we will work with the Carlsbad team to develop a protocol and procure equipment to perform pH and alkalinity measurements *in-situ* whenever possible. Accurate values for pH and alkalinity will be crucial to perform thermodynamic modeling of the brine chemistries. We will analyze any available samples from the BATS experiments using the new protocols that will be established that continue to support the BATS field experiments through the analysis of brine samples.

Our thermodynamic calculations of the saturation indices of the brines collected from the BATS experiment have identified several mineral phases that are likely to precipitate out of solution. Some of these mineral phases are unlikely to influence the chemistry of the brines collected from the BATS experiment. However, thermodynamic modeling identified several major mineral phases that are likely to play a key role in defining the chemistry of the brines. To support the modeling effort and provide experimental data for model validation, we will perform mineral characterization using X-ray diffraction of the mineral precipitates that are associated with the BATS brines. The analyses should identify the major mineral phases that are in equilibrium with the brines and provide information for model validation. We will perform the analyses on the BATS brine sample collected immediately after the development of the test boreholes as well as on the samples collected after the initial heating experiment and any future brines sampled in support of the BATS field test.

Thermodynamic calculation using PHREEQC will be performed to gain an understanding of the mineral phases that control the chemistry of the brines from the BATS experiment. The current model calculations will be updated with representative pH and alkalinity measurements for the BATS brines and will use results from the X-ray diffraction to define the mineral phases that are likely to control the brine chemistry and composition. After establishing a satisfactory model at ambient temperature, we will set up a series of batch calculations to predict the evolution of the mineral saturations with temperature. The calculations will be constrained by the experimental characterization of the mineral precipitates associated with the BATS brines. The thermodynamic calculation of the brine chemistry and identification of the mineral phases controlling the brine chemistry will be summarized for publication in chemical geology.

Preliminary data from low field NMR characterization of the relaxation times of water present in a salt core from WIPP was very informative. The data showed that brine associated with WIPP salt can be separated into two groups. The first group of water is strongly immobile and can be attributed to water bound to minerals or water present in tight pores. The second group of water is present as free water and is assigned to brine inclusions. The relative intensities of the signal attributed to each group indicate that the water associated with fluid inclusions was more abundant and more readily mobilized by temperature gradients. We will perform a series of signal calibration experiments to standardizes the NMR signal so that quantitative data can be derived from the signal. The following calibrations will be performed:

- Signal intensity as a function of brine mass
- Influence of brine composition on relaxation times
- Relaxation times of water associated with various minerals found in WIPP salt.

The NMR data will be compared to the water mapping obtained using CT scans. The two techniques can provide complementary information that can be used to gain a precise understanding of brine mobilization under temperature gradients. The NMR data will be combined with CT for a publication.

3. Isotopic Analysis

3.1 Water Isotopic Composition

In this section we discuss implementation of continuous measurement of H_2O concentration and stable isotopic content (^{18}O and deuterium- deuterium is also noted as ^{2}H and D in this report and in supporting reproduced figures) during the initial heating experiment (January-February, 2020), unheated permeability testing (April-August, 2020), and initial laboratory efforts to measure the stable isotopic content of individual fluid inclusion as well as H_2O in matrix clays.

The rationale for employing isotopic analysis lies in the knowledge that heating of salt drives the movement of brine inclusions and that in addition to fluid inclusions in salt matrix, salt layers also include water in forms other than liquid, i.e., as interstitial waters that may migrate through fracture systems and as bound water in hydrous minerals (e.g. clays, gypsum, polyhalite), all of which may contain variation in their isotopic content.

Previous analyses of fluid inclusion H_2O from WIPP show that ^{18}O and deuterium in these waters is isotopically intermediate relative to the nearby ERDA9 drill hole (E9 samples in Figure 3-1) and local meteoric waters (parallel lines left half of Figure 3-1) (Lappin, 1988). Knauth and Beeunas (1986) interpret WIPP inclusions with the more positive values to coincide with the isotopic composition expected for evaporating sea water (in the environment the salt was crystalized) which follows a hooked trajectory on a $\delta^2H/\delta^{18}O$ diagram; and inclusions with more negative values to probably reflect synsedimentary or diagenetic mixing of meteoric water with evaporite brines.

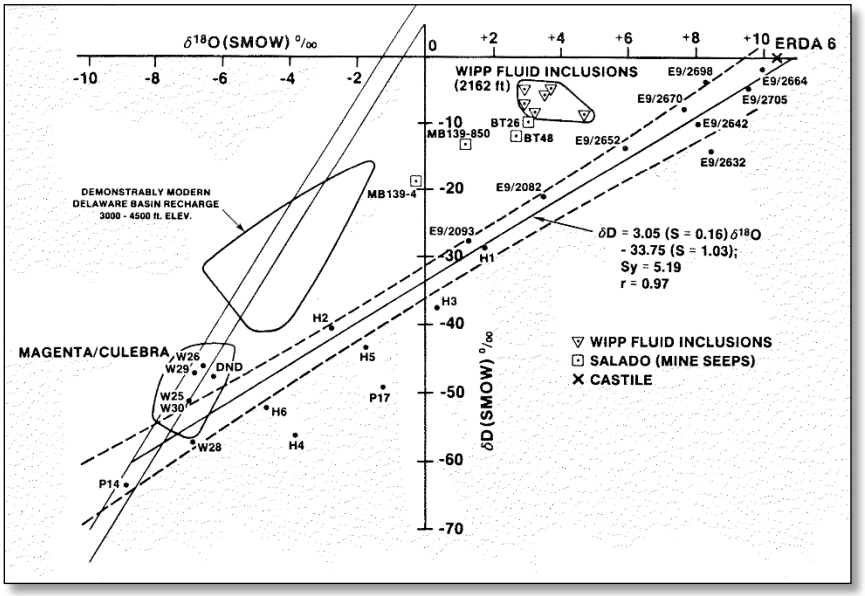

Figure 3-1. Stable water isotope data from WIPP site characterization studies (from Lappin, 1988)

3.1.1 Water Isotopic Composition Time Series: Phase 1

To determine the effect of heating on movement of H_2O in salt, we have been monitoring the concentration of H_2O as well as the isotopic content (^{18}O relative to ^{16}O ($\delta^{18}O$ permil) and ^{2}H relative to ^{1}H ($\delta^{2}H$ permil)) in continuous flow of Nitrogen through the sealed heated and unheated boreholes during Phase 1 of BATS. Continuous measurement of vapor phase H_2O isotopes during borehole heating will be impacted by several effects: 1) evaporation as liquid brine flows into the borehole and evaporates completely or partially into the dry N_2 stream; 2) H_2O from dehydration of hydrous minerals, that may enter the borehole; and 3) hydrous minerals that may form in the borehole (preferentially incorporating heavier isotopes). Continuous measurements are made with a cavity ring-down spectrometer (CRDS) (Picarro, Inc., model #L2130-i) that measures the concentration of water vapor in the gas stream, as well as both oxygen and hydrogen isotopes. Hydrogen and oxygen isotopic measurements are reported as ^{2}H relative to ^{1}H (R_H) and ^{18}O relative to ^{16}O (R_O) in units of per mil and relative to Standard Mean Ocean Water (R_{STD}), i.e. $\delta_{samp} = (R_{samp}/R_{STD} - 1)*1000$. Additional instrumentation for gas stream analyses include a LI-COR 820 (CO_2/H_2O), and SRS quadrupole mass spectrometer (AMU scans 2-180 AMU). Dry nitrogen (N_2) is circulated through the open volume behind the packer and delivered to the external analyzers via the outflow stem of the packer. The mass flowrate of gas (reported at Standard Temperature and Pressure) is monitored both upstream and downstream of the packer to confirm the mass balance of N_2 flowing through the system as an indication of any leaks of the packer-isolated interval through time. Downstream of the flowmeter after the packer, there is a pressure relief valve and a pair of plumbing tees and three-way solenoid valves to allow switching the gas streams from the two boreholes between the two branches of gas analyzers instruments.

Over January and February of 2020 we performed Phase 1 heating of the heated borehole (see Chapter 1 for borehole descriptions and layout). Time series of borehole temperatures and diameter are shown in Figure 3-2. Borehole temperature, Figure 3-2 left side, is highest near the heating element (HHPTC3) at 2.22 m and grades to lower tempertures at 1.22 m and 0.61 m ((HHPTC2 and HHPTC1, respectively). Figure 3-2 (right side) also demonstrates that compression induced incremental reduction in borehole diameter that are observed in the unheated borehole (green data) are not observed in the heated borehole. This is attributed to thermal expansion of the salt essentially building a “stress cage” around the bore diameter until heater power is turned off on Feb. 18.

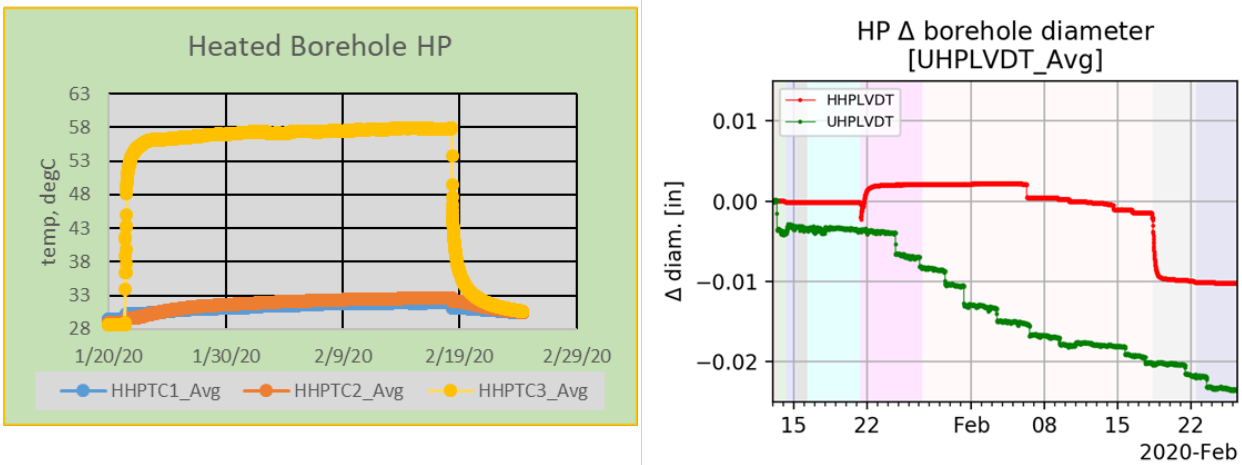

Figure 3-2. Time series of borehole temperatures (left) and diameter (right).

Timing of various changes in flow rate and heating are described in Table 3-1; H_2O concentration and isotopic data are shown in Figure 3-3. Prior to powering the heating element, baseline data for H_2O, δ^2H and $\delta^{18}O$ were collected and flow rate was adjusted to optimize instrument performance (Jan. 13 to Jan. 20). Power to the heating element was initiated on January 21 and was held constant at 120 degree C until Feb 18. Over the course of the heating period, several important observations can be made. Early variability in H_2O concentration is due mostly to changes in flow rate of the purge N_2 gas stream although the unheated hole appears to probably have had some initial standing water that evaporated over time. The initial response of the heated hole to heating on Jan 21 was an immediate increase of H_2O due to both driving off of adsorbed water from the borehole surface as well as vaporization of any liquid water that may have been near the borehole surface in the form of inclusions or interstitial H_2O. In comparison, after Jan. 21 the unheated hole continues to dry down to the point where flow rate must be reduced on Jan. 27 to ensure optimal performance of the CRDS instrument. Both holes thereafter remain relatively stable for the next three weeks until the heater power is shut off although there is some slow decline in the heated borehole H_2O accompanied by slight declines in the H and O stable isotopic signatures. This is attributed to the early pulse of available H_2O being driven off by the heater leaving less available H_2O in the heated borehole over time.

Table 3-1. Timing of various changes in flow rate and borehole heating which correspond with highlighted changes in Figure 3-3.

Jan-13-2020 09:38 AM	# 1: gas on (2 L/min)
Jan-14-2020 07:14 AM	# 2: gas -> 200 mL/min
Jan-15-2020 07:24 AM	# 3: gas -> 500 mL/min
Jan-16-2020 07:23 AM	# 4: gas -> 150 mL/min
Jan-21-2020 09:40 AM	# 5: heat on
Jan-27-2020 08:14 AM	# 6: gas reduced, H=50; U=25 mL/min
Feb-18-2020 08:15 AM	# 7: heat off (leak)
Feb-22-2020 12:01 PM	# 8: gas spent, leak stops

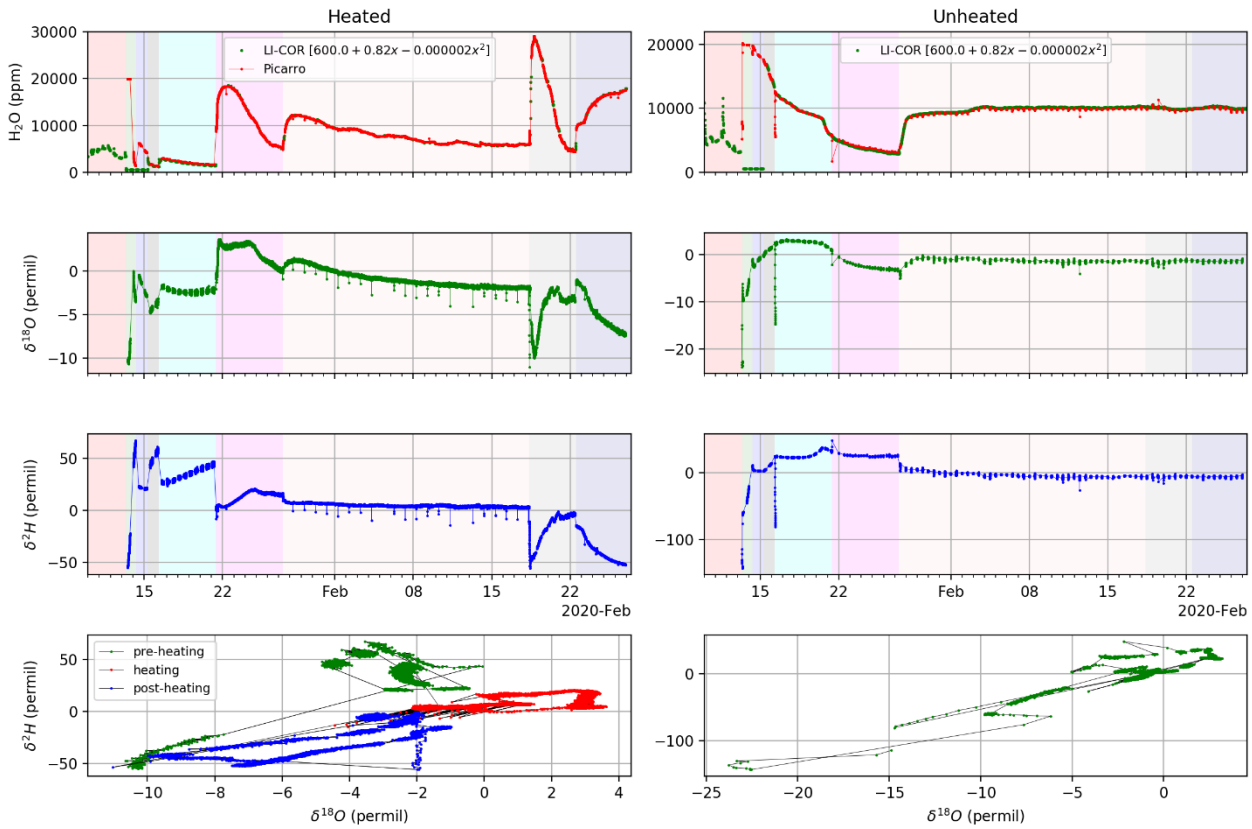

Figure 3-3. H_2O vapor concentration as well as $\delta^{18}O$ and $\delta^{2}H$ in the heated (left) and unheated (right) boreholes as a function of time. Color changes indicate heater on and off as well as changes in gas flow to optimize analytical performance.

The most striking result observed in Figure 3-3 is the sudden increase in H_2O in the heated hole almost immediately following the powering down of the heater on Feb. 18. This six-fold increase in H_2O is accompanied by a large and rapid decrease in both the ^{2}H and ^{18}O isotopic content. We hypothesize that the changes observed immediately following cessation of heating are explained by the following sequence of events. Within minutes of heater power off, borehole temperature declines rapidly (Figure 3-2, left) followed promptly by collapse of the stress cage and reduction in hole diameter (Figure 3-2, right). We hypothesize that elimination of the stress cage allows the sudden eruption of these inclusions into the borehole as demonstrated by the abrupt increase in H_2O concentration. Such inclusions have been shown by previous work to migrated towards the heat source (Roedder and Bassett, 1981). Indeed, we hypothesize further that this event was significant enough that expelled waters accumulated as liquid H_2O in the borehole as evidenced by the H and O isotopic data. As shown in Figure 3-1, $\delta\,^{2}H$ and $\delta\,^{18}O$ isotopic content in WIPP inclusions are typically ~ -5 and +3 per mil respectively. If this water was evaporated instantaneously into the borehole there would be no fractionation and the resultant isotopic measurements would remain relatively unchanged. If, however, the flux of water was rapid enough that not all could immediately evaporate (recall that temperature is dropping rapidly as well and that the H_2O capacity of the borehole air is therefore necessarily reduced), liquid water would accumulate and any vapor that would be subsequently measured would be in isotopic equilibrium with that liquid. Water vapor that is in equilibrium with standing liquid is

isotopically depleted relative to that liquid and that temperature dependent fractionation is well documented in the literature e.g. Horita and Wesolowski (1994).
Further evidence for this interpretation include data from the LI-COR CO_2/H_2O analyzer (Figure 3-4). The content of inclusions in halite (as well any other mineral inclusions) are, at least partially, a combination of the liquids and gases that were present at the time that the inclusion was sealed off from its environment (crystallization). Salt precipitation occurs at the Earth surface where carbon dioxide is one of the most abundant trace gases and CO_2 in salt fluid inclusions has been previously observed (Roedder, 1984). Simultaneous to the sharp increase in H_2O at cessation of heating, we also observed a rapid increase in CO_2 in the continuous flow stream from the borehole (Figure 3-4). Unfortunately, the sudden decrease in temperature on Feb. 18 resulted in failure of the borehole packer system seal and a concurrent abrupt change in flow rate. Both the H_2O and CO_2 resulting from the discharge of inclusion contents into the borehole was therefore greatly diluted.

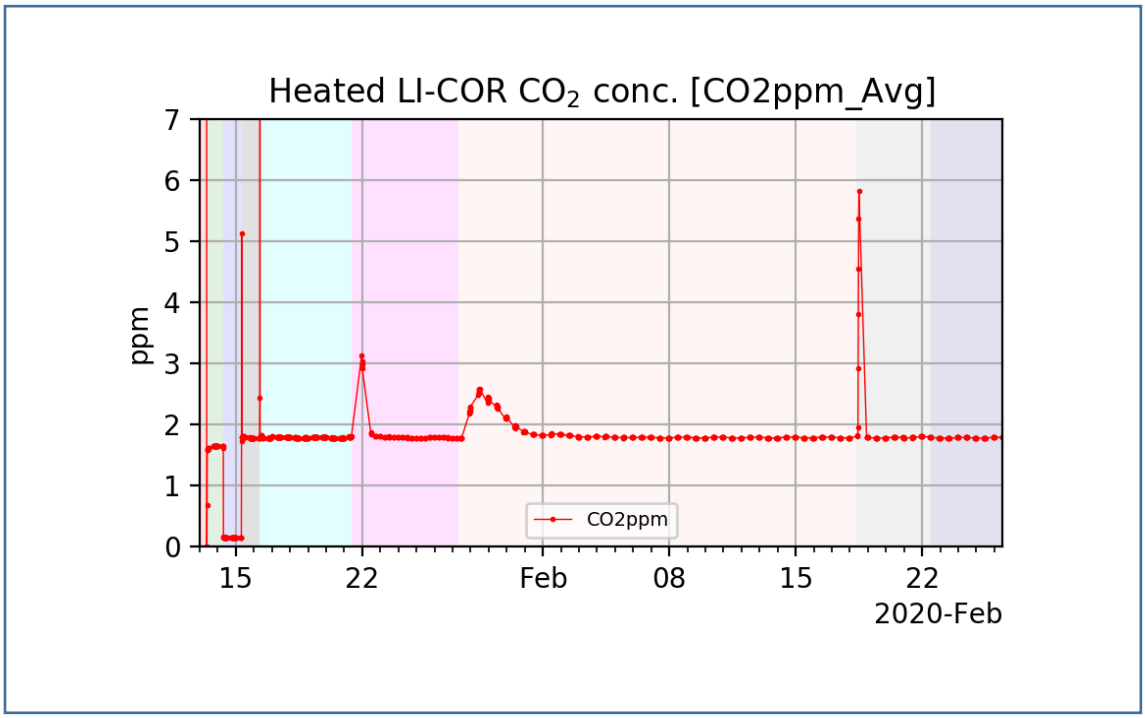

Figure 3-4. Carbon dioxide in continuous flow sample stream of the heated borehole. Unheated borehole CO_2 (not shown) was constant at ~2 ppm.

We can estimate the magnitude of this dilution with the data collected with the SRS quadrupole mass spectrometer (QMS). QMS data are shown in Figure 3-5 where data from the heated and unheated boreholes alternate in the continuous analytical data stream (shorter peaks are unheated, longer troughs are heated). Shown are data for some of the most common atmospheric species,O_2, Ar, CO_2 as well as several other tracers relevant to the salt environment. Looking closely at the data during the period immediately following cessation of heating in the bottom half of Figure 3-5 we see that both O_2 and Ar in the heated data are reduced by a factor of ~ 20 relative to days prior.

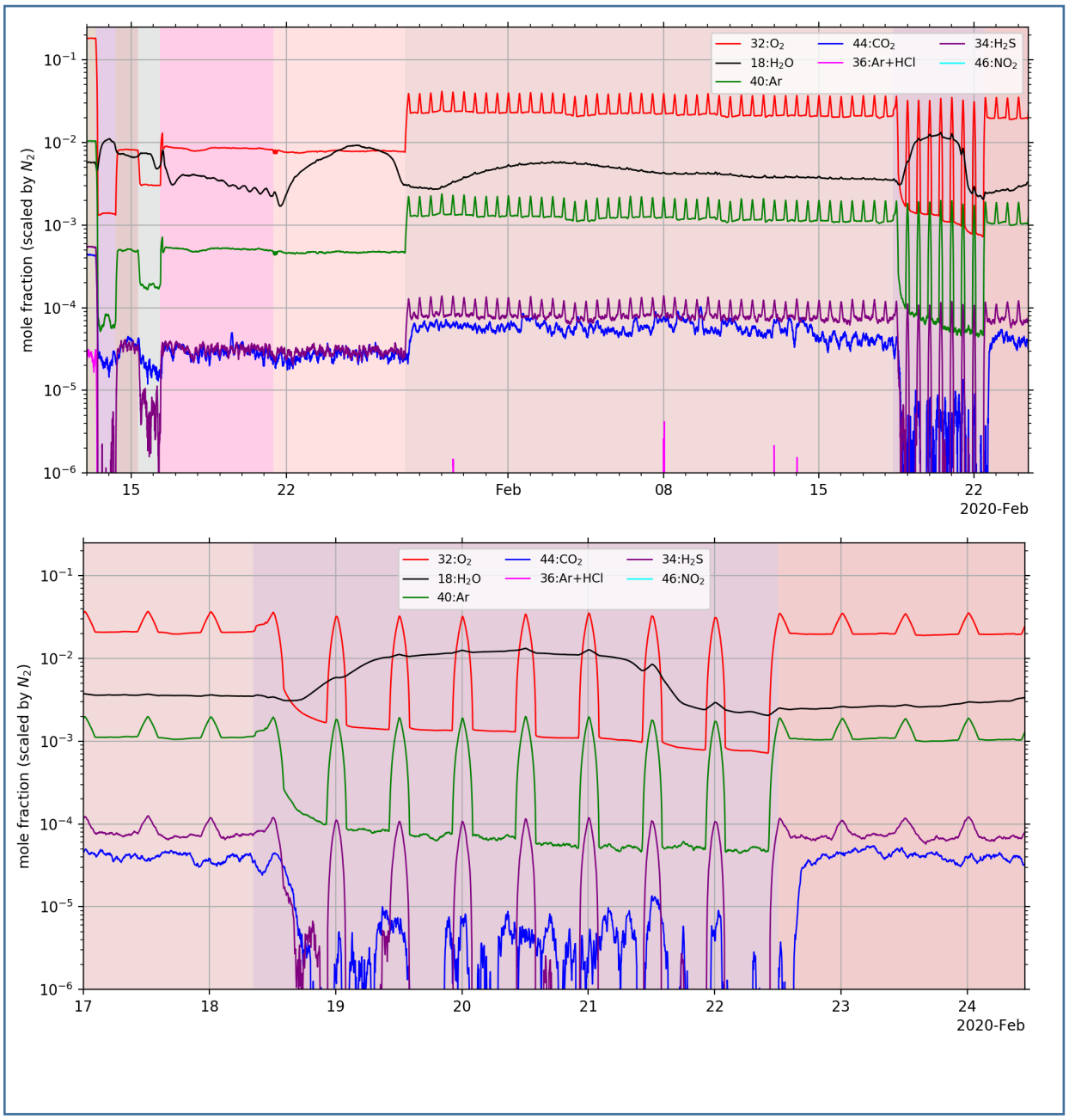

Figure 3-5. Trace gas analyses normalized to N_2. Top: Complete period of heating. Bottom: Detailed observations at time of heater turn-off.

Data collected during Phase 1 of BATS heating identify unique H_2O isotopic behavior that should help constrain and quantify H_2O phase identification (vapor vs. liquid) and also lend insight into variation of H_2O sources over time. Current efforts are being made to incorporate isotopic systematics into ongoing modeling work.

3.1.2 Water Isotopic Composition Time Series: Permeability Tests

In the spring and summer of 2020, additional H_2O and isotopic measurements were completed during testing of the heated and unheated borehole arrays for permeability. Other than a couple of short term periods, no power was applied to the heating element although flow rates were varied and pressure in the D boreholes of both the heated and unheated main holes was adjusted and monitored to determine salt permeability characteristics (see Chapter 5 for permeability test description). The sequencing of events for this period is rather complex and is itemized in Table 3-2.

Table 3-2. Sequencing of gas flow rate and hating during the permeability testing period of April to August 2020.

Date	Comment
3/3/2020	heated and unheated circulation flow ended
4/28/2020	heated flow @ 1000 mL/min
4/28/2020	unheated flow @ 1000 mL/min
4/29/2020	unheated flow @ 50 mL/min
4/30/2020	unheated flow @ 25 mL/min
4/30/2020	heater on for ~ 3.5 hrs
5/1/2020	heated flow @ 250 mL/min
5/5/2020	heated flow @ 1000 mL/min
5/7/2020	heated flow @ 250 mL/min
5/12/2020	heated flow @ 200 mL/min
5/14/2020	heated flow @ 750 mL/min
5/14/2020	heater on for ~ 6 hrs
5/15/2020	heated flow @ 200 mL/min
5/21/2020	heated flow @ 75 mL/min
6/2/2020	gas circulation off for ~ 2.75 hrs
6/2/2020	additional licor added - heated and unheated arrays have dedicated licors
6/4/2020	picarro disconnected from circulation flow for ~ 2 hrs
6/9/2020	circulation flow off for ~ 1 hr for cylinder changes
7/7/2020	unheated gas circulation off to change cylinder
7/14/2020	short term perm testing in unheated and heated HP and D boreholes
7/16/2020	short term perm testing in unheated HP and D boreholes
7/20/2020	short term perm testing in heated D borehole
7/23/2020	short term perm testing in heated D borehole
7/27/2020	heated gas circulation off to change cylinder
7/27/2020	long term perm testing in unheated D borehole @ 14.8 psi
8/4/2020	long term perm testing in unheated D borehole @ 30.6 psi
8/11/2020	short term perm testing in unheated D borehole @ 46.3 psi
8/17/2020	long term perm testing in heated D borehole @ 20.8 psi
8/24/2020	heated flow @ 75 mL/min since 5/21/2020

During this period of testing, heater power was implemented briefly for several hours on 4/30 and 5/14. Otherwise, borehole temperatures were relatively constant over the four month test period as exhibited in Figure 3-6, top panel. Bottom panel of Figure 3-6 shows detail of brief heating periods in late April through May.

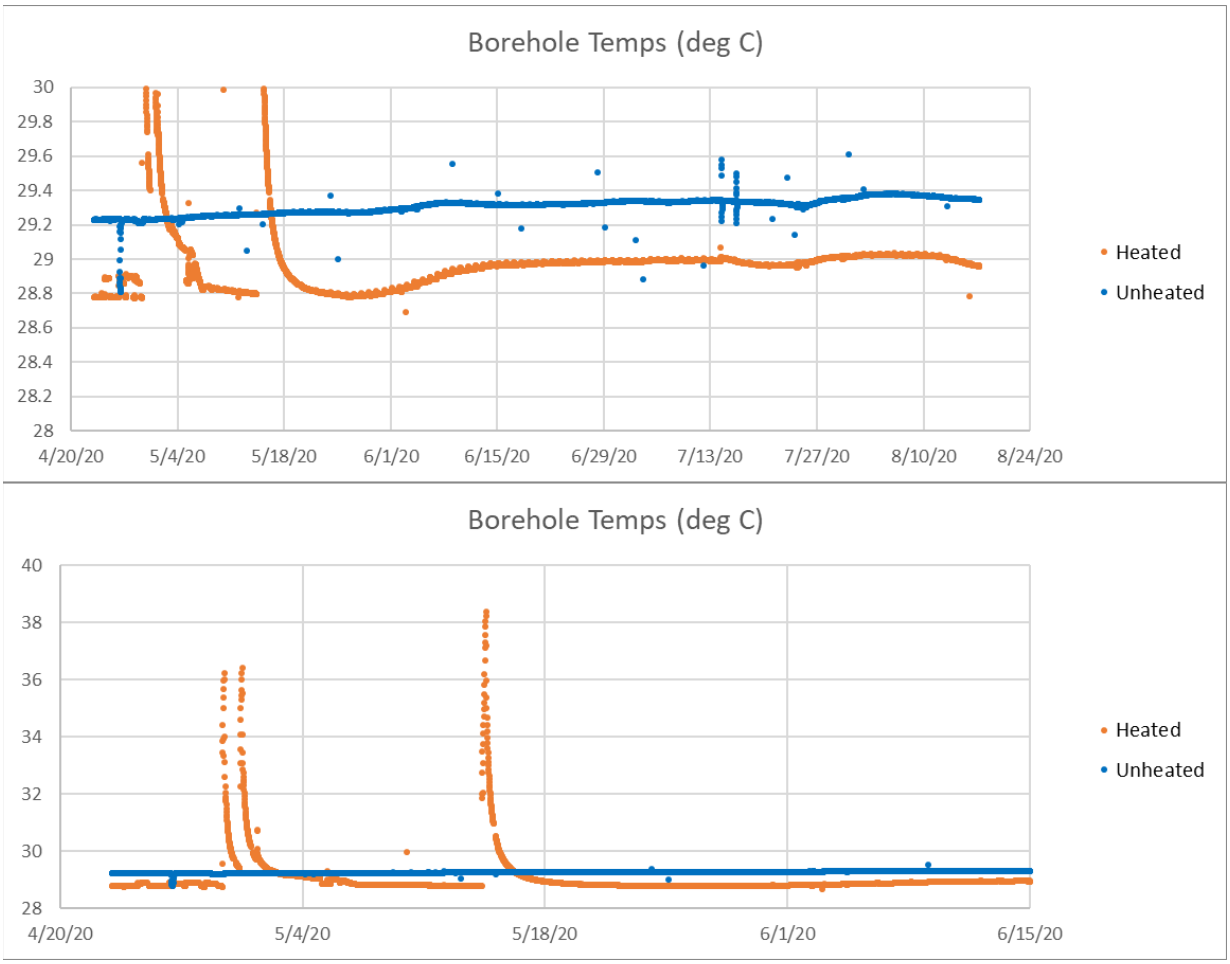

Figure 3-6. Temperature time series during permeability testing in spring/summer of 2020. Top panel shows entire time series while bottom panel shows detail of heating periods of late April through May.

Contemporaneous H_2O concentration and isotopic measurements ($\delta^{2}H$ and $\delta^{18}O$) of the sample streams from the heated and unheated boreholes are shown in Figure 3-7. As with Phase 1 experimental data (previous section), heating of the borehole, even for brief periods of several hours creates perturbations of H_2O concentration as well as its isotopic content (see highlighted ellipses in Figure 3-7). In addition, permeability testing in adjacent D-holes, ~15 cm from the main borehole wall (see Chapter 1 for borehole layout details) induces perturbations to both the H_2O concentration and its isotopic content as best exhibited in the latter part of the time series from the mid to latter part of July.

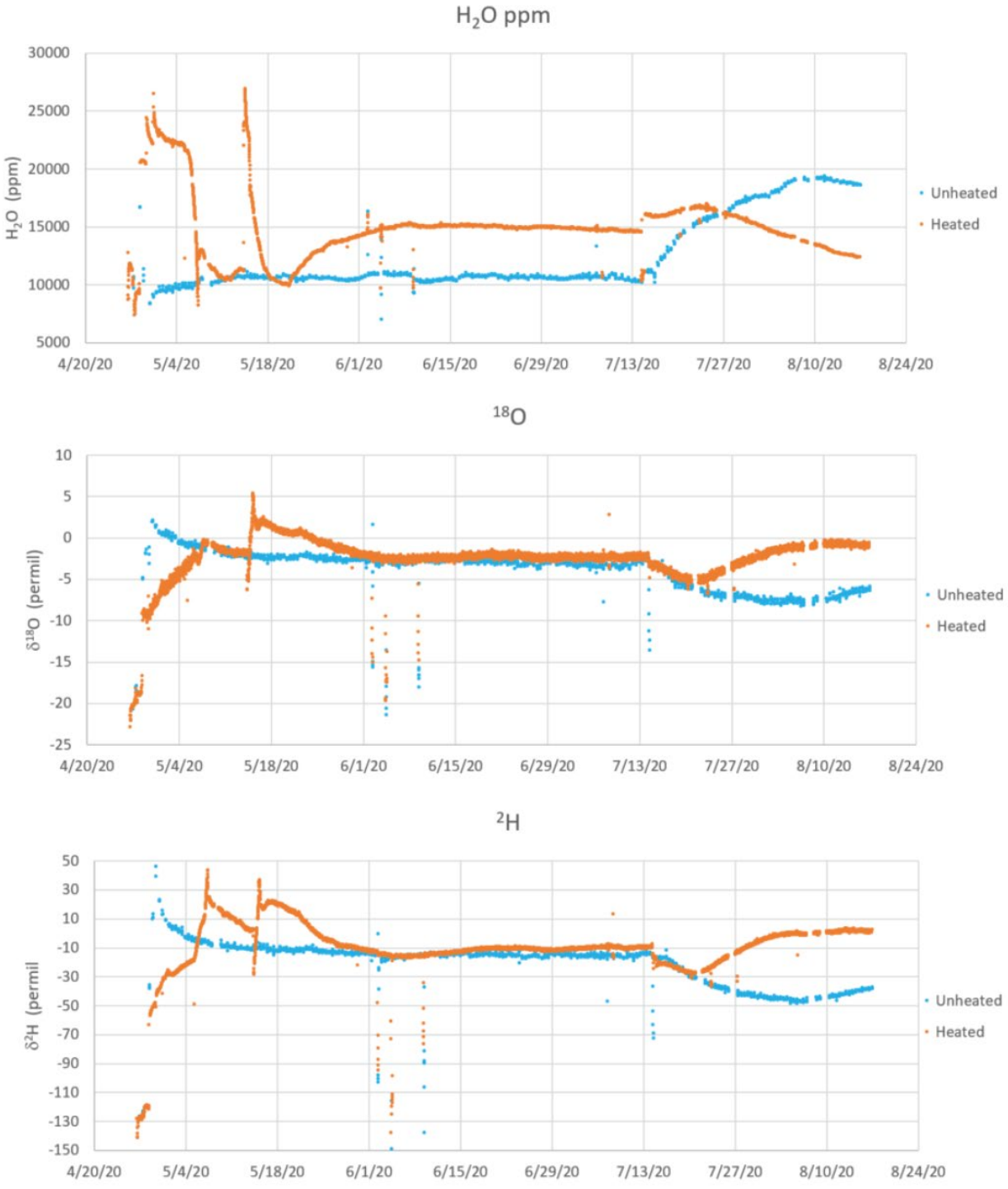

Figure 3-7. H_2O vapor concentration as well as $\delta^{18}O$ and $\delta^{2}H$ in the heated (orange) and unheated (blue) boreholes as a function of time.

Although these data are recent and have yet to be fully evaluated, we can make several observations that reflect the utility of isotopic measurements to complement basic H_2O content results. As an example, one very common method for evaluating H_2O isotopic results is to

compare δ^2H (deuterium) to $\delta^{18}O$ as in Figure 3-1. When we plot δ^2H relative to $\delta^{18}O$ for the heated and unheated boreholes during the permeability testing period, we see that regression analyses of both holes yield very similar slopes and intercepts (Figure 3-8).

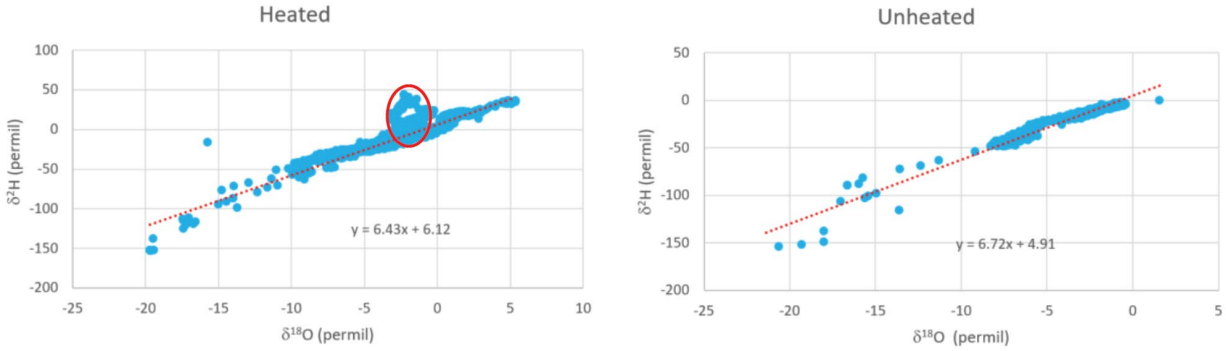

Figure 3-8. δ^2H relative to $\delta^{18}O$ for the heated (left) and unheated (right) boreholes during the permeability testing period April to August 2020.

A more focused look at the heated borehole data, however, yield subsets that can be examined more closely. Figure 3-9 highlights the outlying data encompassed within the red ellipse of Figure 3-8. These data coincide with the heating periods highlighted in the blue and red ellipses of Figure 3-7 where brief periods of heating were initiated. As seen in Figure 3-9 below, the slopes and intercepts of regressions of δ^2H relative to $\delta^{18}O$ reveal markedly different results from the overall period of analysis shown in Figure 3-8. Processes that can affect the relationship of δ^2H relative to $\delta^{18}O$ include, condensation, evaporation, mixing of H_2O sources (e.g. inclusions, interstitial H_2O, hydrous minerals), fractionation related to hydrous mineral dehydration and hydrous mineral formation, etc. Although we cannot make such determinations regarding this preliminary data, it is these processes that we hope to elucidate as we gather more data and further develop our isotopic modeling capabilities.

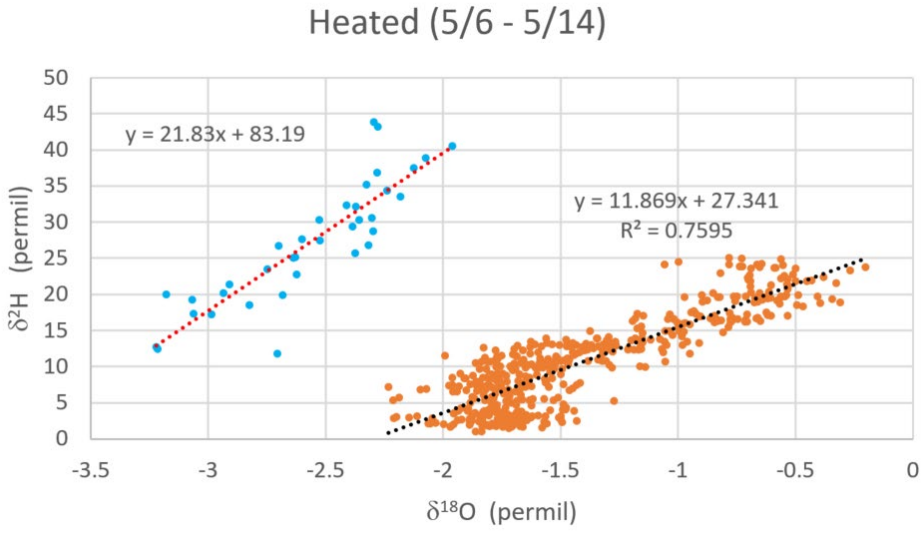

Figure 3-9. δ^2H relative to $\delta^{18}O$ for the outlying data highlighted in Figure 3-8.

3.1.3 Water Isotopic Composition of Fluid Inclusions

In order for us to completely understand the results of our continuous borehole isotopic analyses and to provide input into our source terms for isotopic modeling, we must also know the average and range of the isotopic content of the various source terms that may influence our results. These sources include fluid inclusions in salt matrix, interstitial H_2O that may migrate freely in fracture networks and H_2O that is incorporated in hydrous mineral matrices (e.g. clays, gypsum, polyhalite). We have therefore begun to develop techniques for analyses of these disparate end members. Our initial work has been to develop reliable methodology for analysis of δ^2H and $\delta^{18}O$ in WIPP salt fluid inclusions to verify the results of Knauth and Beeunas (1986) and to examine further the potential range of these limited data.

Previous efforts to reliably and reproducibly analyze the isotopic content of NaCl fluid inclusions have employed a variety of methods (Horita and Matsuo, 1986; Knauth and Beeunas, 1986) with all methods having some limitation in their application. We have initially chosen to employ a vacuum crushing technique due to its simplicity of implementation and capability of analysis of small samples. Our method utilizes a small volume vacuum crusher (modeled after Dublyansky (2012), shown on the left of Figure 3-10) purged with UHP N_2, a high vacuum extraction line with cryogen cold finger for focusing eluted H_2O and a Picarro CRDS model L2130-i (right side of Figure 3-10) for isotopic analysis (Uemura et al., 2016).

.

Figure 3-10. Crusher with inlet and injection port on the left. Picarro CRDS on the right.

In order to calibrate and reliably test the vacuum crushing system, a port for injection of sub-microliter reference H_2O is built into the crusher body. To investigate instrumental calibration and/or systematic fractionation induced by the analytical process we injected a series of known isotopic reference materials into the crusher device both with and without sample present. Figure 3-11 shows an example correlation of measured values of $\delta^{18}O$ (left) and δ^2H (right) versus accepted values of a series. Correlations derived from these regressions allow us to apply

corrections to sample analyses. These correlations are run on a regular basis to test for drift and ensure consistency. We have also run reference H_2O over fresh and crushed halite samples (not shown) with no measureable effect within the precision of the CRDS instrument precision.

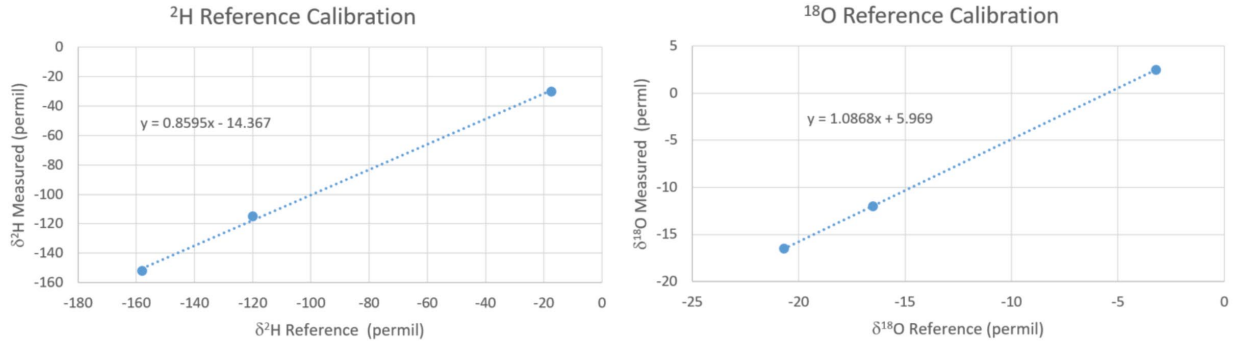

Figure 3-11. Correlation of measured reference material vs known values, O isotopes on left, H isotopes on right.

To date, we have measured three BATS samples, each approximately 0.5 grams. Measured and corrected values are shown in Table 3-3. Peak H_2O content for each sample is robust and within the analytical range required for best performance (>10,000 ppm, <40,000 ppm). Corrected results however are significantly depleted relative to reported values of other WIPP samples (Knauth and Beeunas, 1986; Lambert, 1992).

Table 3-3. Measured and corrected values for H and O isotopes of 500 mg crushed BATS salt samples.

H2O	18O		2H	
peak ppm	measured	corrected	measured	corrected
14700	0	-5.5	-80	-76
21000	-6	-11.0	-105	-105
25000	-5	-10.1	-85	-82

As noted in Knauth and Beeunas (1986) and Horita and Matsuo (1986), isotopic analysis of halite inclusions via the crush method may be susceptible to fractionation induced by precipitation of hydrous minerals before the sample can be introduced to the analytical system. Heating of the sample apparatus has been recommended to reduce mineral formation and maintain H_2O in the vapor phase. Other methods for inclusion analysis are also recommended including, sampling of individual inclusions via capillary extraction or volatilization of complete sample via flash heating with a torch. Possession of a reference material with well-defined isotopic content would also be of great benefit to evaluate the various extraction methods and the conditions under which is preferred. Rigaudier et al. (2012) describe a method for creating hydrogen and oxygen isotope reference materials for the analysis of water inclusions in halite. Moving forward with our isotopic experiments, we will employ the method of Rigaudier to develop a source of well-defined reference materials and evaluate the accuracy and precision of the crush method we are currently employing as well as moving forward with alternative sample extractions. Additional methods will be developed to perform analysis of interbedded hydrous clays.

4. FEHM Code Development during FY20

4.1 Humidity and salt related boundary conditions: new keywords, updated existing keywords

All of the boundary conditions that are described below were incorporated in the transient boundary condition module that ids identified in the input file under the macro name **boun**. There are also other boundary condition related macros that are described below. For clarity, input macros are in bold type (e.g. **flow**) and keywords use in the **boun** macro are plain text. Though some of the keywords and input macros are not new, the functionality and efficiency when used with the air-water-heat (**ngas**) module has been improved. Some of the functionality of the new keywords overlaps that in the boundary condition part of **ngas** input. It is recommended that the user not mix boundary conditions set in the **boun** macro with those set in **ngas.** However, appropriate blank lines must be in the **ngas** input to indicate no source/sinks etc. List of humidity related boundary condition.

1. Inflow and related boundaries
    a. Specified air mass fraction of inflow stream (fxa). This keyword instructs FEHM to divide water inflow stream into pure water source and a pure air source. The fxa keyword is useful when the dissolved air in the water source is known or easily calculated as a function of temperature. The water source will be adjusted for the air mass fraction. Specified air source not allowed with fxa.
    b. Specified water source (sw, dsw). Water source adjusted as described above.
    c. Specified air source (sa, dsa). A potential numerical conflict can arise when a specified air source (inflow) is used with a specified water pressure. If the air source is large enough, the specified water pressure boundary condition can produce unpredictable results. Coding was added to turn off the fixed water pressure at this point.
    d. Specified water pressure (pw)
    e. Specified air pressure (pa)
    f. Energy boundary conditions
        i. Fixed temperature(t)
        ii. Fixed enthalpy rate (se,dse)
        iii. Flowing temperature (ft) (Note: Flowing temperature is not recommended for relative humidity or salt) as the flowing temperature is based on the enthalpy – temperature relationship of liquid water. This functionality is being updated to include the gas phase enthalpy relationship with temperature. See humidity boundary conditions descriptions below.
2. Outflow boundaries- some boun keywords can be used for inflow or outflow
    a. Specified water pressure(pw)

b. Specified air pressure(pa)
c. Specified water source (Note: while it is possible to extract fluid at a fixed or changing flow, the extraction rate must be less than a threshold which is dependent on reservoir properties and geometry.
d. Specified air source -see note for water source.

3. Humidity Boundary condition
   a. Specified flowing relative humidity (huf). This condition creates a gas inflow with a specified humidity; includes the enthalpy flow. The gas flow (sa, dsa) must be specified separately. Optional input temperature (th) and pressure (ph) for humidity calculations are also available. The temperature and pressure are new **boun** keywords. If either th and/or ph are not identified in the input, then the missing parameter is assigned reference values: (T_{ref}, P_{ref}) = (20 C, 0.1 Mpa). This boundary condition will produce water inflow via the water vapor in the gas phase.
   b. Specified humidity (hu). This condition creates both water vapor flow and dry air flow to maintain a specified humidity in a gridblock. The water and air flow can be either inflow or outflow. The magnitude of the flow depend on temperature (th) and pressure(ph) described above.
4. Useful boun keywords and macros when simulating experiments
   a. The **stea** macro is not part of the **boun** macro input but is described here because has been updated to obtain quicker steady state solutions. This can be useful when simulating a new experimental block or field site. See the **boun** keyword tran below.
   b. The tran keyword is used to start transient simulations after a steady state has been achieved with the **stea** macro. It can be in conjunction with any of the **boun** keywords described above.
   c. The chmo keyword is used to change **boun** models in time. For instance, a specified humidity condition can be imposed on a gridblock initially and later in the simulation that condition could be changed to specified water and air flow rate.

Table 4-1 List of **boun** keywords indicating related keywords and input macros. FEHM input macros in **bold**; **boun** keywords in plain text.

	Description	Status	Note	Related keywords and macros
boun keyword				
fxa	Air mass fraction in water inflow	N	Cannot use both fxa and sa in same **boun** model	sw (inflow only)
sw, dsw	Source water, distributed source	U		fxa**, flow** , huf, hu
sa, dsa	Source air, distributed source	U	See cautions in sa description above	fxa**, flow** , huf, hu

pw	Specified water pressure	U		**flow**
pa	Specified air pressure	U		**flow**
t	Specified temperature	O		**hflx**
ft	Flowing temperature	U	Not recommended for relative humidity applications use huf	hu, huf, **flow**
se, dse	Source enthalpy, distributed source			hu, huf , **hflx**, **flow**
hu	Specified humidity	N		huf , **hflx**, **flow**
huf	Specified flowing humidity	N	Cannot be used with fxa	hu, **flow**, **hflx**

N = new keyword, U = updated implementation algorithm in FEHM, O = old

4.2 Examples of boun models

Note: These air-water-heat models are available through the **boun** macro. For now, flowrate or constant pressure BCs should not be entered through the **ngas** macro until all the consistency issues are resolved. inflow:

1. (SW, SA) specified water flowrate (kg/s), specified air flowrate (kg/s). Works for a range of values. Did not test for airflow flowrate in a different direction than water flowrate. Assumes pure water and pure (dry) air flowrates. Note: *When SW is used without FXA, as in this example, the water source is assumed to be pure water*.

```
model  1          INFLOW
ti
2
0. 1.e20
sw
 -0.99e-3 -0.99e-3
sa
 -1.e-3 -1.e-3
t
 110. 110.
if
 5. 5.
```

2. (SW, FXA) specified water flowrate (kg/s), specified air fraction. Assumes water flowrate may contain air. Note: *When SW is used with FXA, as in this example, the water source is assumed to be a mixture of water and air*.

```
model  2          INFLOW
ti
```

```
2
0. 1.e20
sw
 -1.e-4 -1.e-4
fxa
  0.9 0.9
t
300. 300.
if
 5. 5.
```

3. (PW, SA) total pressure (Mpa), specified air flowrate (kg/s). Works for a range of values. Assumes pure water (if induced) and pure (dry) air flowrates. Note, if the specified air flowrate is large enough, the total pressure can exceed the specified value PW. In this case, the PW BC in will be turned off leave the pressure to be a function of the specified air flowrate. *Note: pure water only source because FXA is not used and air flow has its own source.*

```
Model  3                INFLOW
 ti
2
 0. 1.e20
pw
 0.101 0.101
sa
  -1.e-6 -1.e-6
t
 110. 110.
if
   5  5
```

4. (PW,FXA) total pressure (Mpa), specified air fraction. Works for a range of values. Assumes mixed water (if induced) and a fraction of which is air flow. *When PW is used with FXA, as in this example, the water source, induced by PW, is assumed to be a mixture of water and air*.

```
model  4                 INFLOW
 ti
2
 0. 1.e20
pw
 0.101 0.101
fxa
 0.01 0.01
t
 110. 110.
if
```

```
5     5
```

5. (SA, HUF) specified air source (kg/sec), specified flowing humidity. Here the air source is considered humidified and the air flowrate divided into a water flowrate and air flowrate. If either of ph or th is missing then the reference value is used for that parameter.

```
model  6                INFLOW
 ti
2
 0. 1.e20
sa
-1.e-3 -1.e-3
huf
0.01 0.01
 ph
 0.098 0.098
 th
 90. 90.
t
 110. 110.
if
 5     5
```

6. (PA, HUF) specified air pressure (Mpa), specified flowing humidity. Here the air flowrate results from a specified air pressure and is considered humidified. The air flowrate is divided into a water flowrate and air flowrate. If either or both keyword ph or th is missing then the reference value(s) is (are) used for that parameter. Standard conditions are Pstd = 0.1 Mpa, Tstd = 20. C

```
model  7                INFLOW
ti
 2
 0. 1.e20
pa
0.11  0.11
huf
0.01 0.01
 ph
 0.098 0.098
 th
 90. 90.
t
 110. 110.
if
 5     5
```

7. (HU) specified constant humidity. Here the air flowrate and water flow rate result from conditions necessary to maintain a fixed humidity. If either or both keyword ph or th is missing then the reference value(s) is (are) used for that parameter.

```
model  7              OUTFLOW
ti
 2
 0. 1.e20
hu
0.3 0.3
 ph
 0.098 0.098
 Th
 60. 60.
```

4.3 Simulation examples using boun models

Figure 4-1 depicts the problem domain for the an example of the boundary conditions shown above

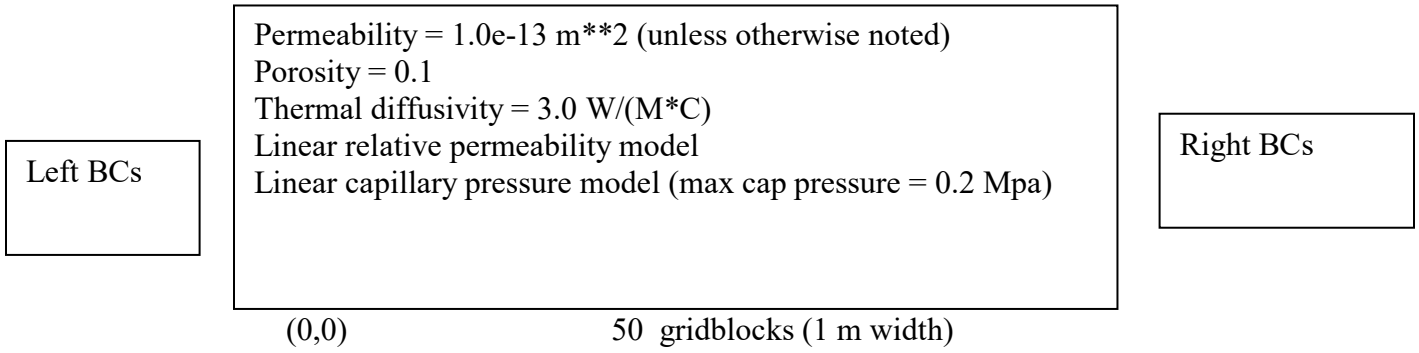

Figure 4-1. 1D domain used for example simulations with boun macro keywords and tabular air EOS verification.

The results of the simulation are presented below at 500 days. The boundary conditions are such that there is only the gas phase and steady state conditions. The fixed relative humid condition on the right side fixes the pressure (0.098 Mpa), temperature (60 C), and humidity (0.3). The pressure is predictable. The temperature shows an inflection point which indicates some complicated processes in the energy and air balance equations which are not easy to understand. The humidity shows a maximum near fixed gridblock humidity. Again, the result is difficult to explain. Increasing the reference temperature to 120 C produces a more easily explainable result.

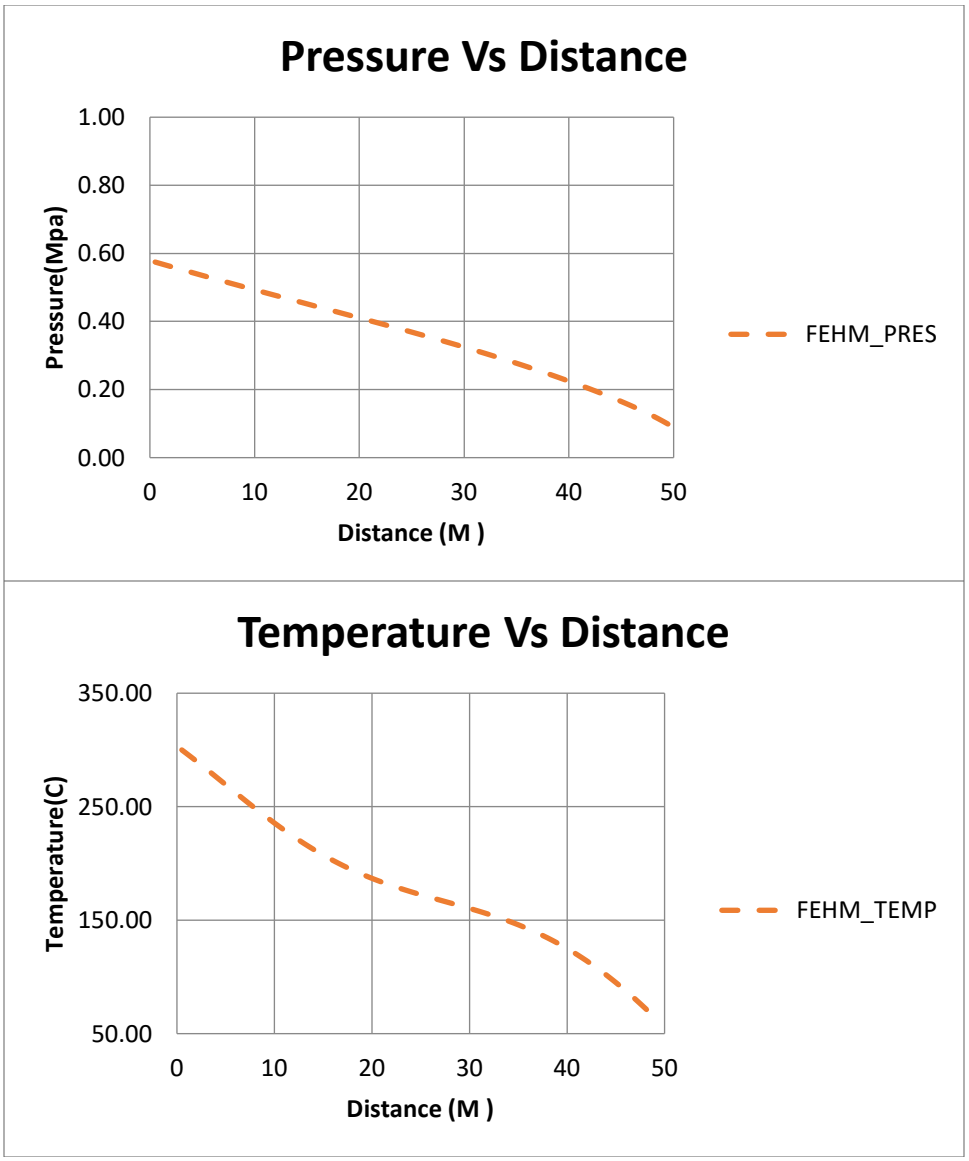
Pressure Vs Distance
1.00
0.80
0.60
0.40
0.20
0.00
Pressure(Mpa)
0
10
20
30
40
50
Distance (M)
FEHM_PRES
Temperature Vs Distance
350.00
250.00
150.00
50.00
Temperature(C)
0
10
20
30
40
50
Distance (M)
FEHM_TEMP

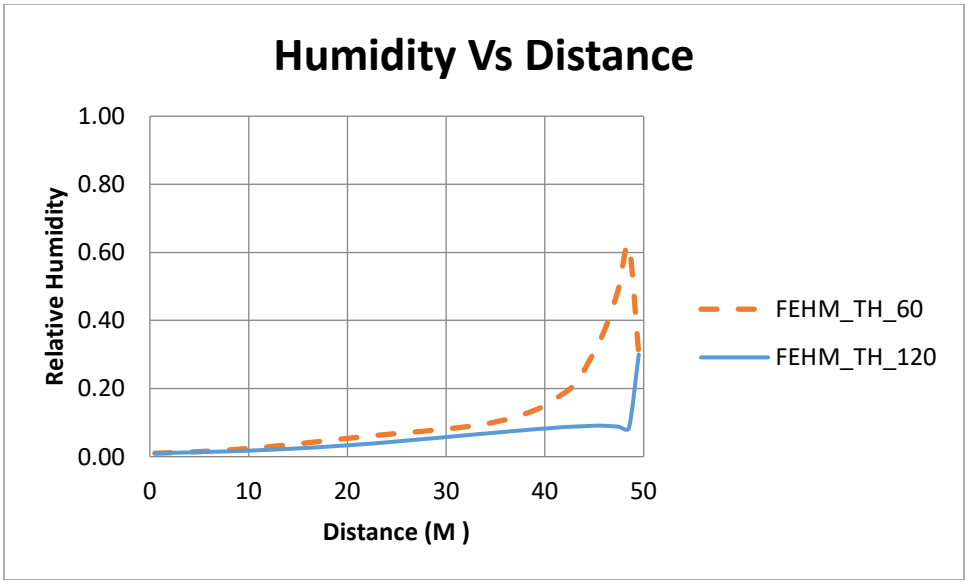

Figure 4-2. Pressures (2a), temperatures (2b), and relative humidity (2c), for model 3 applied for the Left BC and model 7 applied for the Right BC.

4.4 Tabular Air Equation of State for all temperatures

Because of the importance of the dissolved and free air in a salt repository, a highly accurate tabular Equation of State was added to FEHM. Because the Critical temperature of air is -140 C, only the gas phase is required. We note the Critical pressure of air is 3.79 Mpa but poses no problem with the inclusion of pressures up to 100 Mpa as even of the entries in the table are in the Critical region. This is because of the continuity of properties across the gas phase and critical phase boundary. The NIST23 database (Lemmon et al., 2013)for air density, enthalpy, and viscosity is used. The table structure is general enough to add other properties like (improved) solubility and heat of solutiondata as it comes available. At the heart of the high temperature fluid property module is an efficient variable resolution property table (Doherty, 2006) that was originally developed under the Carbon Sequestration Program for CO2 property evaluation.

Compared to the FEHM original formulas for density (perfect gas law), enthalpy, and viscosity, the new tabular equation of state did not produce significant differences except for density at high pressures. This is due to the deviation of density from the perfect gas law. Figure 3 show a pressure and using the problem domain described above except with smaller permeability values to produce higher pressures. For this simulation, temperatures differences between the new and EOS, were less than 1 C.

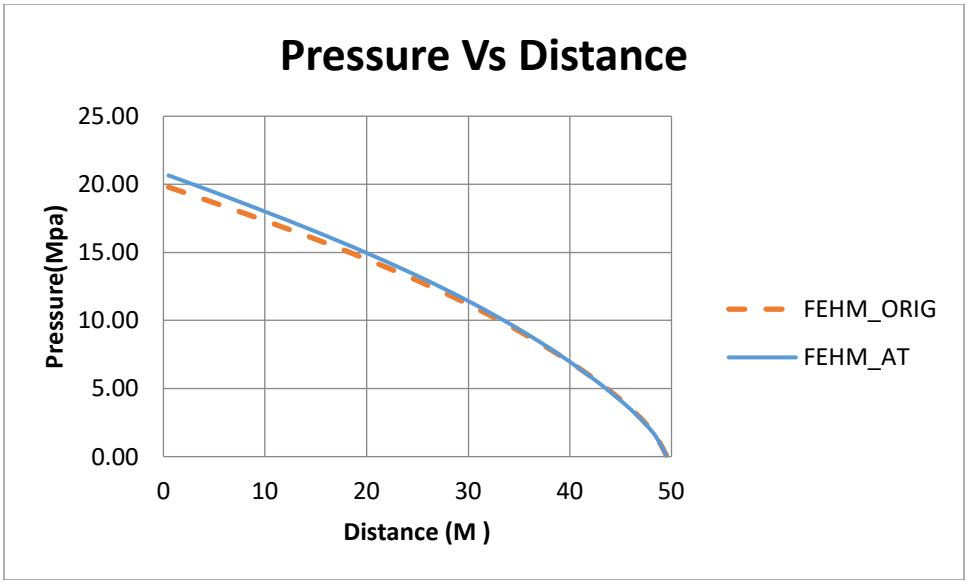

Figure 4-3. Comparison of table and previous existing properties in FEHM

4.5 Other AWH and Salt activities

1. Improvement of numerical performance during phase changes. The change of phase is especially important because of relative humidity. The more accurate prediction of partial gas pressures has decreased iteration count and re-started timesteps by 20 % in simple problems. Testing continues and it could be more important in simulations with more complex and highly resolved grids.
2. Increased the stability of the coupling between the species transport and reaction module, and fluid density coupling with salt.

4.5.1 Computation algorithm for fixed gridblock relative humidity and flowing relative humidity

Gridblock fixed relative humidity (hu)
Input parameters: th-reference temperature, ph-reference pressure, hu-relative humidity
Gridblock parameters: ptotal-total gridblock pressure, pc-partial pressure of air, t-temperature

1. pv_hu = hu* psatl(th), where psatl(t) is the saturation pressure of water, a function of t
2. pdiff=ph-pc, where pdiff is current gridblock water vapor pressure with respect to the reference pressure.
3. sk_hu= Aw*(pdiff-pv_hu), where sk_hu is a water flowrate based on the departure of the water vapor from the relative humidity*pv_hu, Aw is a physically based parameter.
4. skair_hu = Aair*(ptotal-ph), where skair_hu is a air flowrate based on the departure of the gridblock pressure from the reference pressure, Aair is a physically based parameter

5. enth_hu = Ehu*(t-th), where enth_hu is a enthalpy flow base on the departure of the gridblock temperature from the reference temperature, Ehu is a physically based parameter

The algorithm above is simple and the water, air, and enthalpy flows in or out of the gridblock keep it at the specified humidity.

Flowing relative humidity (huf).
This humidity boundary condition insures that the incoming gas flow (from another boundary condition) is at the specified humidity at the reference temperature and pressure set with the th, ph keywords and caveats described earlier):

1. pv_hu = huf* psatl(th)
2. pc_hu = ph-pv_hu
3. calculate (or table lookup) : air_density and water_vapor_density at th and pc_hu and pv_hu respectively
4. calculate the air_mass_fraction = air_density/(air_density+ water_vapor_density)
5. divide the incoming gas flow into air and water vapor flows using the air mass fraction
6. calculate the enthalpy inflow rate using the air_mass_fraction and the enthalpies for air and water vapor

5. Modeling

5.1 Model Development

Initial model development was based upon the full three dimensional mesh developed for Phase 1s (Guiltinan et al., 2020). The new mesh is 20m wide x 20m tall x 10m deep and contains 1,003,995 nodes. The locations of each borehole in the model was based upon the "as-built" diagram constructed after the drilling of the Phase 1 boreholes (Figure 5-1, Kulhman et al, 2020). Drilling of the boreholes was completed on April 29, 2019 and they were subsequently surveyed to develop the "as-built" which shows the final drilling location of each borehole, as well as its dip and orientation. The mesh does not include each borehole's dip and orientation and instead represents each borehole as a straight line of nodes. The line of nodes is located at the closet node which places the borehole in the correct location within the plane of the heater, and thus the borehole locations at the drift face look different than the "as-built" (Figure 5-2). The model is highly resolved around the central borehole and the resolution decreases with distance from the center. The central borehole itself includes an "air" zone, a "packer" zone, and a "heater zone". These zones can be seen in the three dimensional representation of the model (Figure 5-3).

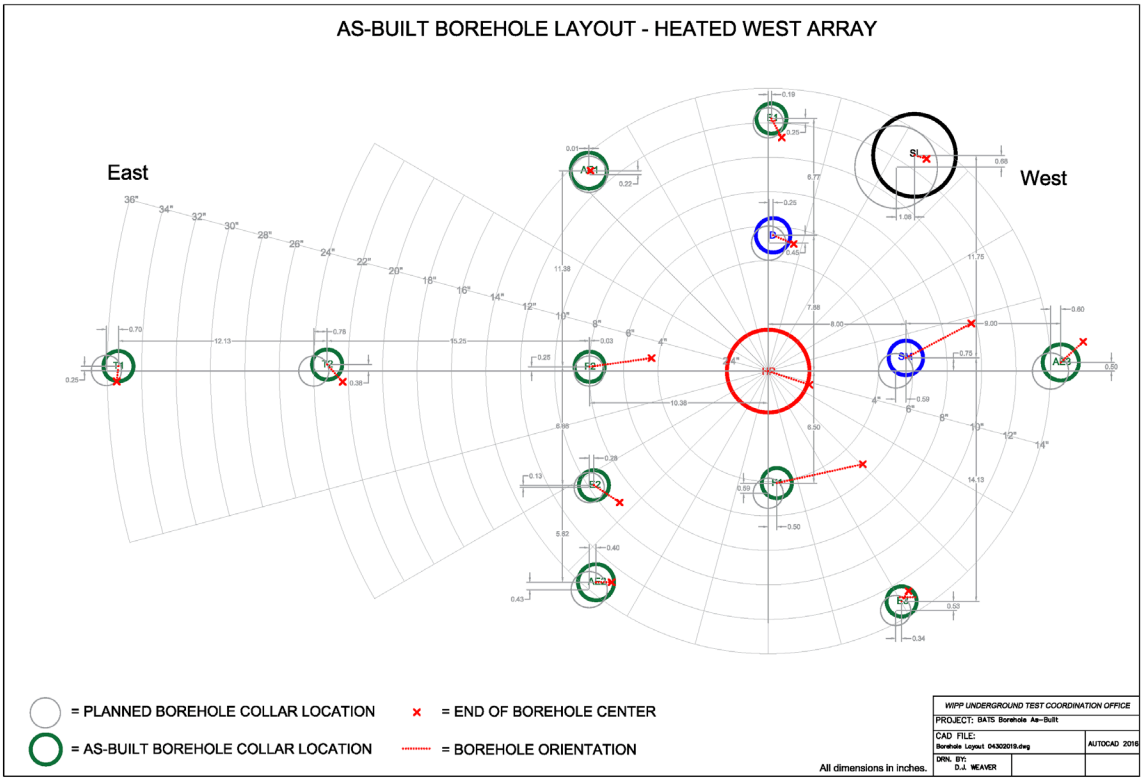

Figure 5-1. As-built locations and orientations of the boreholes in the heated array. From Kuhlman et. al, 2020

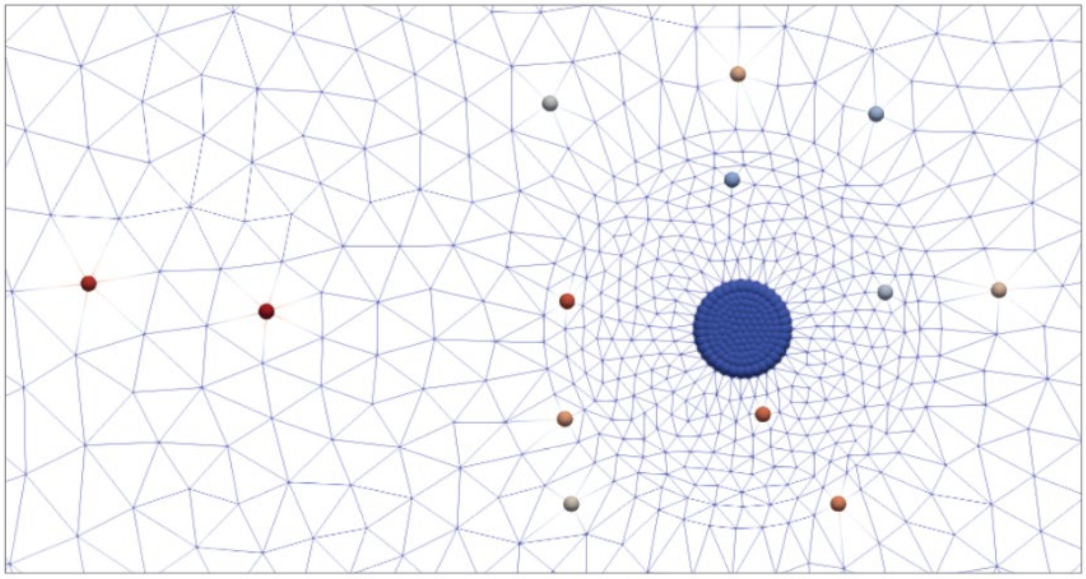

Figure 5-2. Borehole locations at the drift face in the three dimensional Phase 1 model domain

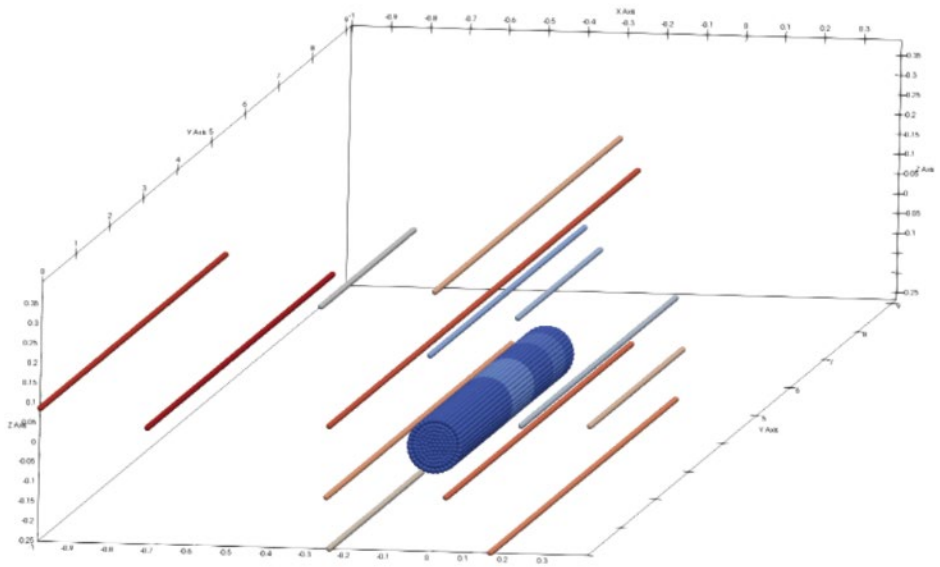

Figure 5-3. Three dimensional representation of the model.

Due to the extremely low permeability of intact salt, developing an initial state pore pressure and saturation distribution is critical for model accuracy. The pressure and saturation distribution were developed in a similar way as our Phase 1s model (Guiltinan et al., 2020). The Phase 1 boreholes are located on the south side of the N-940 drift which was excavated 7 years prior to the drilling of the Phase 1 boreholes. To develop the initial state pressure and saturation profiles our model was initialized with a background formation pressure of 12 MPa and an atmospheric pressure and zero saturation condition along the drift face (Figure 5-4). The far field formation

pressure should approach the lithostatic stress of 15 MPa, however local stress relief due to the WIPP excavation results in lower formation pressures during experiments (Beauheim, 1997; Beauheim and Roberts, 2002). Once initialized the model is ran for a period of 7 years. This develops the pressure and saturation conditions at the time of drilling. Next, the boreholes are placed within the model as areas of zero saturation with high permeability (1e-12 m^2). During the Phase 1s simulations the model was run for an additional 6 years but here the model is used immediately with no further equilibration time. Thus, these models represent fresh boreholes that were immediately instrumented. In reality, these boreholes equilibrated for approximately 8 months. Future modeling of Phase 1a and Phase 1b will account for this equilibration time. Other important modeling parameters are presenting in Table 5-1.

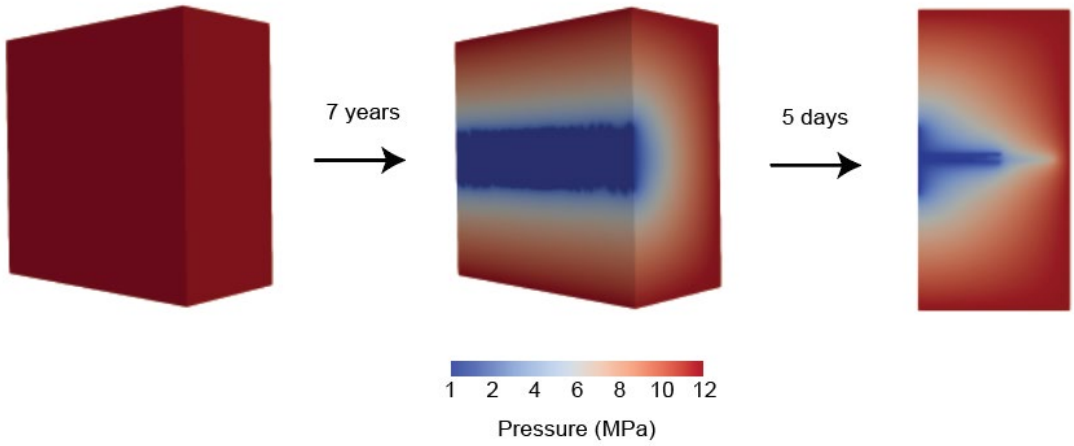

Figure 5-4. The initial pressure distribution development for the Phase 1a model. The model is initialized with a formation pressure of 12 MPa and an atmospheric pressure and zero saturation boundary condition representing the drift face. The model is ran for 7 years to develop the initial pressure and saturation condition for the model. On the right, a slice through the center of the model showing the pressure around the boreholes after 5 days.

Table 5-1 Key initial parameters used for Phase 1a borehole simulations

Parameter (units)	Value
Salt initial porosity (-)	0.001
Salt initial permeability (m^2)	10^{-21}
Damaged rock zone permeability (m^2)	10^{-18}
Damaged rock zone thickness (m)	0.08

Borehole permeability (m^2)	10^{-12}
Packer permeability (m^2)	10^{-26}
Salt thermal conductivity at 31.5 ºC (W/m K)	5.25
Air thermal conductivity (W/m K)	0.03
Initial formation pressure (MPa)	12
Initial formation temperature (°C)	28.5
Air source behind heater (kg/sec)	3.83×10^{-26}
Residual saturation (-)	0.1
Maximum capillary pressure (MPa)	1.00
Saturation at which capillary pressure is zero (-)	1.00

5.2 Initial Results of 3D Model

Phase 1a heating began on January 21st and ended February 18th 2020 (28 days). A 750 W quartz lamp infrared heater was used to heat the formation. A Watlow controller was used in conjunction with a thermocouple near the heating element to maintain a temperature of 120 °C while a backup thermocouple, located near the LVDT, was used an emergency over-limit check (Figure 5-5, Kuhlman et al., 2020).

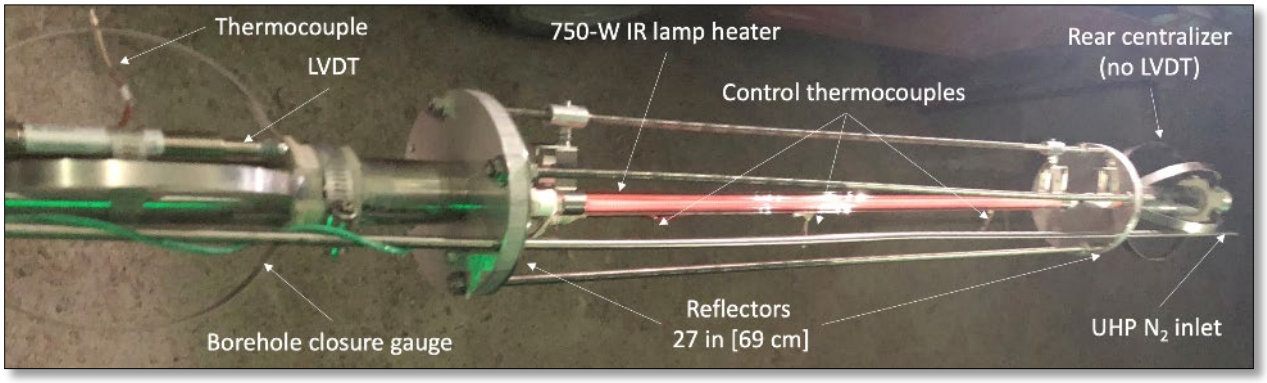

Figure 5-5. 750W Infrared heater, borehole closure gage, and thermocouples. From Kuhlman et al, 2020

Initial model runs targeting a 120 °C borehole wall temperature significantly overestimated the observed temperature at surrounding boreholes. Although the experimental setup is similar to that used during the Phase 1s experiment it is believed that the thermocouple controlling the heater was likely in poor contact with the salt and absorbing infrared radiation directly from the heater. This may have caused the thermocouple to report artificially high temperatures to the

Watlow controller resulting in lower overall borehole wall temperatures. One line of evidence is shown in (Figure 5-6). The thermocouple in direct line of sight to the infrared heater is stable at 120 °C while the thermocouple near the LVDT, out of sight of the infrared, is only 65 °C.

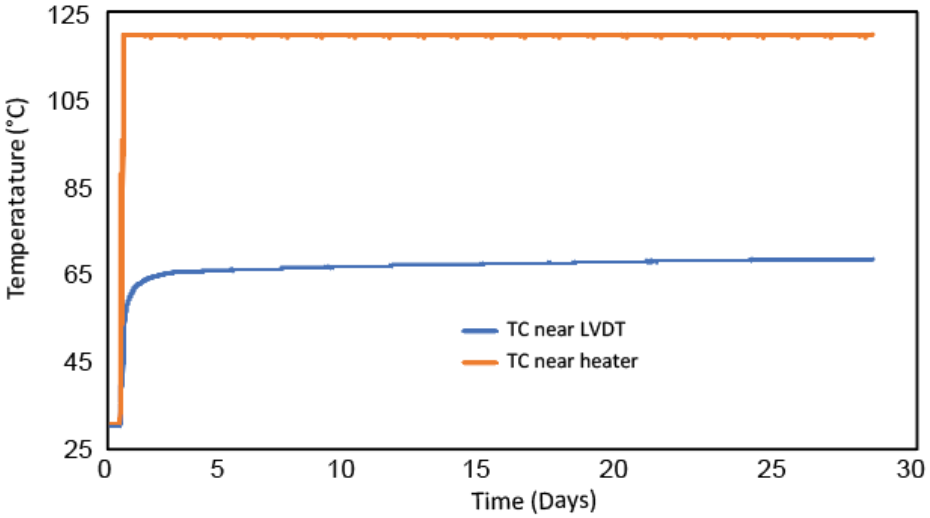

Figure 5-6. Temperature at thermocouple control near heater compared to nearby thermocouple.

After overestimating the temperature using a 120 °C constant heater source, a 480 W heater source was applied to the model and compared to the experimental data. Figure 5-7 presents a cross section of the model in the plane of heater at the end of heating. Lower saturation zones around the higher permeability boreholes can be seen. Boreholes fully grouted with cement are treated as intact salt and do not appear in these figures.

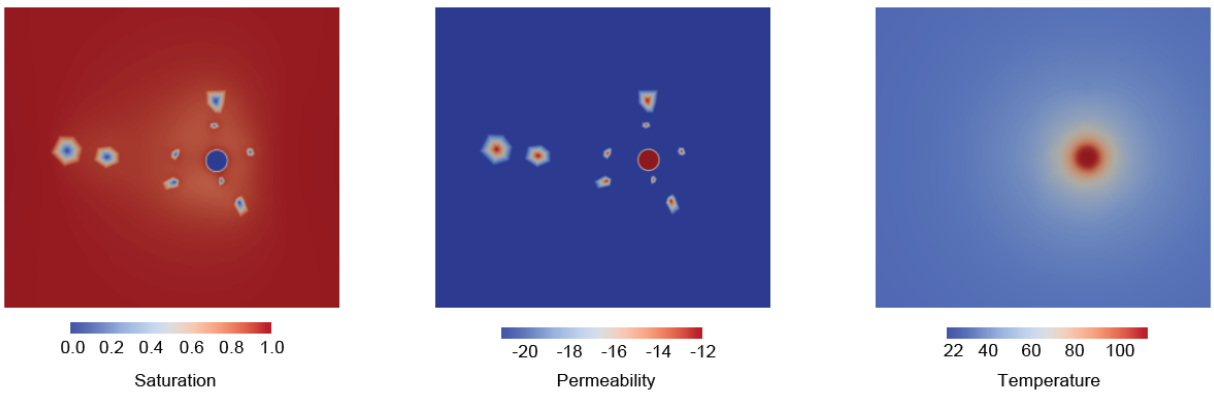

Figure 5-7. Saturation, permeability, and temperature in the parallel to the drift face in the plane of the heater

All intact salt was given the same variable thermal conductivity model used during the Phase 1s model, which is:

$$\lambda_{IS} = \lambda_{IS,300}\left(\frac{300}{T}\right)^{\gamma_1} \tag{5-1}$$

where γ_1 is 1.14 and $\lambda_{IS,300}$ is 5.4 (W/m*K). However, this thermal conductivity and the 480W heat source overestimated the temperatures in the salt formation. The temperature at the two temperature boreholes, T1, and T2 are shown in Figure 5-8. TC-8 is the warmest thermocouple in each borehole and is in the plane of the heater. TC-10 and TC-6 are deeper and shallower, respectively.

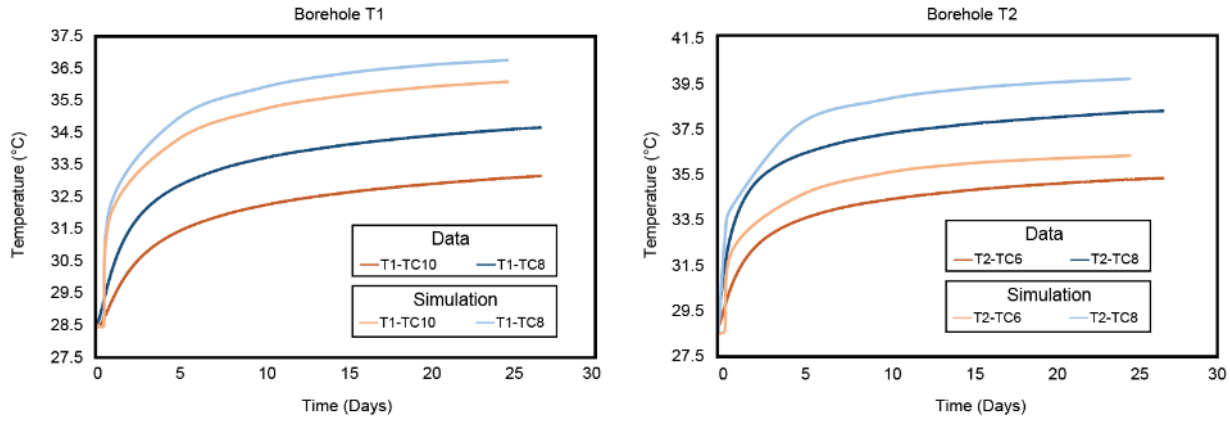

Figure 5-8. Phase 1 3D simulation results. Left, the temperature response in borehole T1. Right, temperature response in Borehole T2. TC8 is in the plane of the heater and thus the warmest thermocouple. TC-10 and TC-6 are deeper and shallower than TC-8, respectively.

5.3 2D Radial Model

To quickly investigate the effect of the thermal conductivity of the intact salt, damaged rock zone, and other parameters a simpler 2D radially symmetric model was constructed. The model is centered around the heated borehole with a secondary borehole (HT2) surrounded by a DRZ. The radially symmetric nature of the model prevents the inclusion of a third borehole because it would be entirely shadowed the by first. The model is 10m by 10m and includes 3,458 nodes. The initial permeability of the borehole, packer, intact salt, and DRZ are shown in Figure 5-9.

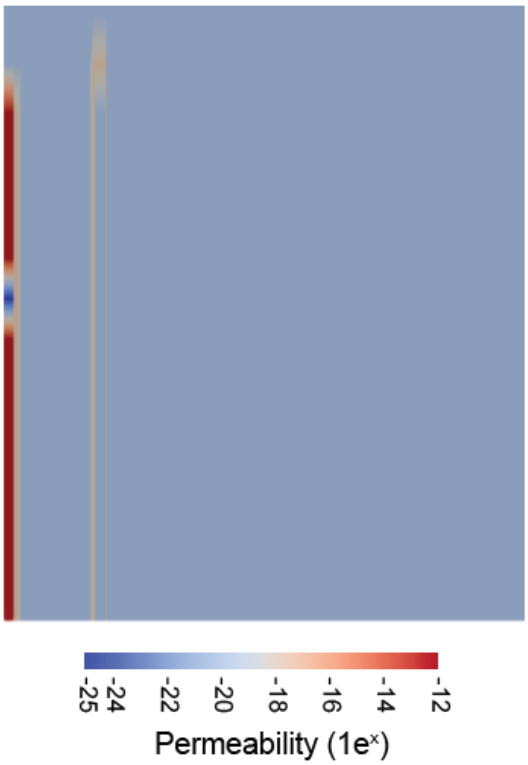

Figure 5-9. Permeability in 2D radial model of the Phase 1 experiment.

In this simplified model no initial pressure and saturation development were conducted. The point of these simulations was simply to explore the effects of heating and thermal conductive on the formation temperature. To approximate the wattage of the Phase 1 experiment the heater was step wise changed from a high of 593 watts at time zero to a low of 495 watts at 5 days (Table 5-2). The 495W heating was continued for 30 days.

Table 5-2 Heating schedule during the 2D radial Phase simulation

Time (Days)	Heater Wattage
0	593
0.5	548
1	530
2	514
3	504
4	498
5	495

Equation (5-1) with $\lambda_{IS,300}$ equal to 5.4 (W/m*K) represents the thermal conductivity of intact halite (Johnson et al., 2019; Munson et al., 1990). However rock salt, is not pure halite and is instead composed of polyhalite, halite, anhydrite, gypsum, and clays giving it a range of $\lambda_{IS,300}$ from 4.5 to 5.5 (W/m*K). By systematically altering our thermal conductivity we find a $\lambda_{IS,300}$ equal to 5.15 very closely matches the thermal response in HT2 (Figure 5-10). Thermal conductivity measurements of the salt cores and grout are being conducted at Sandia. These measurements will help constrain our modeling efforts and will be included in future models of Phase 1a, and Phase 1b.

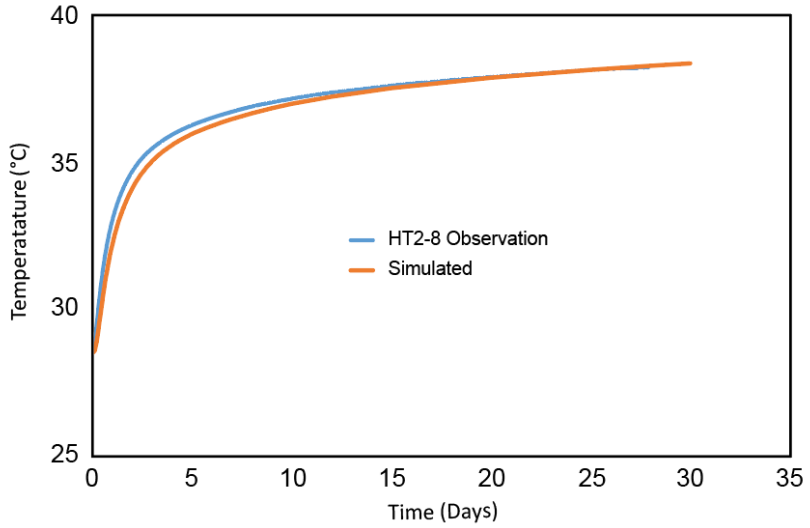

Figure 5-10. Temperature result at HT2-8 using $\lambda_{IS,300}$ = 5.15 for intact salt and step heating schedule shown in Table 5.2.

5.4 Isotopic Simulations

A primary goal of the BATS investigation is to understand the distribution, composition, and abundance of brine to sources of heat in salt formations. The three potential brine sources are interstitial brine, fluid inclusions, and mineral bound water. Each of these sources potentially has its own isotopic signature which can be used in conjunction with numerical simulations and field measurements to determine the source of brine to heat. As part of this effort LANL is conducting laboratory experiments to characterize the isotopic signature of brine and measuring the isotopic signature of water removed from the heated borehole (Chapter 3). However, an important aspect of the isotope work is the development of accurate isotopic transport models. The development of these models and the laboratory techniques to measure the different isotope sources is being conducted in conjunction with each other and ahead of the planned isotope tracer experiment scheduled for Phase 1b, later in 2020. Here we report on the current state of the isotope modeling work at LANL, which is still in the developmental stage.

The transport of stable isotopes in partially saturated media was originally incorporated into FEHM to simulate deuterium and ^{18}O movement through the vadose zone at the Nevada Test Site (Kwicklis et al., 2006). Transport of each phase, $H_2{}^{16}O$, $H_2{}^{18}0$, and $HD^{16}O$ are tracked as separate species with their own liquid and vapor diffusion and Henry's law partitioning

coefficients. Molecular diffusion coefficients for the model are based upon work by Smiles et al, (1995) and Henry's partitioning by Friedman and O'Neil (1977) and Marilvate and Coantic, (1975). Table 5-3 presents the important isotope transport parameters used for simulating isotope movement at WIPP.

Table 5-3 Diffusion and Henry's law parameters for isotope modeling

Isotope species	Henry's Law Constant (Mpa)	Fractional Henry's Law Constant	Vapor Diffusion Coefficient	Liquid Diffusion Coefficient
$H_2{}^{16}O$	2.332×10^{-3}	1.0000	2.57×10^{-5}	2.23×10^{-9}
$H_2{}^{18}O$	2.309×10^{-3}	0.9903	2.50×10^{-5}	2.23×10^{-9}
$HD^{16}O$	2.149×10^{-3}	0.9217	2.51×10^{-5}	2.23×10^{-9}

To begin testing isotope transport modeling a simplified two dimensional 7m by 3m radially isotropic mesh was generated (Figure 5-11).

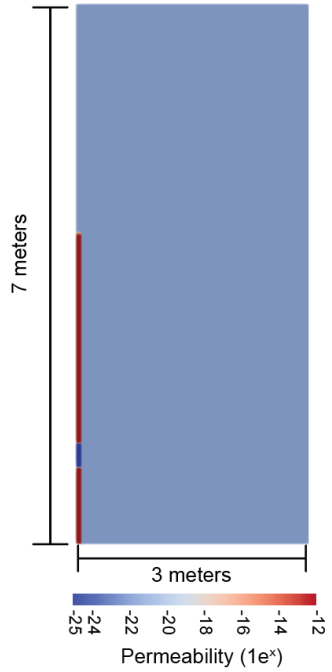

Figure 5-11. Permeability distribution of 2D radial isotope simulation with borehole (red), packer (dark blue), and intact salt (light blue)

The borehole is initialized in the center of the model (around the x = 0 point). The borehole is initialized with no D or $^{18}0$ while the intact salt is initialized with 0.01721 mol D/kg water and 0.111723 mol $^{18}0$/kg water (Figure 5-12). These concentrations correspond to -5 δD and +3 $\delta^{18}O$ which approximate the concentrations measured at WIPP (Lambert, 1992). Delta notation is calculated against Vienna Standard Mean Ocean Water according to:

$$\delta^{18}O = \left[\frac{\left(\frac{^{18}O}{^{16}O}\right)_{Sample}}{\left(\frac{^{18}O}{^{16}O}\right)_{VSMOW}} - 1\right] x\ 1000\ ‰ \quad (5\text{-}2)$$

where $\left(\frac{^{18}O}{^{16}O}\right)_{VSMOW}$ is 2005.2 ppm and $\left(\frac{^{2}H}{^{1}H}\right)_{VSMOW}$ is 155.76 ppm. A background formation pressure of 12 MPa is applied to formation and along the right most wall while the borehole is initialized at atmospheric pressure. The formation is fully saturated and the borehole is completely unsaturated.

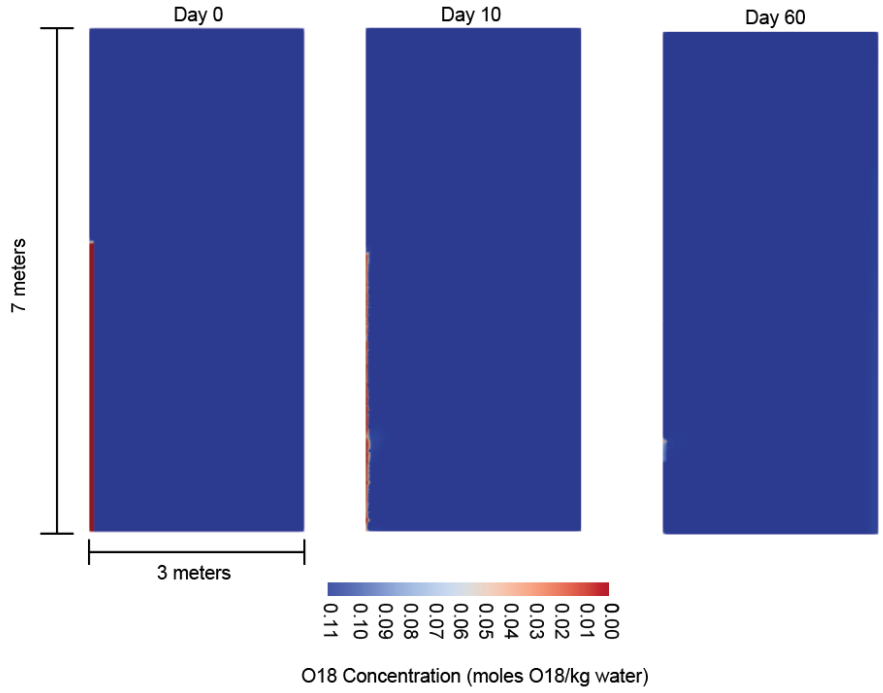

Figure 5-12. Initial Isotope Experiment. A borehole with no isotopic $^{18}0$ is flooded with $^{18}0$ from nearby salt formation.

At time zero the borehole has no D or $^{18}0$, but the formation pressure driven advection and molecular diffusion cause the ^{18}O to fill the borehole. The background formation concentration of ^{18}O has nearly occupied the entire borehole by 60 days. The inclusion of a higher permeability DRZ and an atmospheric boundary condition in the borehole would likely speed this equilibrium.

After successfully benchmarking to this simple experiment the conditions of the Phase 1a heating and nitrogen flow were applied (section 5.3). However, the vapor phase concentration of the isotopes is calculated using the partial pressure of water according to fractional Henry's law constant (Table 5-3) and with dry nitrogen and high heat the saturation within the borehole remains extremely low. Instability in isotope concentrations at very low water saturation is currently causing numerical artifacts in the very dry regions of the numerical simulation. Efforts

to modify the source code to correct vapor phase isotopic concentrations in the presence of extremely low saturation values is ongoing and will be reported in following milestones.

5.5 Vadose Zone Journal Publication

The following section presents our recent publication from the Vadose Zone Journal (Guiltinan et al., 2020). This journal publication was a close collaboration between LANL, LBNL, and SNL. The publication was tied to the journal cover (Figure 5-13), generated a news article (https://www.agronomy.org/news/science-news/are-salt-deposits-solution-nuclear-waste-disposal), was featured in the LANL Science Highlights, and inspired a poetry blog (below).

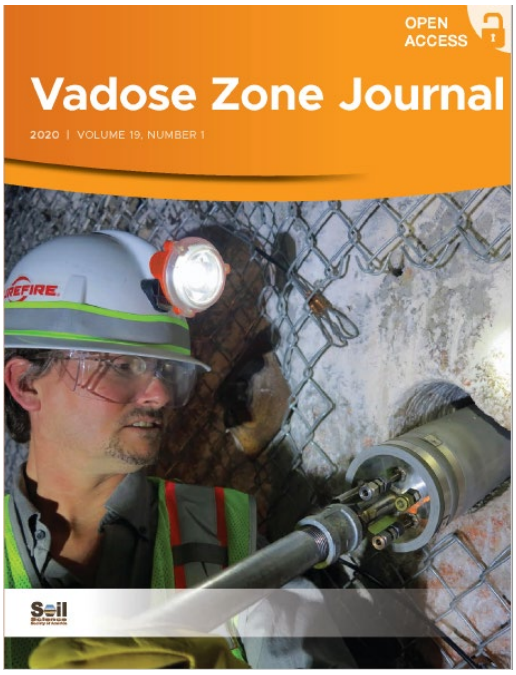

Figure 5-13. Vadose Zone Journal cover.

Salt Poem Link:

From: Sam Illingworth <sam.illingworth@uwa.edu.au>
Sent: Friday, May 1, 2020 2:04 AM
To: Stauffer, Philip H
Subject: [EXTERNAL] Science poem about your research

Hello,
I was inspired to write this poem by your fascinating research into how salt deposits are a potential solution for nuclear waste disposal:
https://thepoetryofscience.scienceblog.com/1275/**salting-the-earth**/
This work will also feature in the next episode of my podcast, to be released on Monday morning: https://scipoetry.podbean.comhttps://scipoetry.podbean.com/
I hope that you enjoy it. :-)
Sam

6. Permeability Measurements

6.1 Borehole Pressure Decay Experiments

Borehole permeability testing was conducted in June of 2019 and July of 2020. Borehole permeability testing was performed by a series of pressurizations of the confined borehole area and observation of the pressure decay. The packer system was inflated to approximately 50 - 80 PSI to isolate the borehole area behind the packer. The permeability testing is performed by pressurizing the confined borehole area to as high as 45 PSI and observing the pressure decay through a pressure gauge connected to a pass through pipe that connects to the confined area through the packer. The pressure readings were recorded using a data logger and processed numerically to determine the borehole permeability. Table 6-1 presents the borehole intervals tested.

Table 6-1 A summary of the permeability tests conducted on the Phase 1 borehole configurations

Array	Borehole ID	Actual Depth, ft	Interval Tested, ft	Date
Heated	HP	12.23	9.03 to 12.23	6/12/2019
Heated	HP	12.23	9.06 to 12.23	6/13/2019
Heated	HP	12.23	9.06 to 12.23	6/18/2019
Heated	HP	12.23	9.06 to 12.23	6/18/2019
Heated	HP	12.23	7.03 to 12.23	6/18/2019
Heated	HP	12.23	5.03 to 12.23	6/18/2019
Heated	SL	8.08	5.03 to 8.08	6/18/2019
Heated	SL	8.08	5.03 to 8.08	6/19/2019
Heated	SM	15.01	5.00 to 15.01	6/19/2019
Heated	SM	15.01	7.00 to 15.01	6/19/2019
Heated	D	15	5.00 to 15.00	6/19/2019
Heated	D	15	5.00 to 15.00	6/19/2019
Unheated	HP	12.13	5.03 to 12.13	6/24/2019
Unheated	SL	8.05	5.03 to 8.05	6/24/2019
Unheated	D	15	5.00 to 15.00	6/24/2019
Unheated	D	15	7.00 to 15.00	6/24/2019
Unheated	D	15.00	4.07 to 15.00	7/14/2020
Unheated	HP	12.13	6.245 to 12.13	7/14/2020
Heated	D	15.00	5.8 to 15.00	7/14/2020
Heated	HP	12.23	6.365 to 12.23	7/14/2020

Unheated	HP	12.13	6.245 to 12.13	7/16/2020
Unheated	D	15.00	6.07 to 15.00	7/16/2020
Heated	D	15.00	6.00 to 15.00	7/20/2020
Heated	D	15.00	9.00 to 15.00	7/23/2020
Unheated	D	15.00	6.07 to 15.00	7/27/2020
Unheated	D	15.00	6.07 to 15.00	8/4/2020
Unheated	D	15.00	6.07 to 15.00	8/11/2020

In general the drift DRZ was determined to extend approximately 4 to 5 feet in to the rock salt. Pressure tests less than 5 feet deep rapidly lost pressure. Gurgling sounds were noted during several tests which could be air escaping around the packer through fractures in the borehole DRZ. At times these gurgling sounds were lessened by increasing the inflation pressure within the packer. This could be due to the increased pressure from the packer closing off DRZ fractures or a poor packer seal in the borehole being corrected by high pressure. Several permeability tests were conducted in the HP borehole of the heated array where the Phase 1 packer is placed. One such test, which did not gurgle and lost only a small amount of pressure is analyzed in Figure 6-1. FEHM simulations utilizing a 3 inch DRZ surrounding the HP borehole predict that the HP DRZ permeability is near 2×10^{-17} m^2 (Figure 6-1). This DRZ permeability falls within the range of $3\ x\ 10^{-16}$ to $2\ x\ 10^{-23}$ m^2 as reported by (Beauheim and Roberts, 2002).

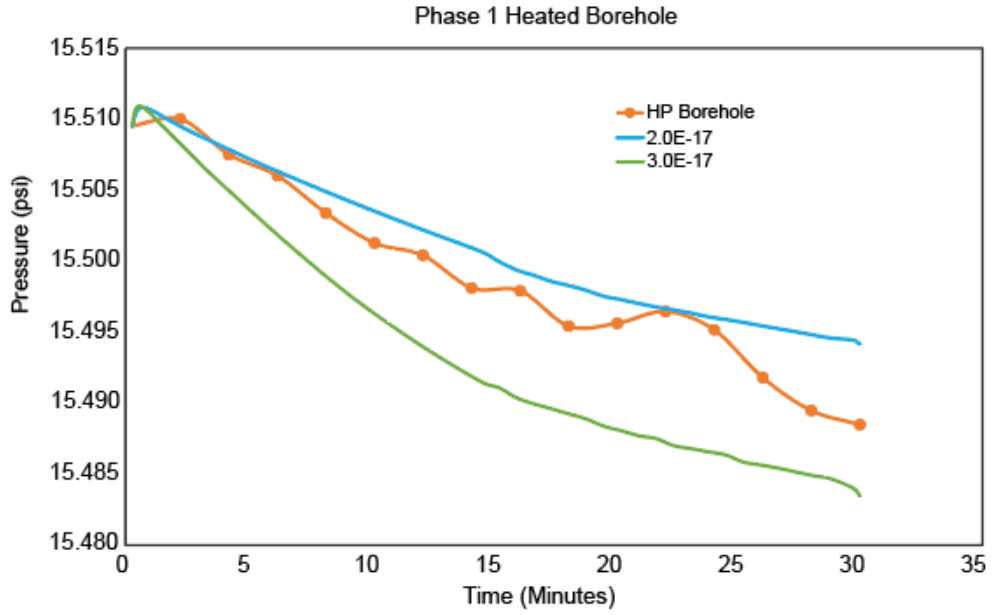

Figure 6-1. Permeability testing data compared to FEHM simulations of the heated borehole in the Phase 1 borehole configuration. The data is approximately matched with a permeability of 2e-17 m^2.

During the 2020 field permeability measurements several tests resulted in rapid pressure loss despite being placed beyond the drift DRZ. Subsequently two packers were discovered to be leaking and unusable, casting doubt on some of the 2020 permeability measurements (Figure 6-2). These packers were sent back to the manufacture for repair and pressure testing.

Figure 6-2. Leaky packer detected during permeability experiments.

6.2 U D Borehole Threshold Pressure Testing

In low permeability formations such as shales, tight sandstones, some carbonates, and salt formations the capillary threshold pressure can be a significant barrier to conducting permeability testing. The size of the threshold pressure is controlled by the pore structure and interfacial tensions of the corresponding fluids (Guiltinan et al., 2018). Previous work by Davies (1991) attempted to correlate the permeability of the salado formation to the threshold pressure of nitrogen. Equation 6-1 rearranges their correlation (Equation 11 in Davies, (1991)) to express permeability in terms of nitrogen threshold pressure.

$$k[m^2] = \left(\frac{P_{cap}[MPa]}{5.6*10^{-7}}\right)^{-2.89} \quad (6\text{-}1)$$

During permeability testing the U-D borehole did not leak when initially pressurized to approximately 8 psi (Figure 6-3). This is likely due to 8 psi not exceeding the threshold pressure. In an attempt to characterize the threshold pressure and conduct permeability testing the U-D borehole pressurize was increased in stages over approximately 4 weeks to a maximum pressure of approximately 45 psi. At 45 psi the threshold pressure was exceeded and drawdown of the borehole pressure began to occur.

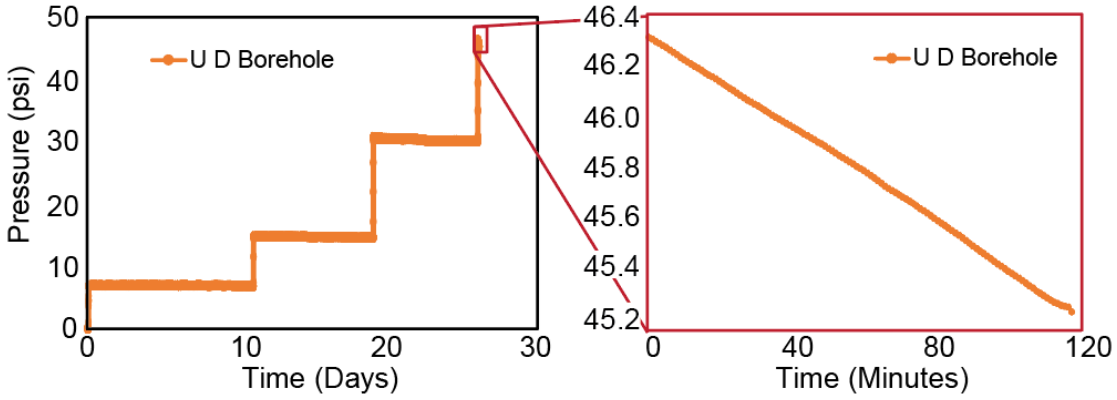

Figure 6-3. U-D nitrogen breakthrough pressure experiment

The result of this experiment is that the threshold pressure in the U-D borehole was measured to be between 30 and 45 psi. Applying this to equation 6-1 yields an estimated permeability of between 8.1e-17 m^2 and 2.5e-17 m^2. These values approximate those presented in Davies (1991) for the damaged rock zone (Figure 6-4).

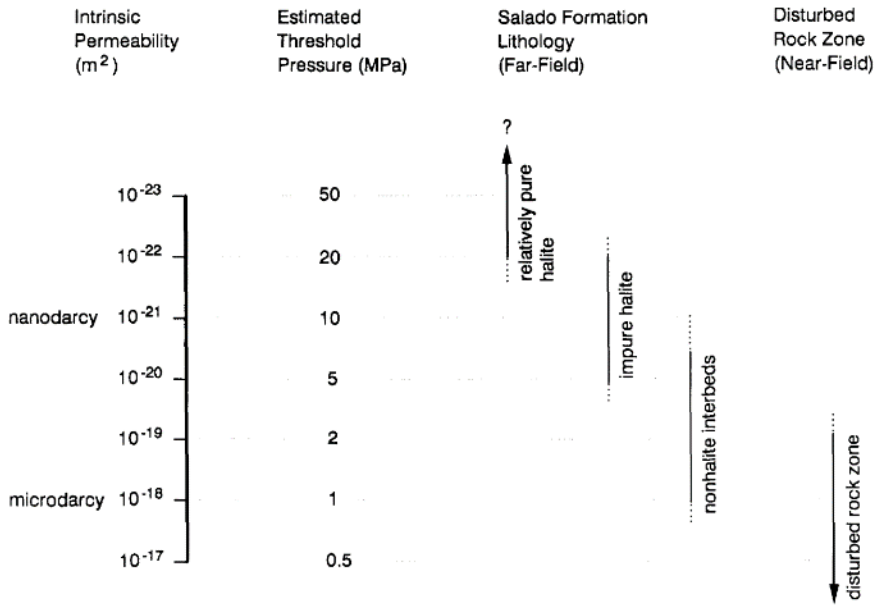

Figure 6-4. Permeability and threshold pressure in the salado formation. From Davies (1997)

FEHM modeling was conducted to estimate the permeability of the borehole from the pressure decay (Figure 6-4). Similarly to the results presented in figure 6-1, the model was composed of a borehole embedded in intact salt with a 3 inch DRZ. The linear pressure decay of the U D borehole is not fit well with the linear relative permeability model used for these simulations however the permeability estimated of approximately 6e-17 m^2 fits within the expected range of the DRZ as well as the range estimated by equation 6-1. Future permeability simulations will explore the use of different relative permeability models and potentially other conceptual models of the DRZ possibly including a discrete fracture network DRZ.

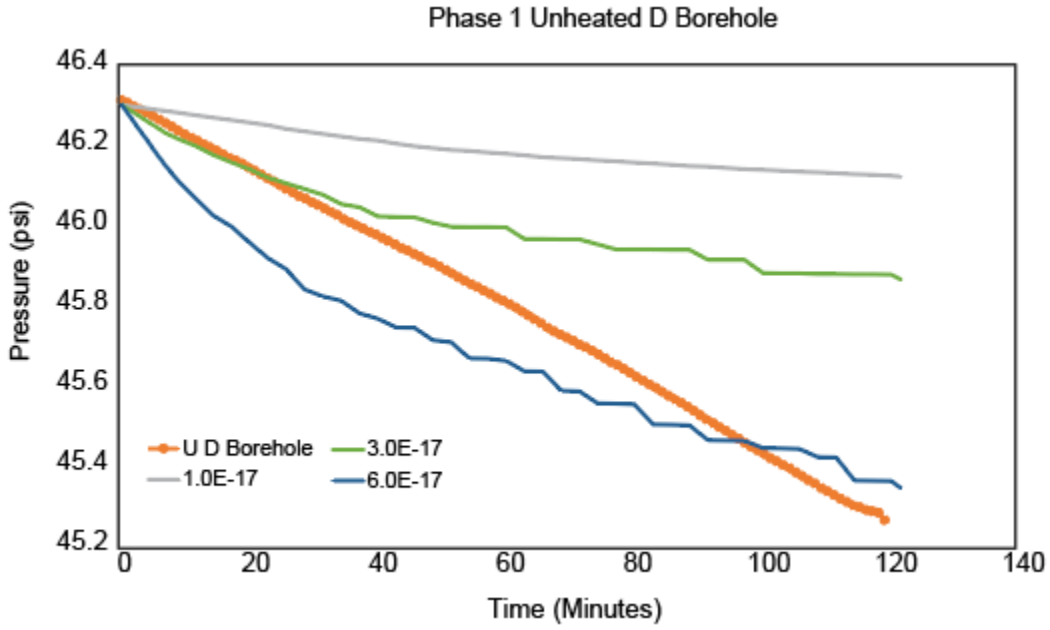

Figure 6-5. Phase 1 U-D permeability simulation.

7. BATS Lessons Learned

The following list of lessons learned was compiled by the LANL-WIPP repository science and operations group with input from LANL, LBNL, and SNL.

Pre-test planning

1. Typically a test plan exists prior to a test. For the BATS test there was not a formal test plan, but a SAND report and test inventory list were in place early on which provided guidance for the test.
    a. All members of the collaboration need to read, review, and understand these documents early on to address procurements, planning, and suggest any changes/additions that are needed prior to field deployment.

Equipment ranges parameters

1. Document all equipment parameters and ranges very early on and define what equipment is the limiting factor in applicable systems. Example the Licor is the limiting factor for the flow rate.
    a. This information is used for developing work control.
    b. This information is used for procurements, such as safety valves, pressure transducers etc.
    c. This information is used for conducting the experiment and knowing that system operation in the experiment is within the correct parameters.

Procurements/purchasing

1. Purchase extra parts and pieces.
2. Start procurements early, many procurements have long lead times.

Test Initiation

1. Ideally the BATS test would have been instrumented and commenced much sooner than it was. There are semi-uncontrollable factors where WIPP is involved – borehole drilling and power.
    a. Ideally, power would be provided at the test location prior to borehole drilling.
2. As much as possible, all test instrumentation/systems are prepared, tested, and vetted before any borehole drilling starts.
3. As soon as possible after boreholes are completed and borehole as-builds are documented instrumentation/system installation needs to start.

Borehole Drilling

1. One borehole was drilled with the wrong size bit. Ensure the proper size bit is used.
2. Some boreholes were drilled with the incorrect horizontal angle. Ensure as best as possible the horizontal angle is correct.

For TC's in grouted boreholes

1. Consider using hermetically sealed (measurement end) TC's – they were not available for this test due to an issue at the Omega manufacturing facility.
2. If hermetically sealed TC's are not available then the measurement ends should be coated with RTV, silicone, or JB weld.

3. If hermetically sealed TC's are not available then the wiring end outer insulation should be cut back ~24 to 36 inches to prevent brine from reaching the measurement to channel. Perhaps this should be done for hermetically sealed TC's as well for a conservative approach.

TC placement in boreholes

1. Determine the heater placement early in the planning stage.
2. Align TC's in surrounding boreholes based on the location of the heater, where the TC's are nearly identical in distance positioning – i.e. if the heater center is 9.00' then TC's in surrounding boreholes should all have TC's at 9.00' and this goes for all TC placement where there should be this type of alignment.

TC placement in the heater borehole

1. More TC's are needed in the heater borehole for measurements and backups due to the importance of heater measurements.
2. Locations within the borehole should address:
    a. 2 TC's for heater control, where 1 is a backup.
    b. Measurements should address both heater ends and the middle of the heater, where the TC's are located in a manner to touch the borehole wall.
        i. Perhaps there should be redundancy in the measurements as well.
    c. For the locations mentioned above there should also be TC's located closer to the heater for confidence that the TC's mentioned above are touching or near the borehole wall.

TC placement in the heater borehole - unheated

1. TC's used in the unheated borehole should be nearly identical in the position and distance placement as the TC's in the heated borehole – heated.

Documentation and Photos

1. More photos of instrumentation prior to inserting into boreholes with focus on measuring instruments with tape measure in photos for reference.
2. Measurements and documentation of instrumentation measurement locations prior to inserting instrumentation into boreholes.
    a. This was performed very well for the majority of the test, however there were times when this was not performed and instrumentation were removed to perform measurements.

Solenoids and gas circulation switching

1. If possible, consider removing solenoids and each array has identical instrumentation.
2. If solenoids are used due to instrumentation cost
    a. Build as much of the solenoid/plumbing system in the lab, not the underground.
    b. Use Teflon tape on non-swagelok fittings.
        i. Teflon tape was used on non-swagelok fittings for this test, however the Teflon tape was added after the system were built where leak checking revealed leaks at all non-swagelok fittings that did not have Teflon tape.
3. Purchase 2 times the amount of solenoids needed to have backup solenoids.

Gas plumbing

1. Ensure that plumbing to packers used for inflation has dedicated valves to each inflation line for making changes or troubleshooting the system.
2. Purchase new regulators with backups for the test, do not rely on used/old regulators.
    a. If used/old regulators are used then test them in the lab prior to use to ensure they are working as expected.
3. Extra parts and pieces – always have extra parts and pieces. Do not be shy when purchasing swagelok parts and pieces.
    a. Sandia was very good at this.
    b. LANL was not good at this.

Heated and Unheated Packer Assembly

1. TC's and instrumentation for the packer assemblies have wires that are run through pipes and fittings. The wires can be damaged during installation and the instruments will not work.
    a. Test each instrument after installation to ensure it is working as expected and not damaged.
    b. Have extra instruments on hand and replace damage instruments.
    c. Ensure instrument wires are labeled before and after installation to maintain instrument identity.
2. See **TC placement in the heater borehole** – now is the time to identify if TC's are located and positioned as desired.
3. Use robust, machined parts for the packer assembly. Originally a heater centralizer were jury rigged with parts and pieces. Sandia designed and built machined parts to centralize the heater and this was a major improvement.

SM – sample boreholes

1. Test the sample assembly prior to borehole insertion by connecting vacuum pump and testing terminal end of sample tube for vacuum.
    a. Address any vacuum issues if the exist.
2. Test the sample assembly after borehole insertion by connecting the vacuum pump.
    a. Address any vacuum issues if the exist. While inserting the assembly salt can enter the sample tube and this is the most likely problem.

Strain Gages

1. Test VW strain gages prior to building/assembling cement plug using the Geokon readout or datalogger.
2. Test waffle strain gages prior to building/assembling cement plug using datalogger.
3. Document the location of the strain gages prior to cementing and ensure wires are labeled to match documentation.
4. Test all strain gages (use same methods as in # 1 & 2) after cementing in plug.

Power controller and heater

1. Have an extra heater, which we do.
2. Measure the heater resistance and document when new.

3. Measure the heater resistance after the extension wires and plug are connected prior to using the heater.
4. Periodically measure the heater resistance after the extension wires and plug are connected after using the heater.
5. Ensure the datalogger and power controller are working, datalogger and power controller are communicating as expected prior to field deployment.
6. Ensure the power controller operation is understood and known prior to field deployment, i.e. the power measurement, current measurement, and other features.
7. Ensure the power controller assembly has correct fuses in place prior to field deployment.
8. Have the meters and instruments used in # 6 available in the field to test/troubleshoot the power controller when necessary.
9. Provide instruction for power controller use/configuration and document the configuration prior to field deployment.

Equipment/System operational instructions and organization

1. Provide operational instructions in concise and systematic order. Often times many sets of instructions exist for operating the same piece of equipment/system. Piecemealing and using the instructions after time has passed becomes difficult, time consuming, and leads to mistakes.
2. An organized system where all equipment/system operational instructions, schematics, and information is in one place is very valuable. This is currently in place, for the most part, and is very helpful.

ERT

1. Unexpected brine wires issue.
    a. This was potentially resolved with the extension cables. In the future consider designing a solution or ensure extension cables are used from the start.

Fiber Optic

1. Fiber channels were lost early on and this may be due to brine/wire issue and strain.
    a. Design improvement to address brine.
    b. Design improvement to address strain, loss of channels – more robust fiber protection?

Permeability Testing

1. Dedicated packers are best with limited pass throughs.
2. Test packers for inflation and circulation leaks prior to borehole use.
    a. Circulation checks need to be performed in a pre-built vessel assembly in order to ensure circulation pressure is constant behind the packer and there are no leaks. Highly suggest that there are two of these for the large and small packers that are underground at WIPP. ~5 psi capable vessel would be sufficient.
3. Small packers are difficult to work with since most of them leak for inflation.
    a. Consider another company for purchasing small packers.
    b. Have extra packers on hand, since several have failed.
4. Have dedicated pressure transducers for all inflation lines on every inflatable packer.

5. Consider having a tank dedicated to circulation for permeability testing if permeability testing is slated for periodic testing. If only before and after test permeability testing is necessary then a dedicated tank is not necessary.

8. SFWD Website

Over the last year we have built a website to serve as a central repository for LANL's salt repository science contributions to the Spent Fuel and Waste Disposition campaign. The website features journal articles, DOE reports, researcher profiles, and photo galleries. The site is intended to be a comprehensive look at the salt repository science we are doing for SFWD, and in particular, with respect to BATS.

The website is available at https://sfwd.lanl.gov. At the moment, the website is wholly focused on salt repository science. Over time, we will expand the scope of the site to encompass other aspects of SFWD including work on crystalline, argillite, and alluvial basins as host rocks for repositories.

8.1 Website Sections

The website is composed of four sections: Journals, DOE reports, WIPP Experiments, and People.

8.1.1 Journals page

On the Journals page, a comprehensive collection of all journal articles related to our work on this project can be found, along with their corresponding PDFs for download as well. In addition, the Vadose Zone Journal covers and *Poetry of Science* article (as described in Section 5.5 of this report) are featured.

8.1.2 DOE Reports page

The full PDFs of all salt related reports to the Department of Energy can be found within this subsection.

8.1.3 WIPP Experiments page

This page is intended to be a comprehensive look at the LANL experiments performed at the Waste Isolation Pilot Plant salt bed in Carlsbad, New Mexico. Specifically, there is a comprehensive overview of both Phase 1s/Phase 1 of BATS and the Heated Canister Test operational test.

To that end, this page features:

- A short, written overview describing the experiments
- Journal articles grouped by the experiment they were supporting
- DOE Reports grouped by the experiment they were supporting
- Photo galleries for BATS (Phase 1 and Phase 1s) and heater tests
- Conference papers and posters from WM2020

- Video and slides of the Stauffer and Kuhlman *DOE Salt Research and WIPP Test* talk given to the U.S. Nuclear Waste Technical Review Board
- Relevant WIPP and DECOVALEX links

8.1.4 People page

A number of LANL researchers have been critical to the progress and status of this work. In the People subsection, we feature those researchers along with their contact information and homepages.

8.2 Additional Comments

The LANL SFWD website is continuously updated and is intended to serve as a place for the public, other salt researchers, and those interested at the Department of Energy to learn about the work that LANL is doing, has done, and will continue to do. The site has already proven useful as a repository for our reports and publications for both LANL staff and collaborators in the US and internationally.

8.3 Screenshots of the Website

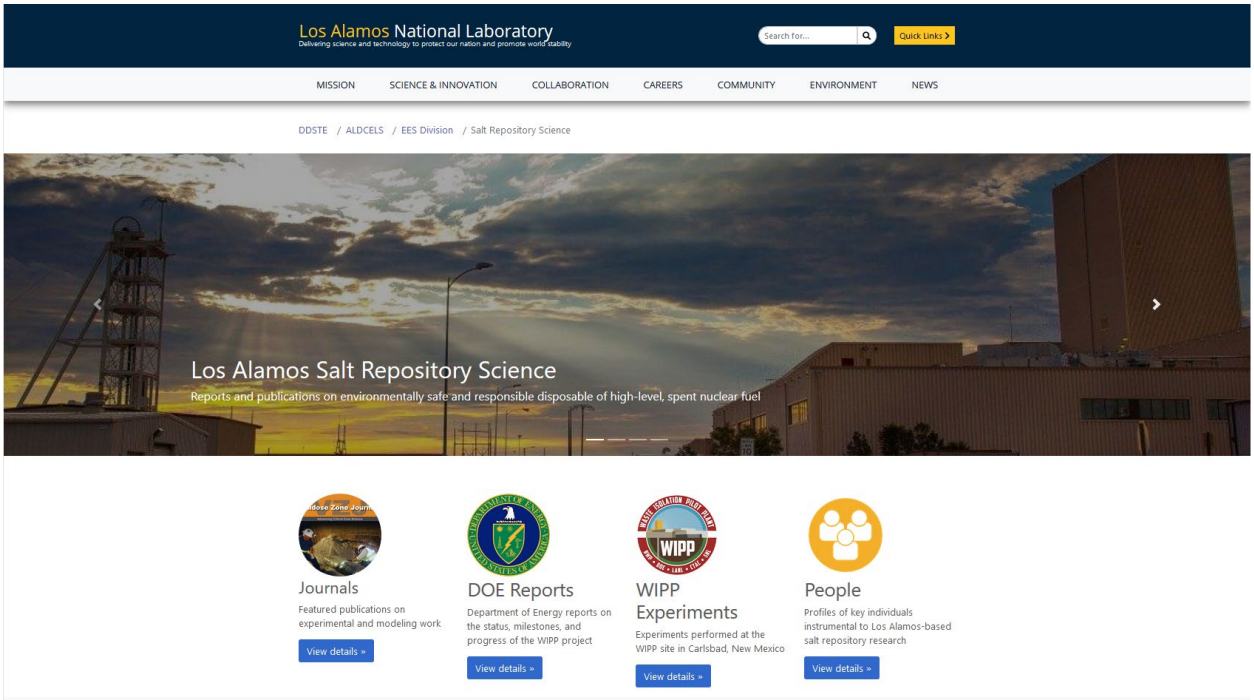

Figure 8-1. Homepage of the https://sfwd.lanl.gov website.

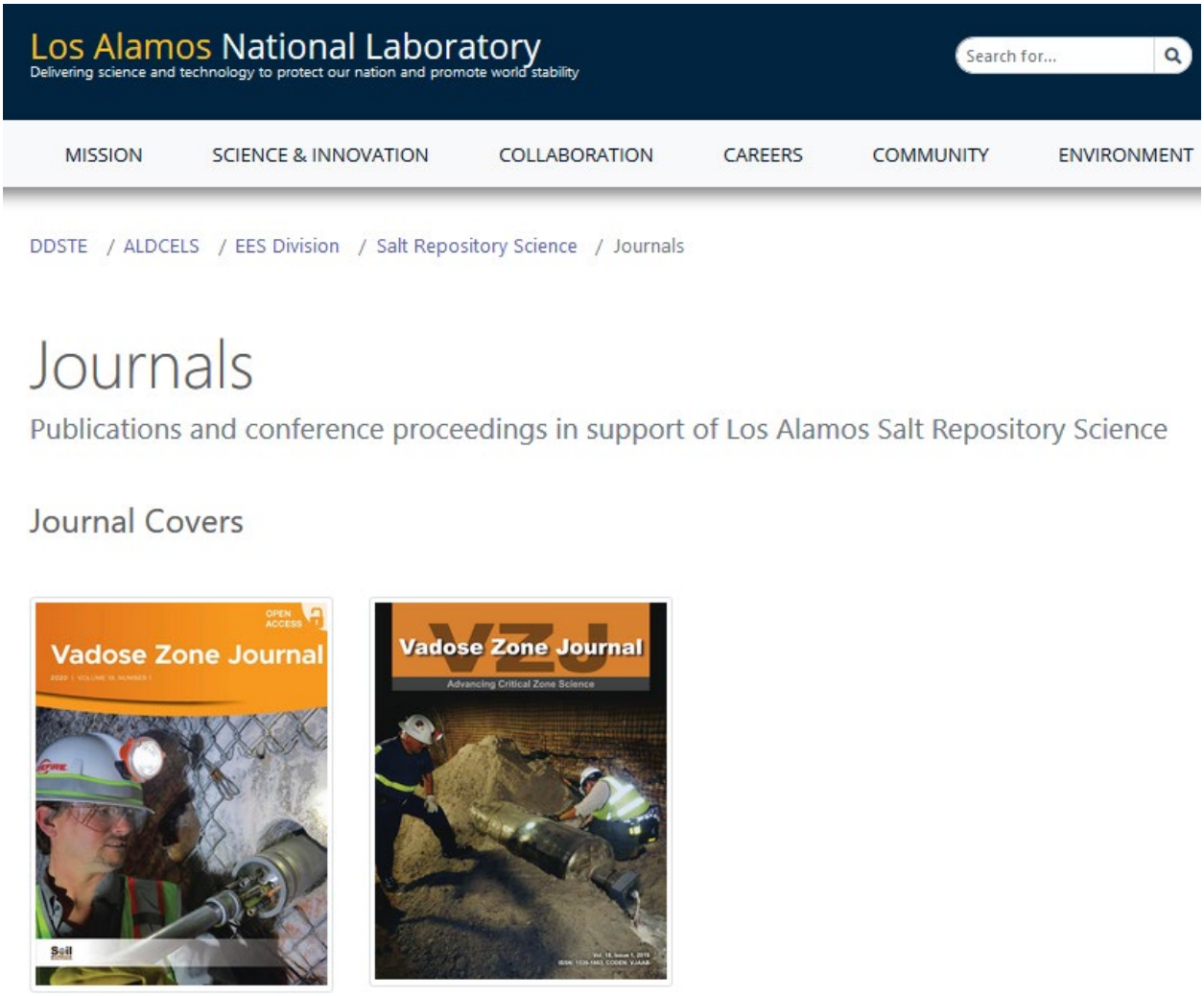

Figure 8-2. Journals webpage.

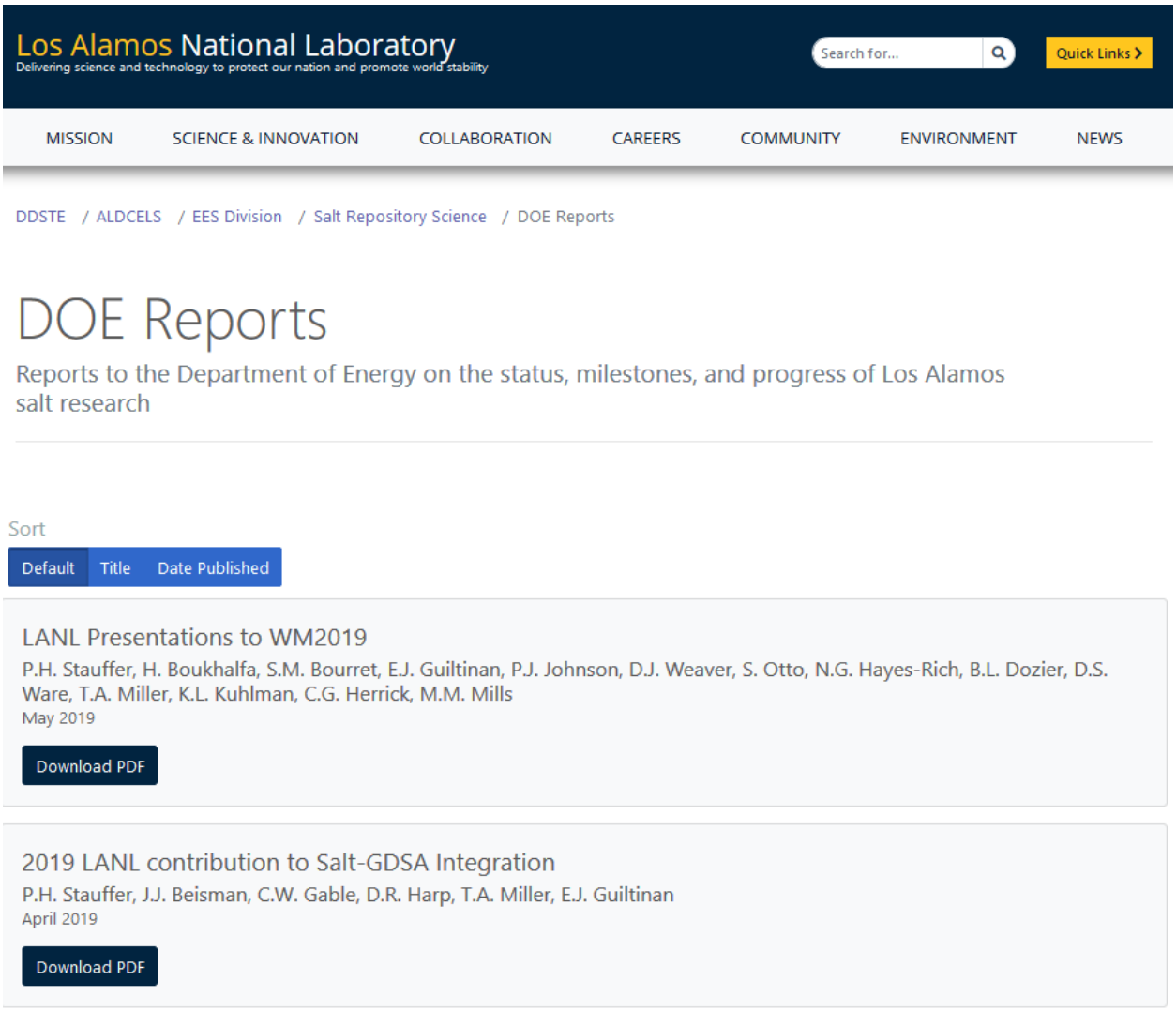

Figure 8-3. DOE Reports webpage.

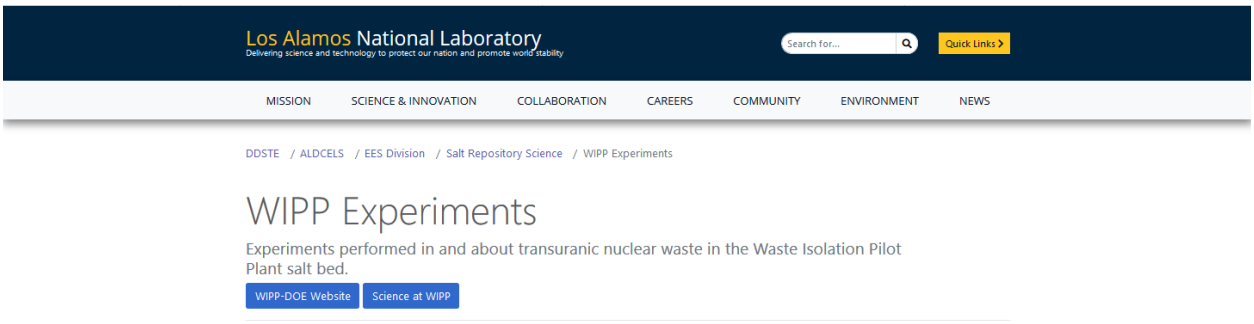

Figure 8-4. WIPP Experiments webpage.

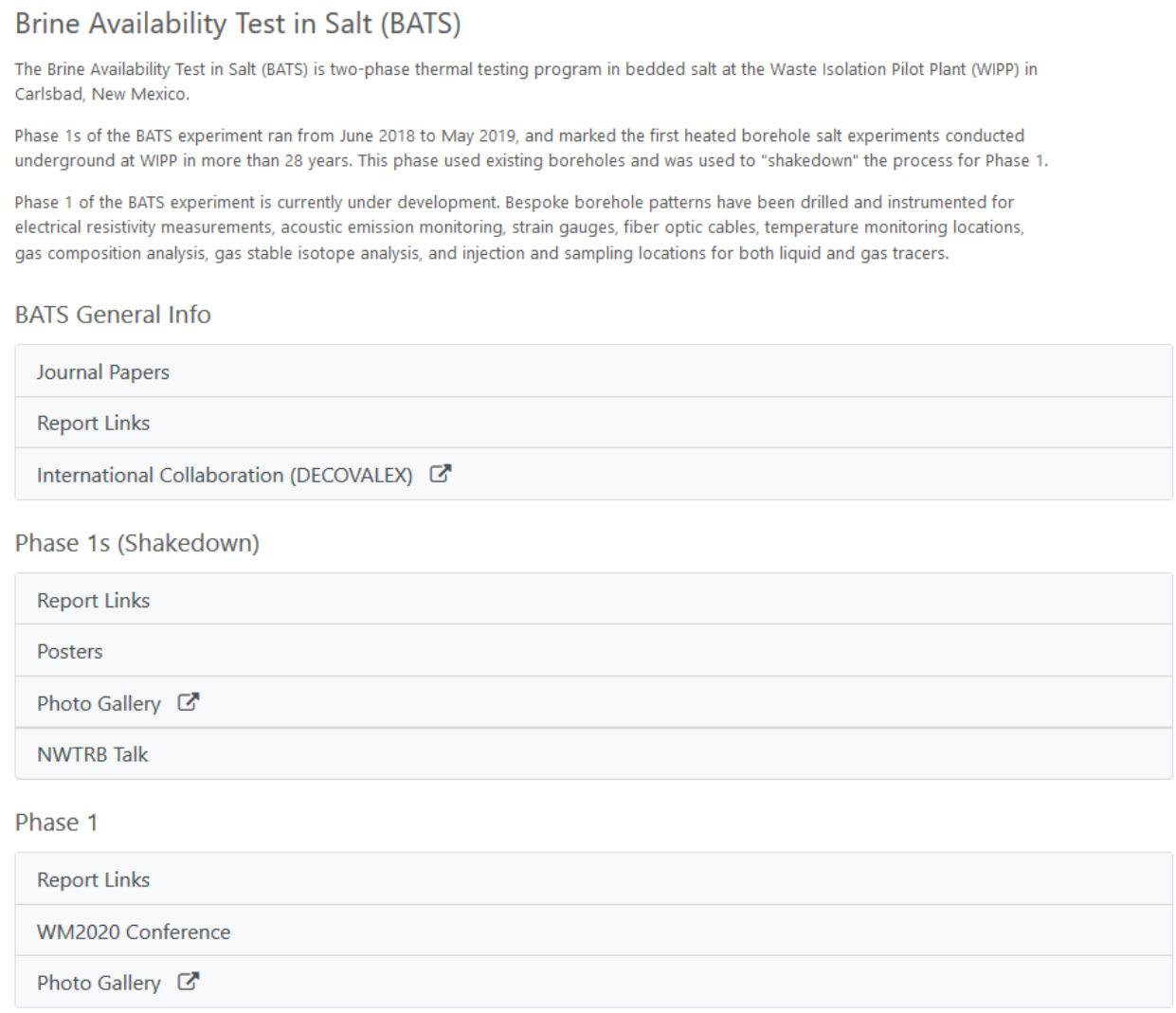

Figure 8-5. The BATS subsection of the WIPP Experiments webpage.

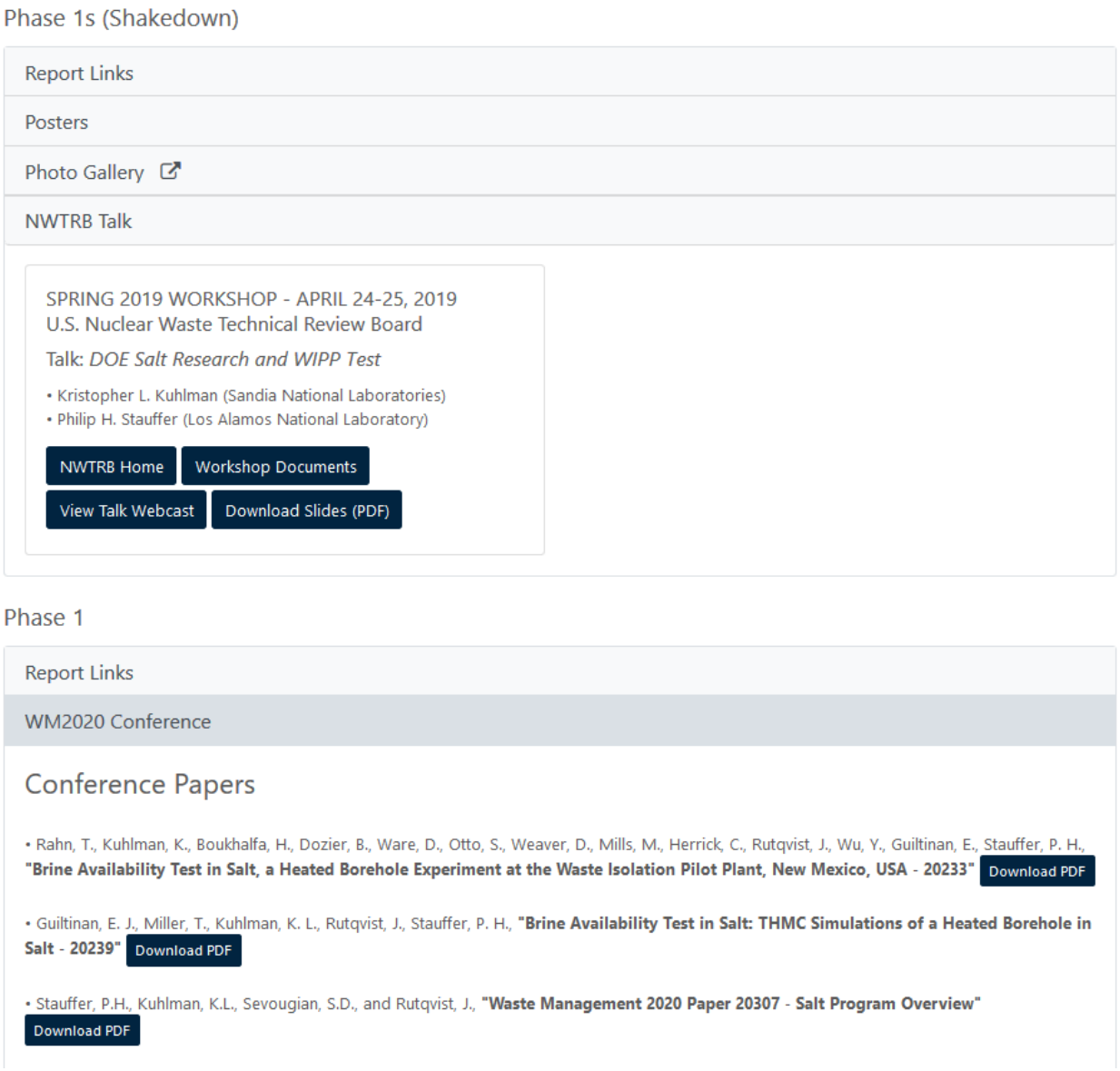

Figure 8-6. The BATS subsection of the WIPP Experiments webpage, with some content sections expanded.

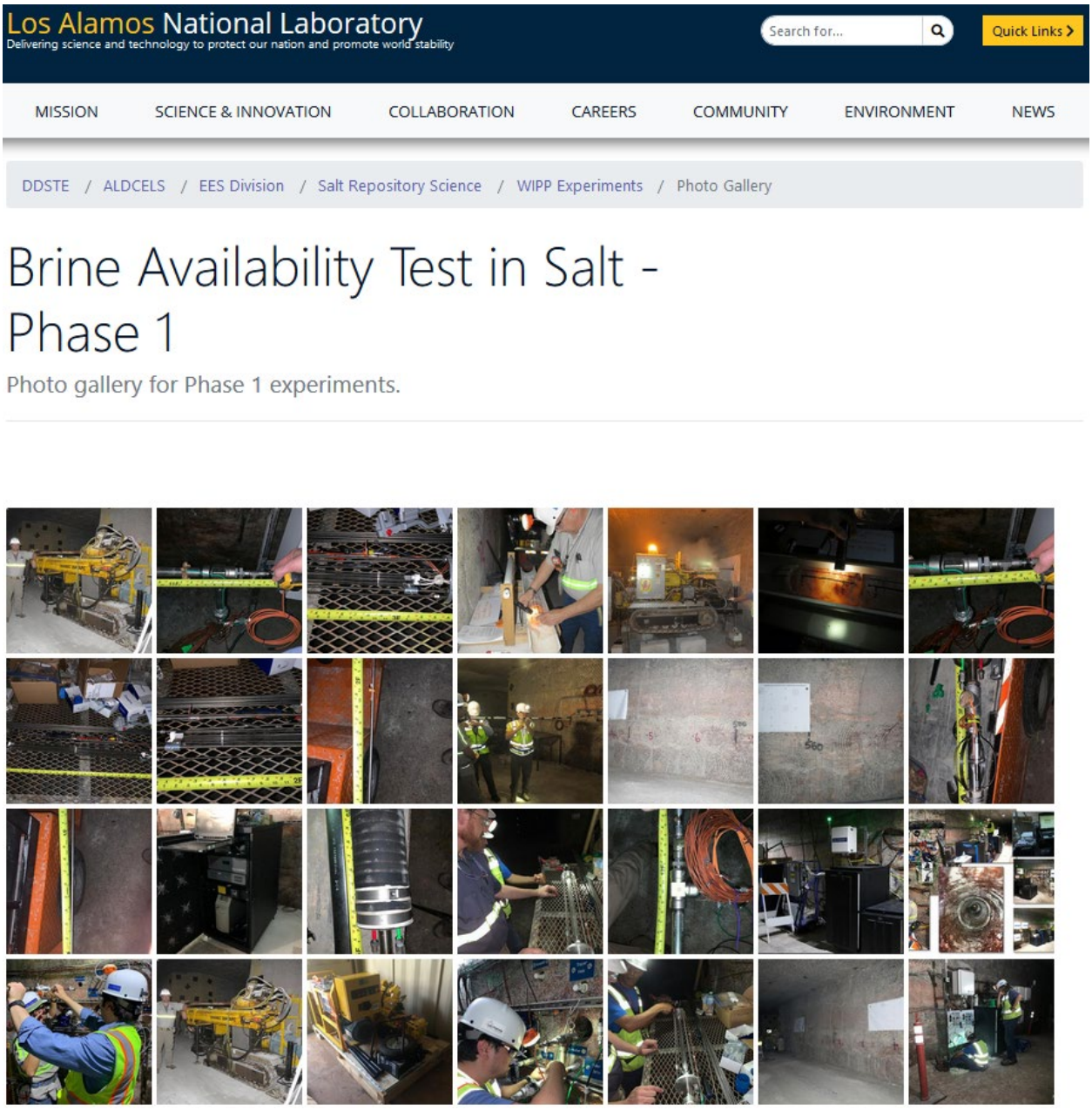

Figure 8-7. The BATS Phase 1 photo gallery within the WIPP Experiments webpage.

9. Summary

The Brine Availability Test in Salt (BATS) experiments have continued making progress towards the goal of a better understanding of brine composition, source, and abundance to heated boreholes at WIPP. The first phase of BATS was a shakedown experiment conducted on pre-existing boreholes to develop heated borehole experimental techniques and procedural methods for conducting experiments in the WIPP underground. These lessons have been put to use for

the development of the Phase 1 experiment. The BATS Phase 1 experimental borehole arrays have been completed and a Phase 1a heater experiment was conducted in early 2020. Plans to conduct Phase 1b, which includes another round of heating and the use of isotopic tracers has been delayed due uncertainty from the SARS Covid-19 pandemic. Phase 1b is now scheduled to begin later this year and will be the subject of future milestones.

LANL contributions to this work during fiscal year 2020 included extensive work by the LANL Carlsbad Field Office (CBFO) team to complete and instrument the Phase 1 boreholes as well as conduct ongoing maintenance, data acquisition, and perform permeability experiments. The large array of equipment includes many temperature sensors, electrical resistivity electrodes, piezoelectric transducers for monitoring acoustic emissions, and fiber optic distributed temperature and strain sensors. Many lessons learned during the drilling of these arrays, and installation of these sensors have been documented by the CBFO team and incorporated into Chapter 7 of this report.

Other scientific LANL contributions during fiscal year 2020 are included in the other chapters. We present chemical analysis of brine samples and comparison to historical data (Chapter 2); analysis of the isotopic signature during the Phase 1a experiment and preparations for laboratory measurements of the different brine sources collected in core samples (Chapter 3); FEHM code developments to properly handle relative humidity boundary conditions associated with the BATS simulations (Chapter 4); simulations of temperature and brine flow during the Phase 1a test with initial model development for isotopic transport simulations (Chapter 5); and an analysis of the permeability experiments (Chapter 6). In addition to this work a peer-reviewed journal publication documenting the BATS team results from Phase 1s was published (Section 5-5); and a public facing website was established to promote accessibility to LANLs contributions to the SFWD campaign (Chapter 8).

10. References

Appelo, C., 2015, Principles, caveats and improvements in databases for calculating hydrogeochemical reactions in saline waters from 0 to 200 C and 1 to 1000 atm: Applied Geochemistry, v. 55, p. 62-71.

Appelo, C., D. L. Parkhurst, and V. Post, 2014, Equations for calculating hydrogeochemical reactions of minerals and gases such as CO2 at high pressures and temperatures: Geochimica et Cosmochimica Acta, v. 125, p. 49-67.

Beauheim, R. L., 1997, INTRAVAL Phase 2 WIPP 1 test case report: Modeling of brine flow through halite at the Waste Isolation Pilot Plant site, Sandia National Laboratories, Albuquerque, NM. SAND-97-0788

Beauheim, R. L., and R. M. Roberts, 2002, Hydrology and hydraulic properties of a bedded evaporite formation: Journal of Hydrology, v. 259, p. 66-88.

Bein, A., S. Hovorka, R. Fisher, and E. Roedder, 1991, Fluid inclusions in bedded Permian halite, Palo Duro Basin, Texas; evidence for modification of seawater in evaporite brine-pools and subsequent early diagenesis: Journal of Sedimentary Research, v. 61, p. 1-14.

Boukhalfa, H., P. J. Johnson, D. Ware, D. J. Weaver, S. Otto, B. L. Dozer, P. H. Stauffer, M. M. Mills, E. N. Matteo, M. B. Nemer, C. G. Herrick, K. L. Kuhlman, Y. Wu, and J. Rutqvist,

2018, Implementation of Small Diameter Borehole Thermal Experiments at WIPP, Los Alamos, NM, Los Alamos National Laboratory.
Braitsch, O., 2012, Salt deposits their origin and composition, v. 4, Springer Science & Business Media.
Caporuscio, F. A., H. Boukhalfa, M. Cheshire, and M. Ding, 2014, Brine migration experimental studies for salt repositories, Los Alamos National Lab.(LANL), Los Alamos, NM (United States).
Colon, J. F. C., W. F. Philippe, T. Hadgu, J. E. Bean, J. M. Martinez, J. G. Arguello, C. Leigh, and F. D. Hansen, 2012, Thermomechanical-Hydrological and Chemical (TMHC) Model Development, Albuquerque, NM, Sandia National Laboratory.
Davies, P. B., 1991, Evaluation of the role of threshold pressure in controlling flow of waste-generated gas into bedded salt at the Waste Isolation Pilot Plant, Sandia National Laboratories Albuquerque, NM.
Deal, D., R. Abitz, J. Myers, J. Case, M. Martin, W. Roggenthen, and D. Belski, 1991, Brine Sampling and Evaluation Program, 1990 report, Westinghouse Electric Corp., Carlsbad, NM (United States). Waste Isolation Div.
Doherty J., 2006. Fast Lookup of CO2 Properties, LANL informal report.
Dublyansky, Y., 2012, Design of two crushing devices for release of the fluid inclusion volatiles: Open Geosciences, v. 4, p. 219-224.
Friedman, I., and J. R. O'Neil, 1977, Compilation of stable isotope fractionation factors of geochemical interest, v. 440, US Government Printing Office.
Garcia-Veigas, J., J. J. Pueyo, and C. Ayora, 1992, Fluid inclusion analysis and evaportie modeling: International symposium on water-rock interaction, p. 649-653.
Guiltinan, E., D. Espinoza, L. Cockrell, and M. Cardenas, 2018, Textural and compositional controls on mudrock breakthrough pressure and permeability: Advances in Water Resources, v. 121, p. 162-172.
Guiltinan, E. J., K. L. Kuhlman, J. Rutqvist, M. Hu, H. Boukhalfa, M. Mills, S. Otto, D. J. Weaver, B. Dozier, and P. H. Stauffer, 2020, Temperature response and brine availability to heated boreholes in bedded salt: Vadose Zone Journal, v. 19, p. e20019.
Hansen, F. D., and C. D. Leigh, 2011, Salt disposal of heat-generating nuclear waste, Sandia National Laboratories Albuquerque, NM.
Hardie, L. A., 1968, The origin of the recent non-marine evaporite deposit of Saline Valley, Inyo County, California: Geochimica et Cosmochimica Acta, v. 32, p. 1279-1301.
Hardie, L. A., 1982, Reconstruction of Brine Compositions of Ancient Evaporites from Their Mineralogy: Application to Chemistry of Ancient Seawater: AAPG Bulletin, v. 66, p. 577-577.
Horita, J., and S. Matsuo, 1986, Extraction and isotopic analysis of fluid inclusions in halites: Geochemical Journal, v. 20, p. 261-272.
Horita, J., and D. J. Wesolowski, 1994, Liquid-vapor fractionation of oxygen and hydrogen isotopes of water from the freezing to the critical temperature: Geochimica et Cosmochimica Acta, v. 58, p. 3425-3437.
Johnson, P. J., S. Otto, D. J. Weaver, B. Dozier, T. A. Miller, A. B. Jordan, N. G. Hayes-Rich, and P. H. Stauffer, 2019, Heat-generating nuclear waste in salt: Field testing and simulation: Vadose Zone Journal, v. 18, p. 1-14.
Johnson, P.J., H. Boukhalf, D.J. Weaver, S. Otto., B.L. Dozer, P.H. Stauffer, M.M. Mills, E.N. Matteo, K.L., Kuhlman, J. Rutqvist, Y. Wu. 2017, Test Plan Document for Thermal

Testing in Salt. US Dept. of Energy Used Fuel Disposition Campaign, DOE Milestone M3SF-18LA010303013
Knauth, L. P., and M. A. Beeunas, 1986, Isotope geochemistry of fluid inclusions in Permian halite with implications for the isotopic history of ocean water and the origin of saline formation waters: Geochimica et Cosmochimica Acta, v. 50, p. 419-433.
Kuhlman, K.L., M.M. Mills & E.N. Matteo, 2017. Consensus on Intermediate Scale Salt Field Test Design. SAND2017–3179R, Albuquerque, NM: Sandia National Laboratories.
Kuhlman, K., M. Mills, R. Jayne, E. Matteo, C. Herrick, M. Nemer, J. Heat, Y. Xiong, C. Choens, P. Stauffer, H. Boudkhalfa, E. Guiltinan, T. Rahn, D. Weaver, B. Dozer, S. Otto, J. Rutqvist, Y. Wu, M. Hu, S. Uhlemann, and J. Wang, 2020, FY20 Update on Brine Availability Test in Salt, Albuquerque, NM, Sandia National Laboratories.
Kwicklis, E. M., A. V. Wolfsberg, P. H. Stauffer, M. A. Walvoord, and M. J. Sully, 2006, Multiphase, multicomponent parameter estimation for liquid and vapor fluxes in deep arid systems using hydrologic data and natural environmental tracers: Vadose Zone Journal, v. 5, p. 934-950.
Lambert, S. J., 1992, Geochemistry of the waste isolation pilot plant (WIPP) site, southestern New Mexico, USA: Applied geochemistry, v. 7, p. 513-531.
Lappin, A., 1988, Summary of site-characterization studies conducted from 1983 through 1987 at the Waste Isolation Pilot Plant (WIPP) site, southeastern New Mexico, Waste management'88.
Lemmon, E., M. L. Huber, and M. McLinden, 2013, NIST standard reference database 23: reference fluid thermodynamic and transport properties-REFPROP, version 9.1, standard reference data program: National Institute of Standards and Technology: Gaithersburg, MD.
Lucchini, J., M. Borkowski, H. Khaing, M. Richmann, J. Swanson, K. Simmons, and D. Reed, 2013, WIPP Actinide-Relevant Brine Chemistry: Los Alamos National Laboratory, Los Alamos, New Mexico.
Merlivat, L., and M. Coantic, 1975, Study of mass transfer at the air-water interface by an isotopic method: Journal of Geophysical Research, v. 80, p. 3455-3464.
Mills, M. M., K. L. Kuhlman, E. N. Matteo, C. G. Herrick, M. Nemer, J. E. Heath, Y. Xiong, M. J. Paul, P. o. Stauffer, Hakim, E. Guiltinan, T. Rahn, D. o. Weaver, Brian, S. Otto, J. Rutqvist, Y. j.-F. Wu, Jonathan, and M. Ò. Hu, 2019, Salt Heater Test (FY19), Sandia National Laboratories, Albuquerque, NM SAND2019-4814R
Munson, D., R. Jones, J. Ball, R. Clancy, D. Hoag, and S. Petney, 1990, Overtest for Simulated Defense High-Level Waste (Room B): In situ data report (May 1984--February 1988): Waste Isolation Pilot Plant (WIPP) Thermal/Structural Interactions Program, Sandia National Labs., Albuquerque, NM (USA).
Rigaudier, T., V. Gardien, F. Martineau, G. Reverdy, and C. Lécuyer, 2012, Hydrogen and oxygen isotope reference materials for the analysis of water inclusions in halite: Geostandards and Geoanalytical Research, v. 36, p. 51-59.
Roedder, E., 1984, The fluids in salt: American Mineralogist, v. 69, p. 413-439.
Roedder, E., and R. Bassett, 1981, Problems in determination of the water content of rock-salt samples and its significance in nuclear-waste storage siting: Geology, v. 9, p. 525-530.
Smiles, D., W. Gardner, and R. Schulz, 1995, Diffusion of tritium in arid disposal sites: Water Resources Research, v. 31, p. 1483-1488.
Sandia National Lab (SNL), 2020, Project Plan: Salt in situ Heater Test.

Song, Y.-Q., and R. Kausik, 2019, NMR application in unconventional shale reservoirs–A new porous media research frontier: Progress in nuclear magnetic resonance spectroscopy, v. 112, p. 17-33.

Stauffer, P., A. Jordan, D. Weaver, F. Caporuscio, J. Ten Cate, H. Boukhalfa, B. Robinson, D. Sassani, K. Kuhlman, and E. Hardin, 2015, Test proposal document for phased field thermal testing in salt: FCRD Used Fuel Disposition Campaign Milestone FCRD-UFD-2015-000077.

Stein, C. L., and J. L. Krumhansl, 1986, Chemistry of brines in salt from the Waste Isolation Pilot Plant (WIPP), southeastern New Mexico: a preliminary investigation, Sandia National Labs., Albuquerque, NM (USA).

Uemura, R., M. Nakamoto, R. Asami, S. Mishima, M. Gibo, K. Masaka, C. Jin-Ping, C.-C. Wu, Y.-W. Chang, and C.-C. Shen, 2016, Precise oxygen and hydrogen isotope determination in nanoliter quantities of speleothem inclusion water by cavity ring-down spectroscopic techniques: Geochimica et Cosmochimica Acta, v. 172, p. 159-176.

11. Appendix 1

Table S.1 saturation indices calculated for synthetic brines.

ERDA

Temp	5	15	25	40	55	70	85
Polyhalite	-4.56	-4.46	-4.45	-4.57	-4.84	-5.23	-5.71
Magnesite	-0.02	0.11	0.19	0.26	0.27	0.23	0.15
Anhydrite	-0.47	-0.34	-0.22	-0.07	0.06	0.18	0.28
Goergeyite	3.25	2.51	1.88	1.12	0.56	0.14	-0.14
Gypsum	-0.06	-0.07	-0.08	-0.1	-0.13	-0.16	-0.2
Halite	-0.23	-0.22	-0.23	-0.24	-0.26	-0.29	-0.31
Brucite	-7.05	-6.43	-5.88	-5.17	-4.57	-4.08	-3.67
Huntite	-1.92	-0.84	0.1	1.31	2.35	3.26	4.08
Dolomite	0.55	1	1.35	1.74	1.98	2.11	2.14

Brine A

Temp	5	15	25	40	55	70	85
Polyhalite	-2.28	-2.37	-2.55	-2.97	-3.54	-4.22	-5.02
Magnesite	2.2	2.25	2.27	2.27	2.23	2.15	2.04
Anhydrite	-0.68	-0.6	-0.53	-0.45	-0.4	-0.36	-0.35
Goergeyite	3.4	2.38	1.46	0.27	-0.75	-1.63	-2.39
Gypsum	-0.32	-0.37	-0.43	-0.52	-0.62	-0.74	-0.86
Halite	-0.31	-0.33	-0.34	-0.37	-0.41	-0.44	-0.48
Brucite	-4.21	-3.67	-3.2	-2.6	-2.09	-1.68	-1.35
Huntite	5.19	5.99	6.69	7.64	8.48	9.24	9.95

Dolomite	3.23	3.55	3.79	4.04	4.19	4.25	4.22

G-Seep

Temp	5	15	25	40	55	70	85
Polyhalite	-0.81	-0.85	-0.97	-1.3	-1.77	-2.36	-3.05
Magnesite	1.49	1.56	1.6	1.61	1.56	1.47	1.35
Anhydrite	-0.28	-0.19	-0.11	-0.02	0.06	0.11	0.15
Goergeyite	5.56	4.6	3.75	2.67	1.77	1.02	0.4
Gypsum	0.07	0.03	-0.02	-0.1	-0.18	-0.28	-0.37
Halite	-0.05	-0.06	-0.07	-0.1	-0.13	-0.16	-0.19
Brucite	-5.45	-4.9	-4.41	-3.79	-3.27	-2.84	-2.49
Huntite	2.27	3.13	3.88	4.84	5.66	6.37	6.99
Dolomite	1.72	2.06	2.31	2.57	2.7	2.73	2.65

Inclusions

Temp	5	15	25	40	55	70	85
Polyhalite	-1.99	-2.04	-2.17	-2.51	-2.99	-3.59	-4.3
Magnesite	1.97	2.04	2.08	2.09	2.06	1.98	1.88
Anhydrite	-0.61	-0.52	-0.45	-0.35	-0.28	-0.22	-0.19
Goergeyite	3.43	2.46	1.61	0.52	-0.39	-1.14	-1.78
Gypsum	-0.21	-0.26	-0.3	-0.38	-0.47	-0.56	-0.66
Halite	-0.36	-0.37	-0.38	-0.41	-0.44	-0.47	-0.5
Brucite	-4.51	-3.95	-3.47	-2.84	-2.32	-1.89	-1.54
Huntite	3.94	4.79	5.54	6.52	7.39	8.17	8.87
Dolomite	2.43	2.76	3.02	3.29	3.45	3.51	3.47

Brine Weeps

Temp	5	15	25	40	55	70	85
Polyhalite	-1.97	-1.99	-2.11	-2.42	-2.88	-3.46	-4.15
Magnesite	2.02	2.09	2.12	2.13	2.1	2.03	1.92
Anhydrite	-0.63	-0.53	-0.45	-0.35	-0.27	-0.21	-0.16
Goergeyite	3.63	2.71	1.89	0.85	-0.02	-0.73	-1.33
Gypsum	-0.26	-0.3	-0.34	-0.41	-0.48	-0.57	-0.66
Halite	-0.19	-0.19	-0.21	-0.23	-0.26	-0.29	-0.32
Brucite	-4.5	-3.95	-3.46	-2.83	-2.31	-1.88	-1.54
Huntite	4.33	5.18	5.92	6.91	7.78	8.57	9.27
Dolomite	2.72	3.06	3.32	3.59	3.75	3.82	3.79

Table S2. Summary of the saturation index data used in the plots presented in Figure 7.

HPShakedown

Temp	5	15	25	40	55	70	85
Polyhalite	1.52	1.28	0.96	0.34	-0.42	-1.3	-2.27
Magnesite	2.5	2.5	2.49	2.43	2.34	2.2	1.99
Anhydrite	0.1	0.13	0.14	0.15	0.14	0.11	0.06
Goergeyite	8.05	6.76	5.59	4.03	2.66	1.45	0.36
Gypsum	0.35	0.25	0.14	-0.01	-0.18	-0.35	-0.53
Halite	0.18	0.16	0.13	0.08	0.04	-0.01	-0.06
Brucite	-3.68	-3.17	-2.73	-2.16	-1.71	-1.35	-1.08
Huntite	5.65	6.24	6.77	7.5	8.13	8.63	8.9
Dolomite	3.09	3.29	3.44	3.57	3.61	3.52	3.27

UD 7-9

Temp	5	15	25	40	55	70	85
Polyhalite	-2.08	-2.16	-2.29	-2.59	-3	-3.5	-4.09
Magnesite	1.25	1.37	1.45	1.52	1.54	1.52	1.47
Anhydrite	-0.83	-0.74	-0.66	-0.55	-0.45	-0.37	-0.29
Goergeyite	3.2	2.18	1.32	0.28	-0.52	-1.12	-1.58
Gypsum	-0.28	-0.33	-0.38	-0.44	-0.5	-0.56	-0.63
Halite	-2.7	-2.73	-2.75	-2.78	-2.81	-2.83	-2.84
Brucite	-5.36	-4.76	-4.23	-3.54	-2.96	-2.47	-2.06
Huntite	1.42	2.43	3.35	4.56	5.64	6.61	7.51
Dolomite	1.35	1.75	2.09	2.46	2.72	2.87	2.93

UF2 7-9

Temp	5	15	25	40	55	70	85
Polyhalite	-1000	-1000	-1000	-1000	-1000	-1000	-1000
Magnesite	-1000	-1000	-1000	-1000	-1000	-1000	-1000
Anhydrite	-1.42	-1.35	-1.28	-1.2	-1.14	-1.1	-1.07
Goergeyite	0.81	-0.21	-1.11	-2.26	-3.21	-3.99	-4.64
Gypsum	-1.08	-1.14	-1.2	-1.3	-1.4	-1.5	-1.6
Halite	0.02	0.01	0	-0.03	-0.06	-0.1	-0.13
Brucite	-1000	-1000	-1000	-1000	-1000	-1000	-1000
Huntite	-1000	-1000	-1000	-1000	-1000	-1000	-1000
Dolomite	-1000	-1000	-1000	-1000	-1000	-1000	-1000

Sample: UEI

Temp	5	15	25	40	55	70	85
Polyhalite	-2.46	-2.49	-2.6	-2.91	-3.37	-3.94	-4.63

Magnesite	1.98	2.03	2.06	2.06	2.02	1.94	1.83
Anhydrite	-0.77	-0.67	-0.59	-0.48	-0.4	-0.34	-0.3
Goergeyite	2.76	1.84	1.03	-0.01	-0.87	-1.58	-2.17
Gypsum	-0.39	-0.42	-0.46	-0.53	-0.61	-0.69	-0.78
Halite	-0.26	-0.27	-0.28	-0.3	-0.33	-0.36	-0.39
Brucite	-4.52	-3.96	-3.47	-2.84	-2.32	-1.89	-1.55
Huntite	4.09	4.88	5.59	6.54	7.39	8.15	8.81
Dolomite	2.56	2.87	3.1	3.36	3.51	3.57	3.52

Sample:
UD

Temp	5	15	25	40	55	70	85
Polyhalite	-3.43	-3.41	-3.48	-3.71	-4.08	-4.56	-5.15
Magnesite	1.56	1.65	1.71	1.75	1.74	1.7	1.62
Anhydrite	-1.05	-0.94	-0.84	-0.71	-0.6	-0.51	-0.43
Goergeyite	1.33	0.47	-0.27	-1.19	-1.91	-2.47	-2.92
Gypsum	-0.59	-0.61	-0.64	-0.68	-0.73	-0.79	-0.86
Halite	-0.69	-0.69	-0.7	-0.72	-0.75	-0.77	-0.79
Brucite	-5.01	-4.42	-3.9	-3.23	-2.67	-2.2	-1.82
Huntite	2.52	3.46	4.29	5.39	6.38	7.26	8.07
Dolomite	1.84	2.21	2.51	2.84	3.06	3.17	3.19

Sample:
USL

Temp	5	15	25	40	55	70	85
Polyhalite	-2.12	-2.14	-2.24	-2.53	-2.97	-3.53	-4.19
Magnesite	1.88	1.94	1.97	1.99	1.96	1.89	1.79
Anhydrite	-0.71	-0.61	-0.53	-0.42	-0.33	-0.26	-0.21
Goergeyite	3.22	2.3	1.5	0.48	-0.35	-1.03	-1.59
Gypsum	-0.3	-0.34	-0.38	-0.44	-0.51	-0.59	-0.68
Halite	-0.4	-0.41	-0.42	-0.44	-0.47	-0.5	-0.52
Brucite	-4.67	-4.1	-3.61	-2.96	-2.43	-1.99	-1.64
Huntite	3.68	4.51	5.25	6.24	7.13	7.93	8.63
Dolomite	2.36	2.68	2.94	3.21	3.38	3.45	3.42

Sample:
HE2

Temp	5	15	25	40	55	70	85
Polyhalite	-3.31	-3.29	-3.36	-3.6	-3.97	-4.46	-5.05

Magnesite	1.57	1.66	1.71	1.76	1.75	1.71	1.62
Anhydrite	-1.04	-0.93	-0.83	-0.7	-0.59	-0.5	-0.43
Goergeyite	1.43	0.57	-0.18	-1.11	-1.84	-2.41	-2.86
Gypsum	-0.57	-0.6	-0.63	-0.67	-0.73	-0.79	-0.85
Halite	-0.71	-0.71	-0.72	-0.75	-0.77	-0.79	-0.81
Brucite	-5	-4.41	-3.9	-3.22	-2.66	-2.2	-1.81
Huntite	2.51	3.44	4.28	5.38	6.36	7.25	8.05
Dolomite	1.81	2.18	2.48	2.81	3.02	3.14	3.16

Sample:
UHP

Temp	5	15	25	40	55	70	85
Polyhalite	-1.4	-1.44	-1.57	-1.91	-2.39	-2.99	-3.7
Magnesite	2.03	2.08	2.1	2.1	2.06	1.98	1.86
Anhydrite	-0.44	-0.35	-0.27	-0.18	-0.1	-0.05	-0.01
Goergeyite	4.61	3.65	2.81	1.73	0.82	0.07	-0.57
Gypsum	-0.06	-0.1	-0.15	-0.23	-0.31	-0.4	-0.5
Halite	-0.26	-0.27	-0.29	-0.31	-0.34	-0.37	-0.4
Brucite	-4.46	-3.91	-3.43	-2.8	-2.28	-1.86	-1.52
Huntite	4.41	5.19	5.89	6.82	7.65	8.4	9.05
Dolomite	2.79	3.08	3.31	3.56	3.7	3.75	3.69

Sample:
HHP

Temp	5	15	25	40	55	70	85
Polyhalite	-2.01	-2.04	-2.15	-2.46	-2.91	-3.48	-4.16
Magnesite	1.93	1.99	2.02	2.03	2	1.92	1.81
Anhydrite	-0.69	-0.6	-0.51	-0.41	-0.32	-0.26	-0.22
Goergeyite	3.34	2.41	1.6	0.56	-0.3	-1.01	-1.59
Gypsum	-0.29	-0.33	-0.37	-0.44	-0.51	-0.6	-0.69
Halite	-0.35	-0.36	-0.37	-0.4	-0.42	-0.45	-0.48
Brucite	-4.59	-4.03	-3.54	-2.91	-2.38	-1.94	-1.59
Huntite	3.88	4.69	5.41	6.38	7.25	8.03	8.72
Dolomite	2.44	2.76	3	3.27	3.43	3.49	3.45

Sample : HAE2

Temp	5	15	25	40	55	70	85
Polyhalite	-6.61	-6.59	-6.63	-6.78	-7.02	-7.35	-7.75
Magnesite	0.51	0.66	0.77	0.9	0.96	0.99	0.97
Anhydrite	-1.81	-1.7	-1.58	-1.42	-1.28	-1.14	-1.02

Goergeyite	-3.21	-4.07	-4.77	-5.55	-6.08	-6.4	-6.56
Gypsum	-1.25	-1.27	-1.28	-1.3	-1.31	-1.32	-1.34
Halite	-1.73	-1.75	-1.77	-1.79	-1.81	-1.82	-1.83
Brucite	-6.15	-5.5	-4.92	-4.16	-3.52	-2.97	-2.52
Huntite	-1.44	-0.29	0.76	2.18	3.44	4.59	5.65
Dolomite	-0.03	0.45	0.85	1.33	1.68	1.92	2.06

Sample: H-T2

Temperature	**5**	**15**	**25**	**40**	**55**	**70**	**85**
Polyhalite	-2.9	-2.89	-2.96	-3.21	-3.6	-4.11	-4.72
Magnesite	1.68	1.76	1.81	1.84	1.83	1.77	1.68
Anhydrite	-0.92	-0.81	-0.72	-0.59	-0.49	-0.41	-0.35
Goergeyite	2.06	1.19	0.43	-0.52	-1.27	-1.88	-2.36
Gypsum	-0.48	-0.51	-0.54	-0.59	-0.65	-0.71	-0.79
Halite	-0.56	-0.56	-0.57	-0.59	-0.62	-0.64	-0.66
Brucite	-4.88	-4.3	-3.79	-3.13	-2.58	-2.12	-1.75
Huntite	2.95	3.85	4.65	5.71	6.65	7.51	8.27
Dolomite	2.02	2.38	2.66	2.97	3.16	3.26	3.26

U-ES

Temperature	5	15	25	40	55	70	85
Polyhalite	-2.86	-2.85	-2.92	-3.17	-3.57	-4.08	-4.69
Magnesite	1.68	1.76	1.81	1.84	1.83	1.77	1.68
Anhydrite	-0.92	-0.81	-0.71	-0.59	-0.49	-0.41	-0.35
Goergeyite	2.1	1.22	0.46	-0.49	-1.25	-1.86	-2.35
Gypsum	-0.47	-0.5	-0.53	-0.58	-0.64	-0.71	-0.78
Halite	-0.57	-0.58	-0.59	-0.61	-0.64	-0.66	-0.68
Brucite	-4.89	-4.31	-3.79	-3.13	-2.58	-2.12	-1.75
Huntite	2.93	3.82	4.62	5.69	6.63	7.48	8.25
Dolomite	2	2.36	2.64	2.95	3.14	3.24	3.24

H-T1

Temperature	**5**	**15**	**25**	**40**	**55**	**70**	**85**
Polyhalite	-2.63	-2.63	-2.71	-2.97	-3.37	-3.9	-4.52
Magnesite	1.74	1.81	1.86	1.88	1.86	1.81	1.71
Anhydrite	-0.84	-0.74	-0.64	-0.52	-0.43	-0.35	-0.29
Goergeyite	2.49	1.61	0.84	-0.12	-0.9	-1.53	-2.03
Gypsum	-0.41	-0.44	-0.47	-0.52	-0.59	-0.66	-0.73
Halite	-0.51	-0.52	-0.53	-0.55	-0.58	-0.6	-0.62
Brucite	-4.82	-4.25	-3.74	-3.09	-2.54	-2.09	-1.72

Huntite	3.18	4.05	4.84	5.88	6.81	7.64	8.39
Dolomite	2.14	2.48	2.76	3.06	3.24	3.33	3.33

Table S3. Complete analytical data of the BATS samples. All concentrations are in mg/L.

	Samples						
Species	H-SL-12-19	U-SL-12-19	H-D-4-23-20	H-F2-FO wires-2-24-20	H-F2-FO wires-2-6-20	U-D-7-9-20	U-F2-7-9-20
Br	1174	1139	1073	814	288	1631	863
Cl	183840	178823	186889	202691	48236	232063	215356
F	<100	<100	<100	<100	<100	<100	<100
NO3	<100	106.6	<100	<100	<100	<100	<100
PO4	<100	<100	<100	<100	<100	<100	<100
SO42-	10090	10133	11391	1210	1740	22636	59052
Al	<1.6	<1.6	39.8	<1.6	<1.6	<1.6	<1.6
B	1071	1043	1022	49.1	21.0	1230	28
Ba	2.0	1.8	<1.1	3.1	1.1	<1.1	3
Ca	291	240	349	6426	4840	339	16
Cr	<0.3	<0.3	0.4	1.6	1.5	<0.3	14
Fe	<1.8	<1.8	89.7	<1.8	<1.8	<1.8	<1.8
K	12651	12100	11878	13594	5713	15416	26703
Li	15.9	15.4	14.7	10.4	4.8	19	21
Mg	20902	20936	20171	1058	<1	23657	<1
MN	2.7	2.7	4.5	<0.3	<0.3	3	<0.3
Na	68592	64138	68993	96502	23824	84030	118860
Si	<27.8	<27.8	102.3	<27.8	<27.8	<59.492	177
Sr	1.7	1.2	4.8	62.6	29.0	3	3
Ti	<0.2	<0.2	0.9	<0.2	<0.2	<0.2	<0.2
Zn	680	77.1	41.7	<5.2	<5.2	<5.2	<5.2

Table S4. Complete analytical data of the BATS samples. All concentrations are in mg/L.

	Samples					
Species	H-AE3-9-19	H-AE1-9-19	U-E3-9-19	H-Seal test brines	H-AE2-9-19c	U-Seal test hole
Br	1465	1941	1016	1529	1235	2039
Cl	316159	297309	190756	206863	203230	270773
F	<100	<100	<100	<100	<100	<100
NO3	<100	<100	<100	<100	<100	<100
PO4	<100	<100	<100	<100	<100	<100

SO42-	27989	27066	17633	18626	18471	25184
Al	7.8	24.6	9.1	14.0	11.6	<1.6
B	1243	1238	925	1048	935	1193
Ba	<1.1	<1.1	<1.1	<1.1	<1.1	<1.1
Ca	287	280	414	241	335	262
Cr	0.4	0.3	<0.3	0.4	0.3	<0.3
Fe	6.5	11.4	11.2	8.9	12.1	2.6
K	15085	14699	12776	12597	12116	14671
Li	19.9	19.7	14.9	17.5	15.7	20.1
Mg	23794	23155	17705	20395	17732	24023
MN	7.6	8.1	4.1	5.3	4.8	4.2
Na	70264	71361	79215	61799	70609	69388
Si	<27.8	39.7	<27.8	<27.8	<27.8	<27.8
Sr	1.3	1.4	30.8	1.2	18.8	1.0
Ti	<0.2	0.7	0.2	0.3	0.3	<0.2
Zn	55.3	26.1	48.7	15.7	18.8	7.4

Table S5. Complete analytical data of the Shakedown sample. All concentrations are in mg/L.

Species	HP Shakedown 7-9-20
Br	2566
Cl	245101
F	<100
NO3	<100
PO4	<100
SO42-	38433
Al	<1.6
B	1090
Ba	<1.1
Ca	258
Cr	<0.3
Fe	<1.8
K	22392
Li	25
Mg	37337
Mn	7
Na	61202
Si	<59.492
Sr	2
Ti	<0.2
Zn	774